UNLV Theses, Dissertations, Professional Papers, and Capstones

12-2010

Chemical and Electronic Structure of Surfaces and Interfaces in Compound Semiconductors

Sujitra Pookpanratana
University of Nevada, Las Vegas

CHEMICAL AND ELECTRONIC STRUCTURE OF SURFACES

AND INTERFACES IN COMPOUND

SEMICONDUCTORS

by

Sujitra Pookpanratana

Bachelor of Science
University of California, San Diego
2006

A dissertation submitted in partial fulfillment
of the requirements for the

Doctor of Philosophy Degree in Chemistry
Department of Chemistry
College of Sciences

Graduate College
University of Nevada, Las Vegas
December 2010

THE GRADUATE COLLEGE

We recommend the dissertation prepared under our supervision by

Sujitra Pookpanratana

entitled

Chemical and Electronic Structure of Surfaces and Interfaces in Compound Semiconductors

be accepted in partial fulfillment of the requirements for the degree of

Doctor of Philosophy in Chemistry

Clemens Heske, Committee Chair

Paul Forster, Committee Member

Dennis Lindle, Committee Member

Rama Venkat, Graduate Faculty Representative

Ronald Smith, Ph. D., Vice President for Research and Graduate Studies
and Dean of the Graduate College

December 2010

ABSTRACT

**Chemical and Electronic Structure of Surfaces and Interfaces in
Compound Semiconductors**

by

Sujitra Pookpanratana

Dr. Clemens Heske, Examination Committee Chair
Professor of Chemistry
University of Nevada, Las Vegas

The interface formation between two different materials is important in applications for optoelectronic devices. Often, the success or performance of these devices is dependent on the formation of these heterojunctions. In this work, the surface and interfaces in such materials for optoelectronic devices are investigated by a suite of X-ray analytical techniques including X-ray photoelectron (XPS), X-ray excited Auger electron (XAES), and X-ray emission (XES) spectroscopies to provide novel insight.

For the group III-nitrides (*e.g.*, $Al_xGa_{1-x}N$) used in many light emitting devices, a significant challenge exists to form an Ohmic contact. The electron affinities and band gaps of GaN and AlN are different, and thus it is difficult to find *one* contact scheme compatible for the entire $Al_xGa_{1-x}N$ system. Contact schemes are empirically derived such that they result in optimal electrical properties, and thus this work focuses on providing a deeper understanding of the empirically derived contact-schemes. For the n-doped alloys, the presence of VN was identified at the $V-Al_xGa_{1-x}N$ interface after contact formation. The amount of VN present varied for n-GaN and n-AlN, and was indicative of the VN dependency of the $n-Al_xGa_{1-x}N$ composition. These findings provide detailed insight into the contact formation of (Al,Ga)N-based devices and the performance of V-based contacts.

Next generation thin film solar cells based on CdS/Cu(In,Ga)Se$_2$ and CdTe/CdS heterojunctions, which are expected to replace the current Si-based technologies within a decade, are constantly driven to improve their device efficiencies. However, to optimize the entire device, the interfaces and layers within such a device must be understood. The interface formation between high-efficiency Cu(In,Ga)Se$_2$ absorbers and CdS buffer layer was followed, and the findings suggest the presence of a S-containing interlayer between Cu(In,Ga)Se$_2$ and CdS. For CdTe/CdS solar cells, post-absorber deposition processing (CdCl$_2$ activation and back contact treatment) is necessary. The findings demonstrate that the CdCl$_2$ activation drives the sulfur atoms from the CdS layer towards the back contact. While both of the processing steps influence the morphology of the back contact, the spectroscopic results suggest that the CdCl$_2$ activation has a larger impact on the surface and interface composition involved in CdTe solar cells.

The surface and interface structure are complex in these optoelectronic devices, and they are expected to influence the electrical properties (and thus performance) of the final device. The goal of this dissertation is to provide new insight and physical explanations which could aid in future optimization and designs of heterojunctions.

ACKNOWLEDGEMENTS

I am thankful for mentors Dr. Jamie Matthews and Prof. Pao C. Chau – they have always provided me with sincere and honest advice. Of course, I am thankful for my family's support, especially my mother's. Max and Olaf patiently waited at home every evening – they were an inspiration to get through each day. I would not have completed this journey without the patience and constant encouragement from my best friend Jason. I am grateful to have Jason by my side for both the enjoyable and challenging times.

"Chance favors the prepared mind."

> – Louis Pasteur

"Mediocrity knows nothing higher than itself, but talent instantly recognizes genius."

> – Arthur Conan Doyle

TABLE OF CONTENTS

LIST OF FIGURES

CHAPTER 1

INTRODUCTION

1.1 Motivation

With the invention of the transistor originally by Julius E. Lilienfeld in 1926 [1], inorganic semiconductors have become an essential component in electronic devices. They are the focus for the development of modern technology as they are in devices such as computers, light emitting diodes (LED), and solar cells. Inorganic semiconductors attract interest due to their electronic properties and functionalities which can be implemented in specific devices. In particular, compound semiconductors are gaining interest due to the potential to tailor their composition to optimize their electrical and electronic properties for a particular device. Of these materials, group III nitrides and chalcogens are widely studied due to their applications in optoelectronic devices such as LEDs and solar cells, respectively. LEDs are considered to be the replacement for incandescent light bulbs due to their superior efficiency of output light per input power. With the rising demand of fossil fuels in the world, there is certainly interest in harnessing alternative energies and implementing more efficient technologies for conservation efforts.

(Al, Ga, In)-nitride alloys are important due to their applications in optoelectronic devices (*e.g.*, Ref. [2] and [3]). Currently, GaN is a central component of the blue laser that is used to read Blu-Ray Disc™ technology. The band gap (E_g) of a (Al, Ga, In)-nitride material could be tuned between 0.9 eV and 6.2 eV, if the composition (*i.e.*, stoichiometry) is changed. The application possibilities for this tunable alloy include a tandem solar cell device, and an LED providing white light. White LEDs, created by combining primary color LEDs, is a technology sought to replace incandescent light

sources due to their much higher efficiencies. Bright green LEDs, when compare to their blue and red counterparts, are challenging to produce. The green LED appears to be bright to the human eye since we are most sensitive to that wavelength [4]. Tandem solar cells are able to achieve higher efficiencies than those of a single junction cell since they consist of individual cells. Each cell (or layer) utilizes an absorber of different band gaps (E_g) where the top cell has the largest E_g to capture short wavelength light (*e.g.*, ultraviolet), while the bottom cell captures long wavelength light (*e.g.*, infrared). Thus, a tandem cell consisting of InN, GaN, and AlN appears ideal. One of the challenges in implementing nitride-based materials is providing suitable Ohmic contacts onto negatively doped $Al_xGa_{1-x}N$ alloys. A significant fundamental challenge for these materials is due to their very different electronic properties (*e.g.*, E_g and electron affinity). Thus, it is difficult to find *one* contact scheme compatible for the entire $Al_xGa_{1-x}N$ alloy system. Often times, contact schemes are complex and empirically derived, and thus a deeper understanding of the underlying interface formation processes and insights into the character of interface species. This understanding is needed to further optimize the interfaces and thus performances of associated devices. In collaboration with the group of Prof. Moustakas at Boston University, the chemical and physical structures of V-based contacts onto n-type GaN and n-AlN was investigated.

Chalcogen-based thin film solar cells are promising as the next generation of commercial photovoltaic technology. They are significantly lower in manufacturing costs compared to conventional silicon wafer-based technologies due to lower material consumption and lower semiconductor quality requirements. $Cu(In,Ga)Se_2$ (or CIGSe) and CdTe laboratory solar cells have already reached efficiencies of 20% [5] and 16.5%

[6], respectively, and have a maximum theoretical efficiency of nearly 30% for a single p-n junction solar cell [7]. With the constant push to increase the cell efficiency, it has also driven the interest of studying their chemical and electronic structure and its correlation to electrical properties of the final device. For Cu-containing chalcogens, the common p-n junction is formed between the p-type Cu-chalcopyrite absorber and a double ZnO window layer (intrinsic and n-doped). However, high efficiency devices require an intermediate CdS buffer layer. The electrical properties of the solar cell device, and the connection to it and its chemical and electronic structure of the CIGSe and CdS layers are necessary to understand to further optimize this system. In collaboration with Ingrid Repins of the National Renewal Energy Laboratory (NREL), the chemical and electronic properties of CdS/CIGSe solar cells as a function of CdS thickness was studied.

With CdTe-based solar cells, the current record efficiency was obtained nearly 10 years ago [6] and it is nearly half of the theoretically predicted value [7]. The CdTe solar cell requires additional post-absorber deposition processing which adds complexity to studying the impact of each interface in a CdTe solar cell. This in turn limits the understanding that is needed to further optimize the device. Together with the group of Prof. Compaan of the University of Toledo, the influence and impact of each post-deposition treatment on the surfaces and buried interfaces in CdTe cells were investigated.

1.2 Dissertation Organization

Here, Chapter 1 introduces the material systems which were investigated and motivations behind studying their chemical and electronic structures in light of the device applications. In Chapter 2, a brief literature review is presented to provide the context and motivation of this dissertation work. The physical principles and brief descriptions of the spectroscopic and microscopic techniques that were used for this dissertation are discussed in Chapter 3.

Chapters 4 and 5 present the results from investigating the contact formation of V onto n-type GaN and AlN by using a suite of spectroscopic and microscopic characterization techniques including X-ray photoelectron spectroscopy (XPS), X-ray emission spectroscopy (XES), photoemission electron emission microscopy (PEEM), and atomic force microscopy (AFM). Here, the chemical structure before and after contact formation was investigated to provide the chemical phases which are formed that may contribute to the Ohmic properties. The results provide a mechanism for the contact formation to the entire $Al_xGa_{1-x}N$ alloy.

In Chapter 6, the chemical structure of the interface formation between CdS and CIGSe absorbers is presented using XPS and XES. Also, the electronic structure, investigated by ultraviolet photoelectron spectroscopy (UPS) and inverse photoemission spectroscopy (IPES), provides insight into the electronic energy alignment between CdS and high-efficiency CIGSe absorbers. In chapter 7, the effects of each post-deposition treatment on the surfaces and interfaces of CdTe/CdS solar cells are presented.

Chapter 8 provides a summary of the results shown in the previous chapters, and an outlook on the future direction towards this research work.

CHAPTER 2

LITERATURE REVIEW

2.1 Contact Formation on Semiconductors

The interface formation between a metal and semiconductor are necessary in all devices since they enable the current flow into and out of the semiconductor material. Before going into more detail, the basic physical characteristics of a metal and a semiconductor must be first be introduced. The energy band diagram of an isolated metal and semiconductor are shown below in Fig. 2.1. The work function (Φ) of a semiconductor material (Φ_{sc}) is usually different from a metal's (Φ_m). The work function is defined as the energy difference between the Fermi energy (or level; E_F) and the vacuum level (E_{vac}). Physically, it is the minimum energy required to remove an electron from a solid to a point immediately outside the solid surface. In addition for the semiconductor, there is an electron affinity (χ_{sc}) term which is the energy difference between the conduction band minimum (CBM) and the E_{vac}.

When the metal and semiconductor are directly adjacent to each other (*i.e.*,
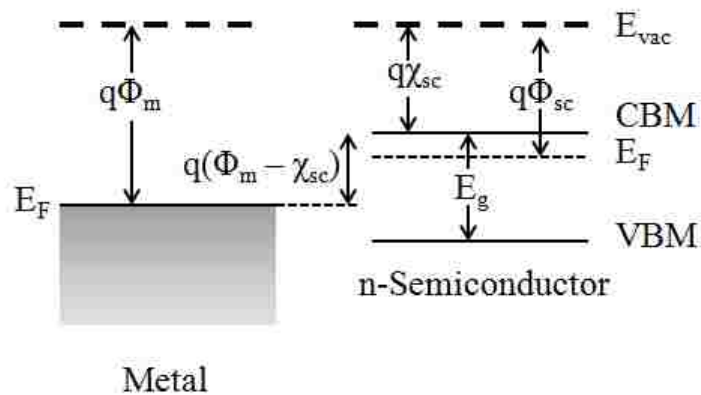
Fig. 2.1: Energy band diagram of an isolated metal next to an isolated n-doped semiconductor under nonequilibrium conditions (adapted from [8]).

thermal equilibrium), the E_F must be equal (*i.e.*, line up). The energy diagram for a metal and semiconductor in equilibrium with each other is shown in Fig. 2.2. In an ideal case, the barrier height (Φ_B) is defined as the difference between the metal work function and the electron affinity of the semiconductor. In order to accommodate the equilibrium conditions, the conduction band bends upwards. The height of this potential, seen by the electrons in the conduction band of the semiconductor moving to the metal, is: $V_{bi} = q(\Phi_m - \chi_{sc})$. When the barrier height (Φ_B) is much larger than kT (*i.e.*, thermal energy), a Schottky barrier is present. In this case, the metal-semiconductor interface behaves similarly like a diode.

In contrast to Schottky barriers, an Ohmic contact is defined as a metal-semiconductor contact that has negligible (*i.e.*, very low) resistance relative to the bulk resistance of the semiconductor regardless of the polarity of the applied voltage. Semiconductor devices and integrated circuits need Ohmic contacts to make connections to other components and devices in a larger electrical system. For an Ohmic contact, the contact resistance is exponentially proportional to the barrier height Φ_B. Thus, when selecting an appropriate contact metal onto a semiconductor, it is essential to minimize
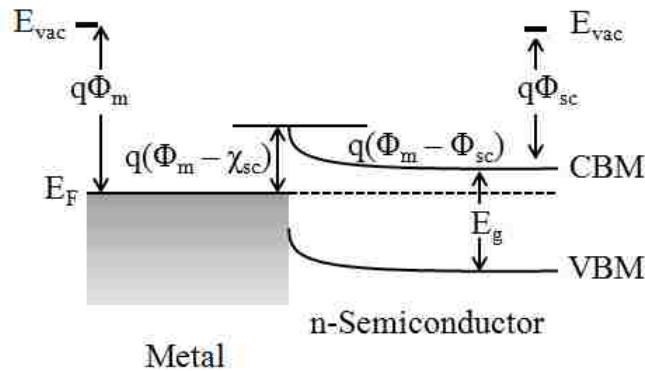
Fig. 2.2: The energy diagram of a metal-semiconductor contact in thermal equilibrium (adapted from [8]).

the difference between the metal's work function and the semiconductor's electron affinity. The above cases are ideal and simplified scenarios, and often times, these concepts are not as simple in practice. Hence, there is a drive to optimize contact metals and formation such that the final electronic device does not degrade in performance.

For (Al,Ga)N alloys, there is a desire to find one contact scheme for the entire composition of the alloy. V-based contacts to n-type GaN and n-AlGaN alloys have shown to have Ohmic properties [9, 10] at lower annealing temperatures [9]. Since Galesic and Kolbesen demonstrated the "nitridation" of metallic vanadium films (*i.e.,* the formation of VN) by rapid thermal annealing (RTA) in N_2 atmosphere [11], it has been hypothesized that VN is also formed at the interface between V-based contacts and n-$Al_xGa_{1-x}N$ after RTA treatment [10].

2.2 Heterojunction Formation in Solar Cells

A solar cell diode is made by forming p-n junction, which is when p- and n-type semiconductor materials are joined adjacent to each other. In Fig 2.3a, the energy diagram of an isolated n-type and p-type semiconductor is shown. When the two
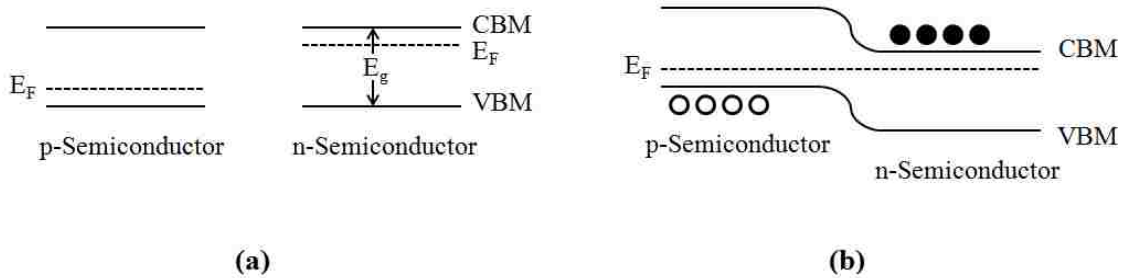
Fig. 2.3: A p-type and n-type semiconductor (a) isolated from each other, and (b) adjacent and in thermal equilibrium. In (b), the majority carriers in the p-type material (*i.e.*, holes) and n-type material (*i.e.*, electrons) are shown (adapted from [8]).

materials are brought together, thermal equilibrium requires that the E_F in both the p-type and n-type material be the same. The p-n junction in equilibrium is shown in Fig. 2.3b where the respective majority carriers in each material are illustrated as well. The p-n junction can be of the same material (homojunction, *e.g.*, silicon) or of different materials (heterojunction, *e.g.*, CdS/CdTe). In the case for Cu-based chalcopyrite solar cells, the p-type $Cu(In,Ga)Se_2$ (or "CIGSe") is joined with the intrinsic (i) ZnO and n-type ZnO. However, for high-efficiency solar cells, a CdS buffer layer is necessary between the CIGSe absorber and the i-ZnO/n-ZnO layers. The typical device structure of the CIGSe solar cell is shown in Fig. 2.4 [12]. In the figure, the molybdenum (Mo) back contact is between the glass substrate and CIGSe absorber. In a solar cell, when the sunlight (hv $\geq$ E_g) excites an electron from the valence band into the conduction band, it leaves behind a 'hole.' The holes move towards the back contact (*i.e.*, the p-doped material), while the electrons move in the opposite direction towards the front contact (*i.e.*, the n-doped material). The p-n junction of an idealized solar cell (upon illumination) is shown in Fig. 2.5 where the direction of the charge carriers are indicated.
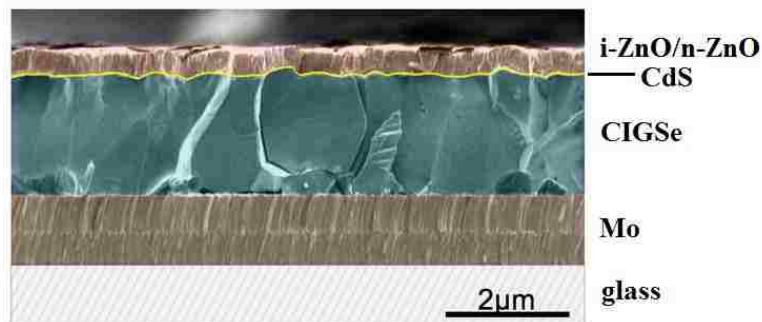
Fig 2.4: A colored, cross-sectional view of a typical NREL CIGSe-based solar cell [12].
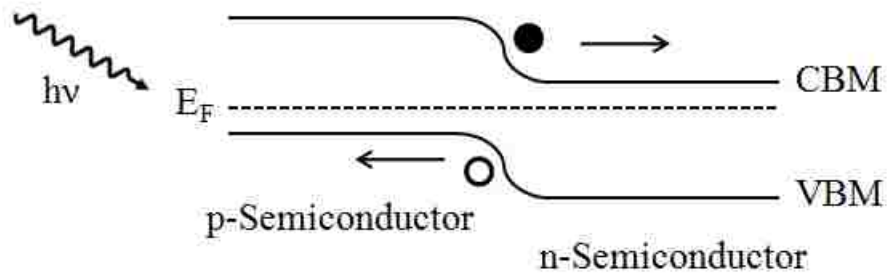
Fig. 2.5: A p-n junction for typical solar cell where the directions of the carriers are shown (adapted from [8]).

One of the factors associated with optimizing CIGSe-based solar cells is the electronic structure between the CIGSe absorber and CdS layer (*e.g.*, the conduction band offset (CBO)). This interface is plays a dominant role, and is often the focus for optimization. The conduction band alignment (and subsequently the CBO), is important for the transport of the (photogenerated) electrons to the front contact. There are three configurations for the conduction band to align in this heterojunction: "spike", "flat", or "cliff" configurations. This is schematically shown in Fig. 2.6. The CBO for the CdS/CIGSe has been reported as having a "cliff" heterojunction [13]. However, the electronic level band-alignment was directly experimentally determined for other Cu-containing chalcopyrites and CdS for $CuInSe_2$ [14], $CuIn(S,Se)_2$ [15], and $Cu(In,Ga)S_2$ [16]. In the case for the $CdS/CuIn(S,Se)_2$ [15] and $CdS/CuInSe_2$ [14] heterojunctions, the conduction band alignment was experimentally shown to be "flat." While for the $CdS/Cu(In,Ga)S_2$ [16], the conduction band alignment was determined to be unfavorable with a "cliff" configuration. The band alignment at the absorber interface is one of the key components to understand as it may provide information for further optimization of the entire solar cell.

9
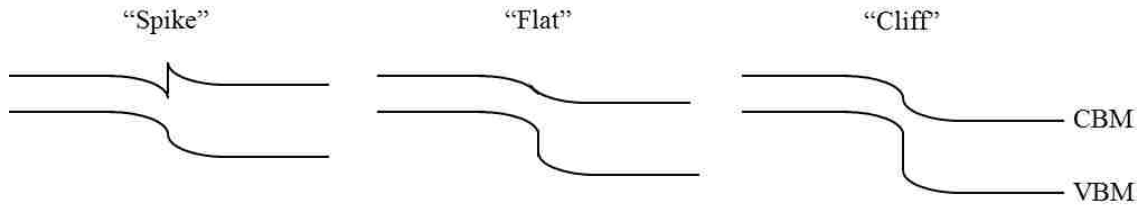
Fig. 2.6: The three different possible heterojunction alignments: "spike," "flat," and "cliff."

2.3 Post-absorber Deposition Treatments on CdTe

Another promising second generation thin-film technology is based on CdTe/CdS solar cells. Typically, a CdTe/CdS solar cell is made in superstrate configuration where the front contact is adjacent to the glass (as shown in Fig. 2.7, adapted from [12]). The CdS/CdTe layers are deposited onto SnO_2:F coated soda lime glass. A cadmium chloride ($CdCl_2$) treatment or "activation" is commonly performed at this manufacturing step. The $CdCl_2$ activation is performed by exposing the CdTe/CdS stack to $CdCl_2$ dissolved in
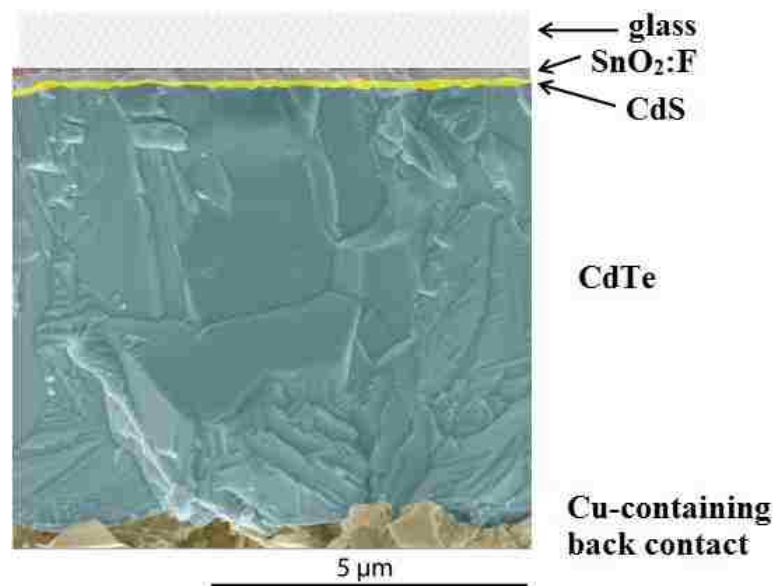
Fig. 2.7: A SEM cross-section image of a CdTe/CdS solar cell (from [12]).

methanol in a heated environment [17]. This post-absorber treatment is commonly accepted and performed since there are correlations of it enhancing the overall devices efficiency [18].

After the CdCl$_2$ activation, the back contact is deposited and an additional heat treatment is performed to form the Ohmic contact [19, 20]. The back contact typically consists of Cu, and in this work, Au/Cu contacts were investigated. Numerous studies (*e.g.*, Ref. [20-22]) have reported diffusion processes at different interfaces in CdTe cells as a result of post-absorber deposition treatments. With a design of a combinatorial sample set that allows the effects of each post-deposition treatment to be separated, many characterization techniques are used to paint a complementary, non-destructive picture of the back contact morphology and chemical interface structure of CdTe-based solar cells as a function of post-deposition treatment.

CHAPTER 3

EXPERIMENTAL METHODS

This chapter presents the experimental techniques, apparatus, and sample preparation that were utilized. The central characterization technique that was used to study the chemical and electronic structure of the materials' surface was photoemission. Complementary techniques such as synchrotron-based X-ray Emission Spectroscopy provided chemical information from buried interfaces. Microscopy was also performed, and provided structural information in conjunction to the spectroscopic results.

3.1 Photoemission

Photoemission spectroscopy (PES) is the most common and important technique used for studying the electronic and chemical structure of solids. PES is based on the photoelectric effect which was first experimentally discovered by Heinrich Hertz in 1887, and later explained by Albert Einstein in 1908. In direct PES, ultraviolet or X-ray photons irradiate a sample surface and eject photoelectrons from the occupied electronic states, and thus provides information of the occupied density of states (DOS). Inverse photoemission (IPES) utilizes electrons (with predefined, known energies) aimed at the sample surface which relax into unoccupied electronic states and emit photons (and thus provides the unoccupied DOS). UV PES (or UPS) and IPES can be combined to provide the electronic structure of a material such as the energy band gap (E_g).

3.1.1 Direct Photoemission

Photoelectron spectroscopy is a very powerful and commonly used technique. In this technique, the kinetic energy (E_{kin}; with respect to the E_F of the analyzer) of the ejected

photoelectrons are measured to infer the occupied energy level (thus *occupied* density of states (DOS)) in which they originated from. The term photoemission and photoelectron spectroscopy will be used interchangeably.

Physically, the photoemission uses incident photons with energy $h\nu$ to excite and eject electrons from occupied electronic states. The intensity of the photoelectrons is proportional to the transition probability given by Fermi's golden rule [23]

$$P(\psi_f, \psi_i) \propto |\langle \psi_f | \hat{H} | \psi_i \rangle|^2 \, \delta \left(h\nu - (E_f - E_i) \right)$$

where ψ_f and ψ_i are the wavefunctions of the initial and final states, respectively, $\hat{H}$ the transition operator, and the δ-function for energy conservation. A schematic of the photoemission process and its measurement is shown in Fig. 3.1.

X-ray Photoelectron Spectroscopy (XPS) is well suited for investigating the core electronic levels in a sample. The laboratory X-ray source has a dual cathode where either Mg $K_{\alpha1,2}$ (1253.6 eV; 1s $\rightarrow$ 2p transition) and Al $K_{\alpha1,2}$ (1486.6 eV; 1s $\rightarrow$ 2p transition) were used. Ultraviolet Photoelectron Spectroscopy (UPS) is more suited for studying the filled electronic states in the valence band. XPS could be used, but the electrons from the valence band have a low photoelectron cross section and the kinetic energies of these valence electrons are high. Any photon energies between $4 - 150$ eV could be used for UPS. In this work, a He discharge lamp was used and subsequently the He I (21.22 eV; $1s^2 \rightarrow 1s2p$ transition) and He II (40.81 eV; 1s $\rightarrow$ 2p transition) excitations were utilized. PES is a surface-sensitive technique as the information depth depends on the ejected photoelectrons arriving to the electron spectrometer. The number of photoelectrons that escape from the sample (and thus are detected) is proportional to a decaying exponential function which depends on the depth below the surface. The
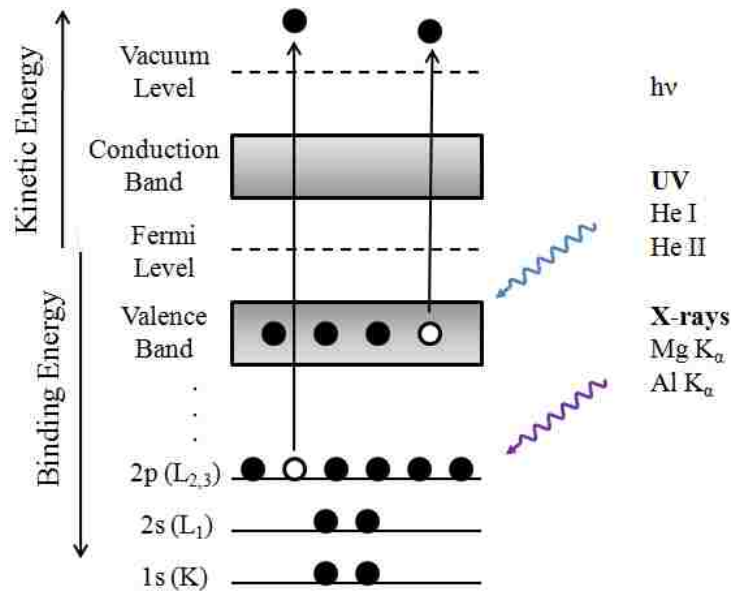
Fig. 3.1: A schematic drawing of the physical process involved with XPS and UPS. X-ray or UV photons irradiate the sample and a (photo)electron is ejected. The kinetic energy (E_{kin}) of the photoelectron is measured by the electron analyzer.

inelastic mean free path (IMFP or escape depth) of electrons as a function of kinetic energy is shown in Fig. 3.2 [24].

PES experiments were primarily performed in the "Andere ESCA" machine which utilized a SPECS PHOIBOS 150 MCD hemispherical analyzer. XPS and UPS measurements utilized a dual anode X-ray source and a helium discharge lamp, respectively. The energy scale of the electron analyzer for XPS measurements were calibrated according to Ref. 25 using the PES and Auger lines of clean Au, Ag, and Cu. PES spectra were recorded in fixed analyzer transmission mode where the pass energy remains fixed for the collection of a spectrum. The pass energy is the energy which the photoelectrons are slowed to a constant energy as they enter the electron analyzer. The relative resolution, $\Delta E/E_{pass}$, is proportional to s/R_0 where ΔE is the absolute resolution,
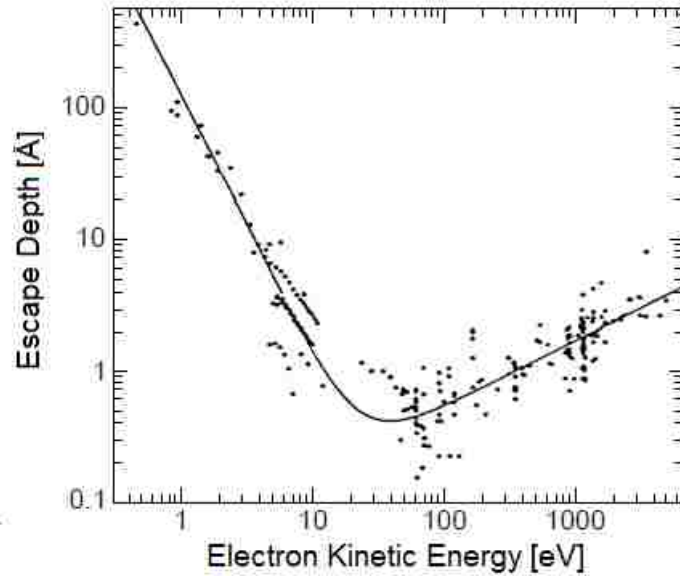
Fig. 3.2: The inelastic mean free path (or escape depth) of electrons as a function of their kinetic energies. The points represent data compiled experimentally. This figure is adapted from Ref. 24.

E_{pass} is the pass energy, s is the mean slit width, and R_0 is the analyzer radius. Thus, for a fixed R_0 and selected s, the pass energy E_{pass} must decrease for better experimental resolution. The experimental resolution, as determined by fitting clean the Au 4f PES lines and Fermi edge, with XPS (E_{pass} = 20 eV) and UPS (E_{pass} = 1 eV) are 0.4 eV and 0.1 eV, respectively.

The experiments were performed in vacuum due to three main reasons: (i) the surface composition of the sample must not change during the experiment, (ii) the photoelectrons ejected from the sample must travel through the analyzer without colliding with other particles, and (iii) some experimental components require vacuum conditions to be operational (*e.g.*, soft X-ray source). The first reason requires the need for ultra-high vacuum (UHV; P < 10^{-9} mbar) as opposed to high vacuum (10^{-4} – 10^{-9} mbar). In the kinetic theory of gases, the ratio of adsorbed particles to the number of free

particles at various pressures can be determined. At a pressure of 10^{-6} and 10^{-11} mbar, the ratio of absorbed particles to the number of free particles is 10^4 and 10^9, respectively. The mean free path λ (*i.e.,* average path each particle travels between collisions) is inversely proportional to number density of molecules present where the latter is directly proportional to the gas pressure.

3.1.2 Inverse Photoemission

Inverse photoemission spectroscopy (IPES) is the inverse process of PES. Here, electrons are impinged onto the surface of a sample and the incident electrons decay into unoccupied electronic states and emit photons. This process is shown schematically in Fig. 3.3. From this technique, the spectrum of *unoccupied* DOS is obtained and the conduction band minimum (CBM) can be determined. The electron source is a low energy electron gun using thermionic emission from a filament (STAIB). The energy of the electron gun is varied (E_{kin}: $6 - 16$ eV), and when an electron relaxes into an unoccupied state in the conduction band, a photon is emitted. The detector used for the IPES experiments is similar to a Geiger-Müller counter. The detector consists of a SrF_2 entrance window to a tube with $Ar:I_2$ filling and high-voltage rod. The window and I_2 filling serves as the high and low energy detection limits, respectively. The SrF_2 window does not transmit radiation with energy greater than 9.8 eV [26]. While the lower detection limit is determined by the threshold for the molecular photoionization of iodine,

$$I_2 + h\nu \rightarrow I_2^- + e^-$$
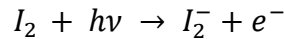
at 9.37 eV [27]. Thus, the photons are detected in isochromat-mode as a function of electron energy. However, the ratio of cross section of IPES to UPS is about 10^{-5} which makes it a more difficult experiment [28]. Energy calibration is performed by measuring
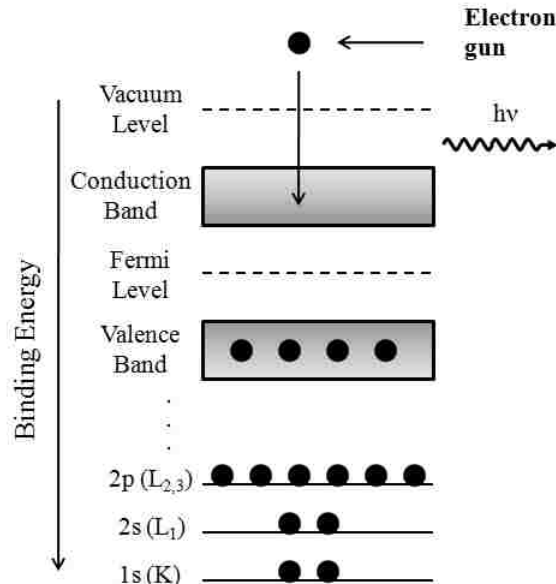
Fig. 3.3: Schematic energy diagram of the IPES process. An electron source impinges electrons (of varying E_{kin}) to the surface of a sample, where the electron relaxes into a lower unoccupied state and emits a photon.

the Fermi level of a clean Au foil, and all subsequent spectra are referenced to the Fermi level. The IPES experiments were also performed in the analysis chamber of the Andere ESCA. The experimental resolution, as determined by the Fermi fit of clean Au foil, for this particular IPES set-up is about 0.3 eV.

3.1.3 Combining UPS and IPES results

The surface band gap (E_g) of a material is experimentally determined by combining the information of the VBM (by UPS) and CBM (by IPES). Both of these techniques are very surface-sensitive since the information depths are 2 - 4 nm based on the approximate IMFP shown in Fig. 3.2 [24]. The band edges (VBM and CBM) are determined by linear extrapolation that intersects the baseline. At this intersection, a state may not necessarily exist at that energy level, but this is the best approximation for the uppermost state (for

17

the valence band). Other arguments for the linear extrapolation method include non-symmetric broadening towards higher E_B from: downward dispersion of the VBM in all directions in reciprocal space, the inelastic scattering process (*e.g.*, photons and electrons), and the possibility of incomplete screening of a core hole [29]. The linear extrapolation procedures are justified experimentally for determining the E_g (*e.g.*, Ref. 14, 15). The electronic surface E_g may be different from bulk E_g measurements since the surface composition of a material could be different compared to the bulk phase. However, the surface electronic properties of materials are key pieces for successful materials incorporation into devices (*i.e.*, their interfaces). The electronic energy levels of the VBM and CBM are essential pieces to understand the electronic properties of a material, and are required for deeper insight into device physics.

3.1.4 X-ray Excited Auger Electron Spectroscopy

While undergoing XPS experiments, X-ray excited Auger electron spectroscopy (XAES) is also performed. When a core hole is created by X-ray photons, one mechanism for the relaxation of the core hole is by the Auger process. In the Auger process, an electron from an outer energy level (*i.e.*, of less binding energy) relaxes into the core hole. An energy difference arises due to that transition, and the energy can either be absorbed by another electron and as a result be ejected or emitted as a photon. The first process is the Auger emission, while the second process is X-ray fluorescence (or emission; see 3.2.1) The XAES process is shown schematically in Fig. 3.4 for an oxygen atom. The ejected Auger electron is also detected by the electron analyzer. The notation for an XAES transition includes information from all three electrons involved, and follows traditional X-ray spectroscopic notation. For example, the O $KL_{2,3}L_{2,3}$ XAES line consists of the
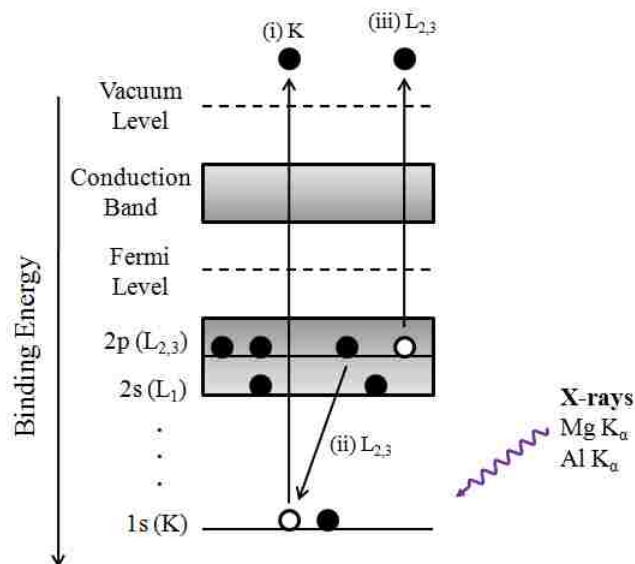
Fig. 3.4: Schematic drawing of the XAES $KL_{2,3}L_{2,3}$ transition for an oxygen atom. First, a core hole is created when X-ray photons eject a 1s electron (i). Next, an outer energy level electron (2p) relaxes to that core hole (ii). The energy difference from step (ii) is absorbed by another outer electron (2p) which is sufficient energy for it to be ejected (iii).

core hole created in the 1s level (*i.e.,* K), an electron that relaxes to that core hole from the 2p level (*i.e.,* $L_{2,3}$), and the detected electron (also) from the 2p. In general, XAES line shapes can be very indicative of the chemical environment since the electron emitted (associated with the XAES spectrum) are typically valence electrons.

3.1.5 The Modified Auger Parameter

The modified Auger parameter (α') is determined by the sum of the positions of a PES and a XAES line. This value is typically tabulated for the most intense (*i.e.*, prominent) PES and XAES lines of a particular element [30, 31]. The α' value can be used to identify and distinguish different chemical environments of a particular element. Since the value is the sum of a PES and XAES lines (in E_B and E_{kin}, respectively), the α' value is

independent of energy shifts due to sample charging, interface-induced band bending, and calibration of the analyzer.

3.1.6 Curve Fitting

Curve fitting is frequently performed as a form of data analysis for XPS data. The experimentally acquired XPS spectra are fitted to a series of theoretical curves as an effective means to compare the experimental data with an expected spectrum. Spectra are typically fitted with either Voigt or Doniach-Šunjić (DS) lineshapes with a linear background. The Voigt lineshape is commonly used in all branches of spectroscopy, and is broadened by Gaussian and Lorentzian functions. Broadening arising from the experimental instruments (*e.g.*, line width of the excitation energy) is best described with a Gaussian function. While broadening due to intrinsic properties of the transition (arising from the uncertainty principle) is best described with a Lorentzian lineshape. Thus, the experimentally acquired spectrum will have a lineshape that is a convolution of a Gaussian and a Lorentzian. Both the Lorentzian and Gaussian functions are symmetric about their center, and the maximum value of the function is at the center. The full-width at half-maximum (FWHM) of the Gaussian contribution is commonly used as a measure for the experimental resolution of the experiment. The spectral shape of metals are sometimes best described by a DS lineshape which is asymmetric in the high E_B part of the range which has resulted from fast photoelectrons undergone inelastic many-electron interactions [32] before their detection in the electron analyzer. The DS line shape displays a high E_B tail.

Spectral fitting was performed with Fityk software which iteratively refines the fit by the least squares method, and the chi-squared value determines the quality of the fit.

The chi-squared value is related to the square of the residuum of the fit. Here, the residuum is defined as the overall (or addition) fit subtracted from the experimental data. The quality of the fit is also determined by constraints and parameters chosen. For fitting spin-orbit doublet peaks, the ratio of the peak areas is held to the physical constraint that,

$$\frac{I(nl_{l+s})}{I(nl_{l-s})} = \frac{l + s + \frac{1}{2}}{l - s + \frac{1}{2}}$$

where l is the angular momentum number, s is the spin ½, and I is the area intensity of the peak nl_{l+s} (*e.g.*, $2p_{3/2}$). Also, when possible, the spin-orbit separation was also fixed using literature values (*e.g.*, Ref. 31). For simultaneous spectral fits of the same PES line of different samples, the Gaussian FWHM were fixed if the measurements were acquired for identical spectrometer and excitation settings. Also, the number of lineshape functions introduced into a fit should be minimized and only introduced if there is a physical explanation (such as an additional identifiable chemical state).

3.2 Synchrotron-based X-ray Spectroscopies

A substantial amount of data presented in this dissertation was acquired at a synchrotron. A synchrotron provides a tunable-energy photon source (*e.g.*, from the infrared to the hard X-ray regime), and of a photon source with high photon flux (*e.g.*, about three orders of magnitude greater than a conventional laboratory X-ray source). Synchrotron radiation is electromagnetic radiation emitted by electrons moving on a circular orbit with nearly relativistic velocity. In this work, X-ray emission spectroscopy (XES) and photoemission electron microscopy (PEEM) were performed at a synchrotron.

3.2.1 X-ray Emission Spectroscopy

As mentioned in the previous sections, photons are used to eject a core electron, thus leaving "behind" a cole hole. The core hole can be relaxed by either the non-radiant Auger decay (see section 3.1.4) or radiant fluorescence (*i.e.*, X-ray emission) process. As seen in Fig. 3.5, the Auger decay process dominates for lighter elements (atomic number < 20) for K-shell (*i.e.*, n=1) core holes [33]. However, due to the much greater flux of photons at a synchrotron and the design of high-efficiency spectrometers, experiments utilizing the fluorescence decay are now on a comparable measurement time-scale to that of laboratory-based spectroscopic techniques. In the fluorescence process, the core hole is filled by an electron from an outer energy level (*i.e.*, either a valence or core electron), and the energy difference from this transition is emitted as a photon. This process is illustrated in Fig. 3.6. The X-ray emission process obeys the dipole selection rule, $\Delta\ell = \pm$
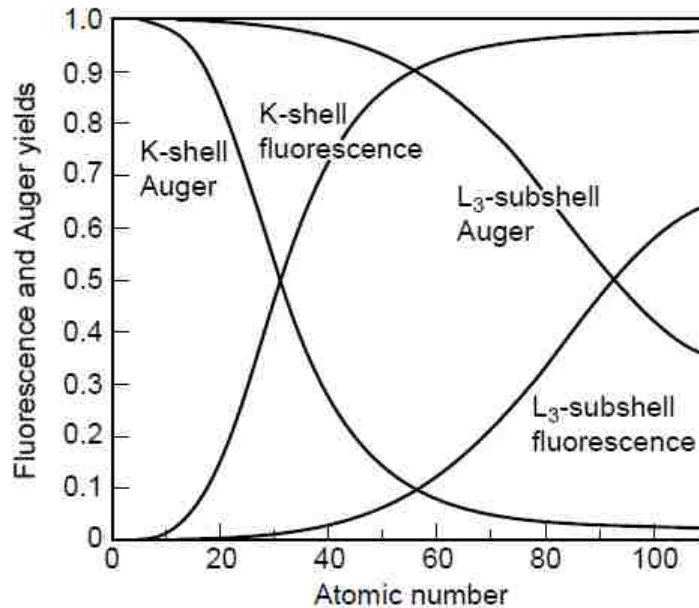
Fig. 3.5: The yields for competing fluorescence and Auger relaxation processes for a photoexcited core hole [33].

22
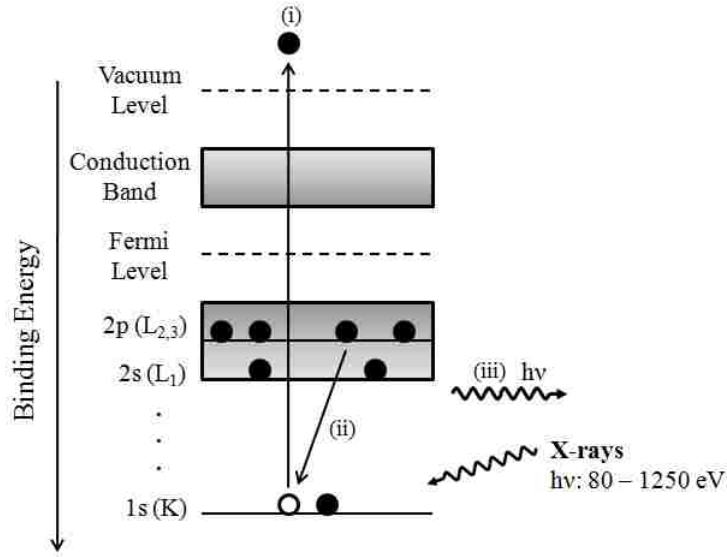
Fig. 3.6: Schematic energy diagram of the X-ray emission process. Note that the (ii) transition obeys the dipole selection rule.

1, where ℓ is the azimuthal (or angular momentum) quantum number. The intensity of the emitted photons in XES also follows Fermi's golden rule as,

$$P(\psi_f \psi_i) \propto |\langle \psi_f | \hat{H} | \psi_i \rangle|^2 \, \delta \left(h\nu - \left(E_i - E_f \right) \right).$$

In addition, the intensity of the XES signal is also dependent on the exponentially attenuated intensity of the incoming photon and outgoing photon. X-ray attenuation lengths through many types of materials are tabulated [34]. XES experiments can be tuned (by selecting a suitable photon energy) to a specific "edge" of an element (*i.e.*, energy level) such as the K-edge (1s). Like PES, XES probes the occupied density of states of a particular element. This technique paints an element-specific partial density of states electronic picture, while XPS, UPS, and IPES portrays the *total* density of states.

XES experiments were performed on Beamline 8.0.1 at the Advanced Light Source (ALS), Lawrence Berkeley National Laboratory. At Beamline 8.0.1, the
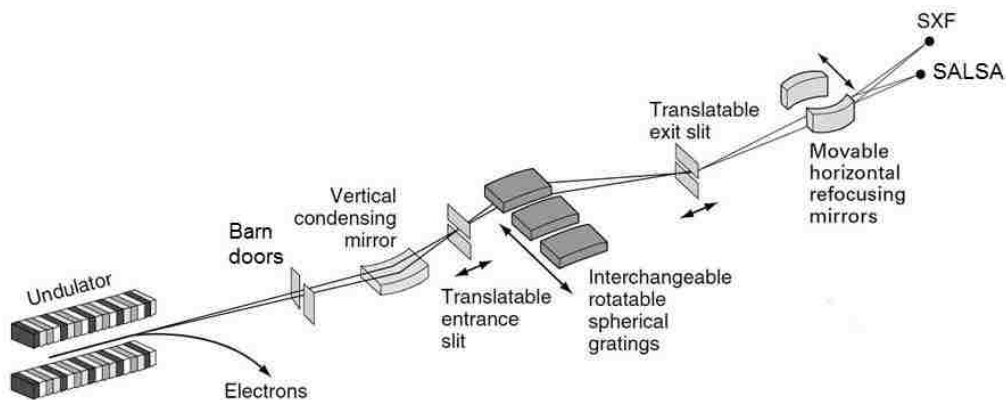
Fig. 3.7: A schematic layout of the synchrotron radiation path in Beamline 8.0.1 at the ALS [35].

synchrotron radiation exits an undulator, then passes through the barn doors, the first vertical focusing mirror, the entrance slit, monochromator spherical grating, the exit slit, and finally a re-focusing mirror to direct the beam. The set up (including optical elements) used in Beamline 8.0.1 is shown in Fig. 3.7 [35]. The experiments were performed in either the permanently installed Soft X-ray Fluorescence ("SXF") endstation [36] or the Solid and Liquid Spectroscopic Analysis ("SALSA") endstation [37]. The SXF spectrometer has a spectral resolution $E/\Delta E$ between $400 - 1900$. In SALSA, the high-efficiency variable line spacing (VLS) spectrometer was used, and has a spectral resolution of $E/\Delta E > 1200$ over the whole energy range $(120 - 880\ eV)$ [38].

3.2.2 Photoemission Electron Microscopy

Photoemission electron microscopy (PEEM) is a laterally-resolved, elementally- and surface-sensitive technique. Using either X-ray or UV photons, PEEM combines elements of PES with a high-resolution microscope where it detects electrons emitted

from a sample in a laterally-resolved fashion. Thus, in contrast to XPS, XAES, and XES, PEEM provides a spatial, occupied DOS map of the (near) surface.

To move the photoelectrons from the sample surface to the microscope, a strong electrostatic field (~ 20 kV) is applied between the sample and the first electrode (extractor) in the electron emission microscope. The resulting image is magnified by a series of electrostatic electron lenses.

UV excitation by a Hg discharge lamp (4.9 eV; $6s^2 \rightarrow 6sp$ transition) was used to study the topography and local variation of the work function of the sample. Tunable, soft X-ray excitation was used for PES-based PEEM. In PES PEEM experiments, the 'images', that resulted from energy differences, were used. For example, if a sample contained a non-homogenous surface distribution of Au, then an image of the "peak" (*i.e.*, on the PES peak) and an image of the "pre-peak" (*i.e.*, the background at higher E_{kin} or lower E_B) were obtained. Next, the "pre-peak" image was subtracted from the "peak" image, then the resulting image is divided by the "pre-peak" image, and this is the final image. This method allows less dependence on the accuracy of the energy filters of the microscope. PEEM experiments were performed at the BESSY II facility of the Helmholtz-Zentrum Berlin on beamline UE49 with a commercial photoelectron microscope.

3.3 Atomic Force Microscopy

The surface topography of samples was investigated by contact-mode atomic force microscopy (AFM) in air. The schematic drawing of the working principle of an AFM is shown in Fig. 3.8 [39]. The cantilever with a tip is brought to the vicinity of the sample
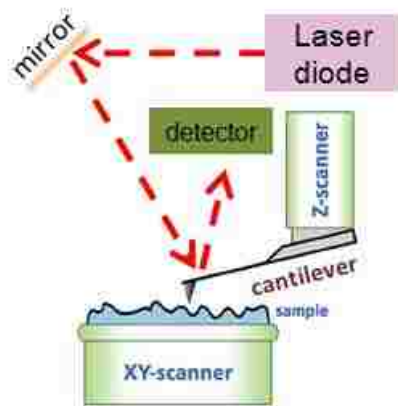
Fig. 3.8: Schematic of an atomic force microscope [39].

surface, and the interatomic forces between the tip and the sample cause the deflection of

the cantilever due to Hooke's law. The deflection is measured by the laser which is

focused onto the cantilever and reflected onto a position-sensitive photodiode (PSPD).

The slight changes in deflection of the tip will cause the reflected laser spot onto the

PSPD to move slightly, which translates to a topographic image as the cantilever scans

line by line on a sample surface. In contact mode, the tip is scanned above the sample

surface such that a constant force between the tip and sample is maintained (through a

feedback control loop). AFM measurements were performed by a Park XE-70

instrument. Image processing was performed by Park XEI software.

3.4 Sample Preparation

The preparation of relatively clean surfaces is an essential aspect of surface to surface-

near bulk sensitive measurements. Contamination of samples can result to inaccurate

measurements of surface-sensitive information such as the VBM and CBM levels, and

surface E_g. Contamination in the form of a native oxide layer can also cause the surface of samples to be non-conductive where conductivity is an essential criterion for PES-based measurements.

3.4.1 Chemical Etching

Chemical etching by way of acid or base can provide a facile method for preparing clean surfaces. Acids are commonly used for etching native oxides on metals. In this work, aqueous ammonia was commonly used to etch native oxide from (Al,Ga)-nitride [40] and CIGSe [41] surfaces.

3.4.2 Ion Treatment

Although etching may be effective for removing a significant portion of contamination, typically low energy ion sputtering will be necessary as the final step on preparing a surface for experiments. Ions of inert gases (*e.g.*, Ar or N_2) are used at low energies (typically 50 -100 eV), and directed to the sample surface. Energy between the ions and atoms at the surface of the sample are exchanged after successive collisions, where the end result causes the ejection of atoms. The low energy gas ions ensure that the sputtering occurs below the sputter threshold [30], where the effects of preferential sputtering are minimized. Ar and N_2 gases of high purity (> 99.9999%) were used. Ion treatments were performed in the Andere ESCA's preparation chamber with either a Vacuum Generator Ex05 or Nonsequitur Technologies 1402 ion source.

CHAPTER 4

CONTACT FORMATION ONTO n-GaN

4.1 Introduction

III-nitride semiconductors are important materials because of their increased use in optoelectronic devices such as light emitting diodes. Their performance depends on a low contact resistance. Thus, forming Ohmic contacts to nitrides is critical. Traditionally, Ti-based contacts were used [42]; more recently, good (*i.e.*, Ohmic) V-based contacts to n-type GaN and n-AlGaN alloys result in better contact resistances [9, 10] at lower annealing temperatures [9]. Since Galesic and Kolbesen [11] demonstrated the "nitridation" of metallic vanadium films (*i.e.,* the formation of VN) by rapid thermal annealing (RTA) in N_2 atmosphere, it has been hypothesized that VN is also formed at the interface between V-based contacts and n-$Al_xGa_{1-x}N$ after RTA treatment [10]. VN is stable [43] and has a low work function [44], thus it is suitable to form Ohmic contacts to n-GaN (whose electron affinity is about 4.0 eV) and n-$Al_xGa_{1-x}N$ (whose electron affinity is less than 4.0 eV) [45]. It was found that $Al_xGa_{1-x}N$ samples need higher RTA temperatures than pure GaN samples for optimal contact resistance [10]. It is speculated that VN is formed at lower temperatures for GaN (or greater Ga content in the alloy) [10], presumably since the bond lengths in GaN are longer than in AlN [46], and hence the bond is expected to be weaker.

The interface between the nitride layer and metal contacts after heat treatment has previously been investigated by (among others) energy dispersive x-ray spectroscopy [47, 48], glancing-angle x-ray diffraction [48], and Auger electron spectroscopy sputter depth profiling [48, 49]. A detailed photoemission investigation of the interface chemistry

between low work function metals and GaN was performed by Wu and Kahn [50]. However, the chemical properties of the interface between *V-based contacts* and GaN, in particular the potential formation of VN, have yet to be explored. We have used chemically-sensitive, laterally-integrating techniques such as X-ray emission (XES), X-ray photoelectron (XPS), and X-ray excited Auger electron (XAES) spectroscopies, to investigate the interface formation between Au/V/Al/V metal contact scheme and n-GaN before and after RTA treatment. In addition, we have used laterally-resolved characterization of the surface microstructure after contact formation by RTA. Atomic force microscopy (AFM), wavelength-dispersive spectroscopy (WDS), and core-level-specific photoemission electron microscopy (PEEM) were utilized to investigate the RTA-treated contact structure.

4.2 Experimental Details

Si-doped GaN samples were grown on c-plane sapphire wafers by molecular beam epitaxy. The samples were chemically treated and V-based contacts were deposited by electron beam evaporation [10]. Two sets of metal contacts were analyzed (referred to as "thin" and "thick"): V(15Å)/Al(80Å)/V(20Å)/Au(100Å) and V(150Å)/Al(800Å)/V(200Å)/Au(1000Å), respectively. Both the thin and thick contacts on n-GaN were annealed by RTA at 650°C for 30 seconds in N_2 atmosphere. The specific contact resistivity was found to be on the order of 10^{-6} Ω cm^2 [10].

All samples were sealed in inert atmosphere at Boston University and loaded into ultra-high vacuum (UHV, base pressure in the 10^{-10} mbar range) at UNLV via a N_2-filled glove box (*i.e.*, avoiding any air exposure). We have used surface sensitive XPS, x-ray

XAES, and surface-near bulk sensitive XES to investigate the interface between a V/Al/V/Au metal contact scheme (where Au is the top-most layer) and n-GaN before and after RTA treatment. XPS and XAES were performed using Mg K_α and Al K_α radiation and a Specs PHOIBOS 150MCD electron analyzer. The electron spectrometer was calibrated using XPS and Auger line positions of Au, Ag, and Cu [25]. XES was performed at the Advanced Light Source (ALS), Lawrence Berkeley National Laboratory, on Beamline 8.0.2. using a variable line spacing spectrometer [38]. The energy resolution is E/ΔE>1200 and the spectrometer was calibrated using elastic scattered peaks at different energies (Rayleigh lines). For the XES experiments, the samples were briefly exposed to air prior to introduction into UHV.

Contact-mode AFM measurements were conducted with a Park XE-70 instrument in air. WDS was performed at the UNLV Electron Microanalysis and Imaging Laboratory with a JEOL JXA-8900 electron probe microanalyzer (after air exposure of the sample). PEEM experiments were performed at HZB's BESSY II facility on beamline UE49 using an Elmitec instrument and ultraviolet (UV, Hg discharge lamp) or soft X-ray excitation. For the surface-sensitive PEEM experiments, native oxides [40] and surface contaminants due to air exposure were removed by etching in aqueous ammonia solution (15 vol%) for 10 minutes at room temperature in an N_2-purged glovebox, rinsing with deionized water (1-2 minutes), and reloading into the ultra-high vacuum (UHV) PEEM chamber while minimizing air exposure to the surface. Subsequently, Ar^+ sputtering (250 eV, 4 $\mu A/cm^2$) was performed for 15 minutes.

4.3 Results and Discussion

4.3.1 Chemical structure of the contact formation

Before RTA treatment, the XPS survey scans (Fig. 4.1) of the n-GaN/V/Al/V/Au samples are dominated by Au features, as expected. After RTA treatment, elements from initially buried layers (*e.g.*, V, Ga, and N) can be observed in the survey scans. The survey spectra of the RTA-treated samples suggest that the heat treatment either induces the diffusion of once buried elements to the surface or that the contact metals "open" to reveal the once buried elements. AFM images (see section 4.3.2) indicate a vein-like network after RTA treatment, suggesting that the contact layers have agglomerated into veins and that
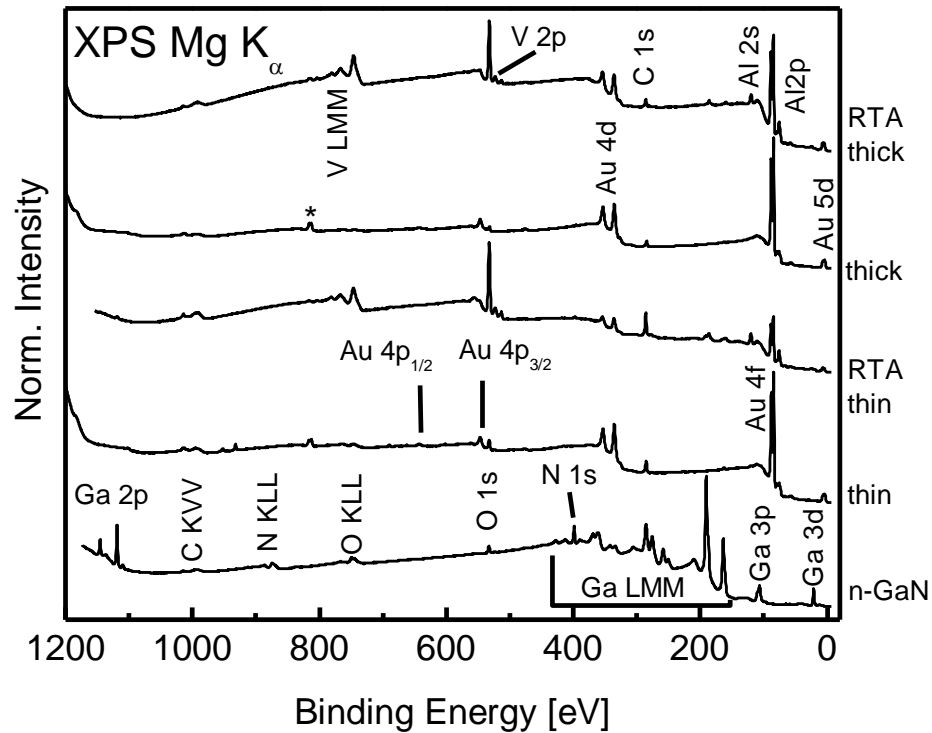
Fig. 4.1: XPS Survey spectra of the thick and thin contact samples before and after RTA treatment. Reference n-GaN spectrum is also shown. The asterisk denotes the Au 4f lines excited by O K$_\alpha$.

emission from initially buried layers can be observed from regions in-between the veins.

The Ga $2p_{3/2}$ XPS and Ga $L_3M_{4,5}M_{4,5}$ XAES detail spectra from the bare (*i.e.,* contact free) n-GaN and the RTA-treated thick and thin samples are shown in Fig. 4.2a and 2b, respectively. The Ga spectral features differ between the RTA-treated thick and thin samples, and both deviate significantly from the corresponding bare n-GaN reference. The Ga $2p_{3/2}$ lines (Fig. 4.2a) of the RTA-treated samples are broader (than the n-GaN line). Furthermore, the thick RTA sample shows a pronounced shoulder at higher binding energies which is attributed to the presence of (at least) a second Ga species. We have thus performed a peak fit analysis (to be described in the following) that indeed indicates that both RTA-treated samples need to be described with (at least) two different Ga species (labeled I' and II), while the bare n-GaN reference can be well described with a single species (labeled I). For species I and I', we chose a Voigt line shape to describe Ga in compound semiconductor environments (GaN and Ga_2O_3, respectively). For feature II, we chose a Doniach-Šunjić (DS) line shape to describe Ga in a metallic environment. This choice of line shape and the assignment of species I, I', and II was motivated by the respective observed binding energies, the XAES spectra, and the modified Auger parameters (to be discussed below). We find that the overall quality of the fit improves by selecting the DS line shape for species II (compared to a Voigt). The fits on all three samples employed a linear background and were performed simultaneously by coupling the full width at half maximum (FWHM; Gaussian and Lorentzian for the Voigt line shape and overall FWHM for the DS line shape) and asymmetry factor (DS). The results of the fits are shown in Fig 4.2a as solid lines. The
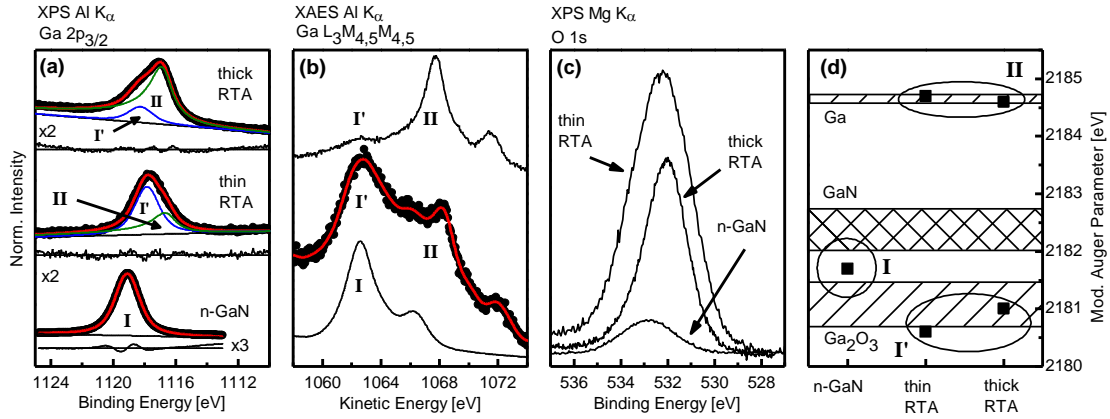
Fig. 4.2: Bare and RTA-treated thin and thick contacts on n-GaN: (a) Ga $2p_{3/2}$ XPS spectra (dots) with respective fits (solid) and residuals, (b) Ga $L_3M_{4,5}M_{4,5}$ XAES spectra [for the thin RTA contact sample the experimental data (dots) and a smoothed (solid red) line are shown], (c) O 1s XPS spectra, and (d) the corresponding modified Ga Auger parameters. In (d), hatched areas denote previously published values of Ga, GaN, and Ga_2O_3 (Ref. 51-54).

contribution of species II is dominant at the thick RTA sample surface, while the thin RTA sample surface is dominated by species I'. Both species (I' and II) in the Ga $2p_{3/2}$ spectra of the RTA-treated samples show an energy shift compared to species I in the n-GaN spectrum. This energetic shift can be explained by a change in the Ga chemical environment (from GaN to Ga_2O_3) after contact formation, as will be discussed below. Also, an interface-induced band bending due to the formation of a metal/semiconductor interface could be present.

The XAES Ga $L_3M_{4,5}M_{4,5}$ spectra are shown in Fig. 4.2b. The spectrum of the bare n-GaN shows only one contribution to the Ga $L_3M_{4,5}M_{4,5}$ transition (I), while the XAES spectra of both RTA-treated samples show (at least) two different contributions (species I' and II). As in the case of XPS, the thick RTA-treated sample has a dominant contribution at higher kinetic energies (II), though a small contribution at lower kinetic

energies (I') is observed. In contrast, the spectrum of the thin RTA-treated sample is a superposition of two species (I' and II), dominated by species I'.

To identify the two Ga species present, the modified Auger parameter (α') was computed (using the sum of the Ga $2p_{3/2}$ and Ga $L_3M_{4,5}M_{4,5}$ lines). α' is independent of the Fermi level position (*i.e.*, independent of band bending and charging). Our α' values are plotted and compared to previously published results for Ga-containing compounds [51-54] in Fig. 4.2d. For the bare n-GaN, we find α'= 2181.5 ± 0.1 eV. This lies between the previously reported values of GaN and Ga_2O_3. The O 1s XPS signal of all three samples is shown in Fig. 4.2c. We note that the signal for the bare n-GaN is relatively small when compared to the RTA-treated samples. Thus, we interpret the observed α' of n-GaN (species I) to be indicative of a GaN surface, possibly modified by some adsorbed water and/or OH formation at the surface from the above-mentioned chemical treatment.

For the two RTA-treated samples, a pair of α' values can be derived (*i.e.*, for species I' and II). For the thin RTA sample, we find α' values of 2180.6 ± 0.1 eV and 2184.7 ± 0.1 eV for species I' and II, respectively. For the thick RTA sample, we find α' values of 2181.0 ± 0.1 eV and 2184.6 ± 0.1 eV for species I' and II, respectively. While species I' agrees well with previously published values for Ga_2O_3, species II agrees well with metallic Ga [51-54], as shown in Fig. 4.2d. The assignment of species I' to an oxide species is supported by the XPS O 1s signal increase for the RTA-treated samples (Fig. 4.2c). Besides the line shape analysis (as discussed earlier), our interpretation of species II as metallic Ga is further supported by Ref. 50, which reported that Ga is released from GaN when Al/n-GaN is annealed.

To investigate the potential formation of VN at the interface, XES was used to resolve the chemical environment of nitrogen and vanadium atoms at the buried interface between the V-based contacts and n-GaN. In Fig. 4.3a, the N K XES spectra of the thick contact on n-GaN before and after RTA treatment are shown, along with reference materials (n-GaN and VN powder). The N K XES spectrum of the untreated contact sample is similar to that of bare n-GaN, as expected. Note the large magnification factor for the spectrum of the untreated contact sample (×470), which is due to the fact that the n-GaN is buried under V/Al/V/Au layers with a total nominal thickness of 215 nm. In the
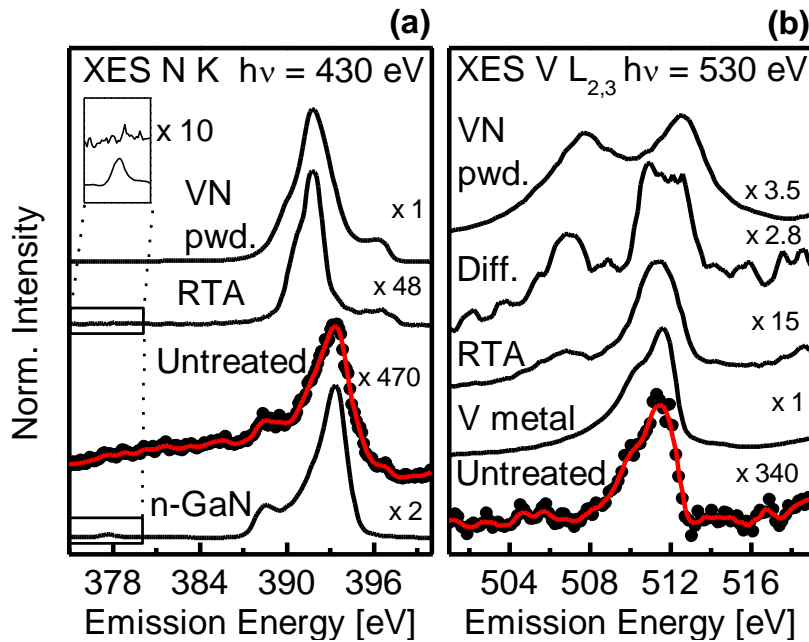
Fig. 4.3: (a) XES N K and (b) V $L_{2,3}$ spectra of n-GaN, thick contact sample before ("Untreated") and after RTA, and VN powder as well as a V metal reference. The XES V $L_{2,3}$ spectrum labeled "Diff." is the difference between the "RTA" spectrum and the "Untreated" spectrum (the latter multiplied by 0.6). For all spectra, multiplication factors are given that normalize the maximum count rate of all spectra to the same value. For the "Untreated" sample, the experimental data (dots) and a smoothed (solid red) line are shown. The inset in (a) shows the magnified region of the Ga 3d → N1s transition for the RTA-treated and n-GaN samples.

spectrum of bare n-GaN (Fig. 4.3a, bottom), a weak emission feature at ~377 eV can be observed, which stems from Ga 3d valence electrons relaxing into N 1s core holes (see enlarged inset in Fig. 4.3a. This feature indicates the presence of N-Ga bonds [55] (note that for the untreated contact sample, it is weaker than the noise level of the spectrum). In contrast to the untreated sample being similar to the n-GaN sample, the thick RTA sample is predominantly in a VN chemical environment. The feature indicative of N-Ga bonds (inset, Fig. 4.3a) and the prominent GaN shoulder at about 388.5 eV are absent in the thick RTA sample. A detailed noise-level analysis suggests that, for the thick RTA sample, the fraction of N atoms in a GaN environment (within the probing volume) is less than 20%. Thus, we find direct evidence for the formation of VN at the contact/GaN interface.

The RTA-induced formation of VN at the interface is also supported by the V $L_{2,3}$ XES spectra in Fig. 4.3b. The untreated sample displays a similar spectral shape to that of a V metal foil. The thick RTA sample shows an additional feature between 504 and 508 eV similar to the VN powder (Fig. 4.3b, top). To ascertain whether the spectrum of the thick RTA sample contains a VN contribution, the spectrum of the untreated sample (weighted by a factor of 0.6) was subtracted from the RTA-treated sample spectrum (Fig. 4.3b, 2nd from top). The difference spectrum shows two emission features which are similar to that of VN. Thus, we find that the V in the thick RTA sample exists in two forms: "unconverted" as metallic V and "reacted" as VN. Note that we do not find any evidence for a significant vanadium oxide formation.

The weight factor used to compute the difference spectrum allows us to quantify the fraction of V atoms in a VN environment. We find that 60% of the spectral

contribution is from metallic V (as in the untreated sample) and 40% from V in VN. This is corroborated by the contact scheme thicknesses: assuming that the lower V layer (15 nm) is entirely converted into VN, while the upper V layer (20 nm) entirely remains metallic, the fraction of V in a VN environment is 43% (ignoring attenuation length effects).

Our observation of a GaN to VN transformation is also thermodynamically supported since the heat of formation of VN (ΔH_{298} = -217.3 kJ/mol) is favored over that of GaN (ΔH_{298} = -109.7 kJ/mol) [56]. The presence of metallic V is likely due to characteristics of the contact scheme: while the upper V layer remains metallic, the lower V layer at the V-GaN interface undergoes VN formation. Consequently, the metallic Ga signal in XPS and XAES is greater for the thick RTA sample than for the thin RTA sample (see Fig. 4.2a and 4.2b) since it has more V atoms available at the interface to form VN and hence able to "release" Ga.

4.3.2 Microscopy and PEEM Results

AFM images of Au/V/Al/V/n-GaN samples before and after RTA treatment are shown in Fig. 4.4. The untreated sample (Fig. 4.4a) exhibits a flat surface with grains of about 0.25 μm diameter, and several surface particles with a maximal height of 40 nm. After RTA treatment, the surface morphology is drastically changed (Fig. 4.4b; note that the length scale differs from Fig. 4.4a), exhibiting three distinct features: "dendrites" consisting of "branches" (bright regions), "voids" (*i.e.*, the spaces between the branches), and "cracks" located in the voids (dark regions). The branches of typical dendrites are about 5 μm wide and approx. 150 nm high, while most cracks reach (at least) 100 nm below the void surface and are up to 2 μm wide.
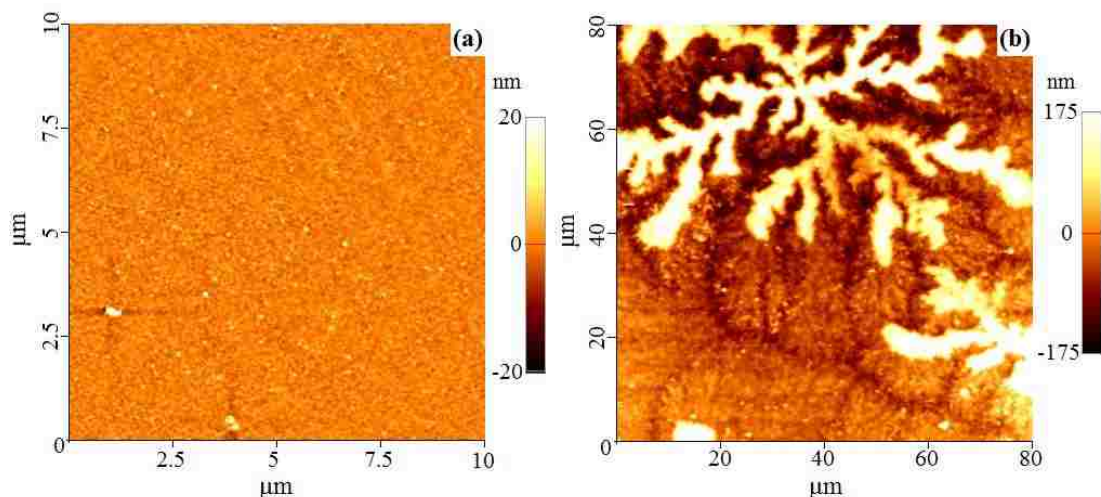
Fig. 4.4: AFM images of (a) an untreated (10 x 10 μm^2), and (b) a RTA-treated (80 x 80 μm^2) sample.

Element-specific WDS maps are shown in Fig. 4.5, and show the distribution of Au, Al, V, and Ga on the RTA-treated sample. For Au (Fig. 4.5a), we find a high concentration in the dendrites, a low concentration in the voids, and even less in the cracks. The Al distribution (Fig. 4.5b) also shows a high concentration in the dendrites, but the weaker contrast between dendrites and voids suggests a higher Al concentration in the void regions compared to the Au distribution. As in the case of Au, the cracks show a significantly lower concentration of Al as well. Note that our X-ray photoelectron spectroscopy (XPS) analysis of these samples (not shown) reveals broadened Au 4f core levels after RTA, which might be indicative of a Au-containing alloy formation, and shows Al 2p peak positions and shapes that suggest a broad oxidized state at the probed surfaces (henceforth denoted "Al-O").
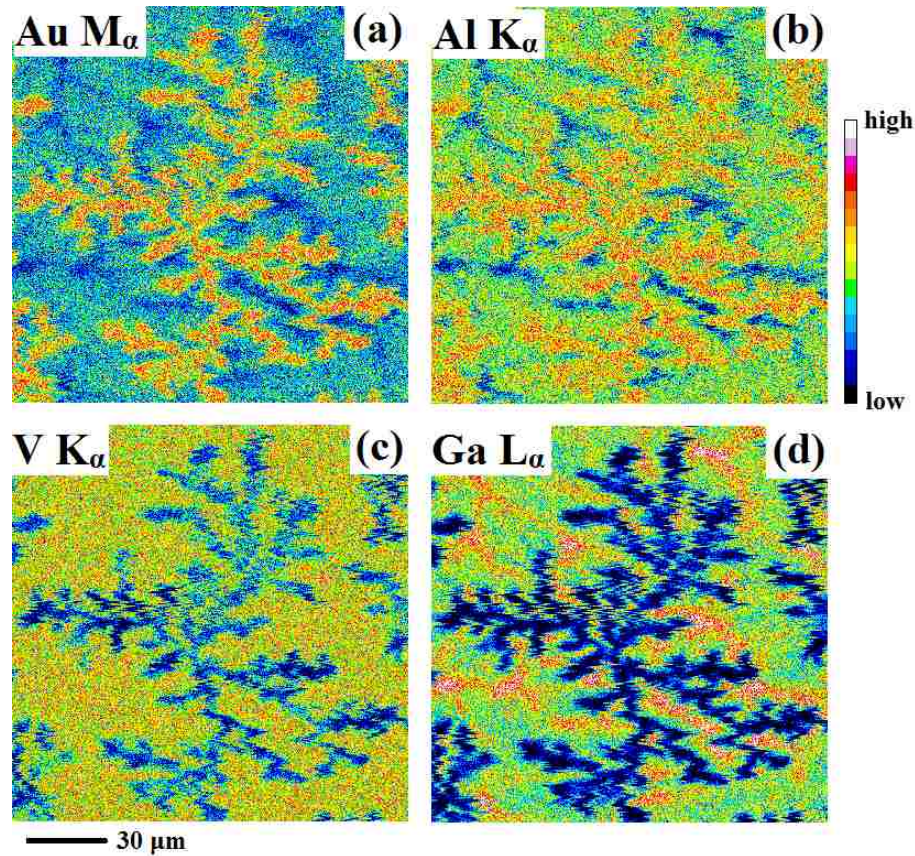
Fig. 4.5: Elemental WDS maps (150×150 μm^2) of the RTA-treated contact stack/GaN sample: (a) Au, (b) Al, (c) V, and (d) Ga.

In contrast, the distribution of V and Ga (Figs. 4.5c and 4.5d, respectively) show a very low concentration (if any) in the dendrites. The V distribution appears homogeneous in the voids and cracks, while the Ga signal is strongest in the crack regions and intermediate in the void regions (note our earlier laterally integrating findings of Ga in two chemical environments, namely as GaN and metallic Ga (section 4.3.1).

Thus, we find that the dendrites are mostly composed of Au and Al-O, while the voids contain (in order of certainty) V, Ga, Al-O, Au, and (based on the XPS results) presumably N. The cracks contain V, Ga, and presumably N, and are thus interpreted to

consist of a (V, Ga, N) layer that covers the n-GaN substrate. This layer differs from the void layer because it does not appear to include Al and/or Au, but exhibits a similar concentration of V. It is also sufficiently thick to completely attenuate the GaN-related N 1s XES signal (section 4.3.1).

The presence of V in the voids and in the (V, Ga, N) layer is in agreement with the initial (pre-RTA) contact scheme (with a V layer adjacent to the n-GaN substrate) and the finding of VN formation (via a V-Ga exchange that forms metallic Ga) at the V-GaN interface; furthermore, some metallic V remains unreacted (section 4.3.1).

To corroborate our findings with a more surface-sensitive, yet laterally resolved spectroscopy, we have used UV- and X-ray excited PEEM to study the RTA-treated surface. In Fig. 4.6a and 4.6b, UV-excited PEEM images with a 70 (a) and 20 (b) μm field of view (FOV) provide contrast resulting from local variations of the work function and topography. The images again display the dendritic structure seen in the AFM and WDS images [note that the PEEM images were recorded on a different dendrite and that the location of Figs. 4.6(b – e) is indicated by a circle in Fig. 4.6a].

The spatially-resolved chemical structure of the surface of the RTA-treated samples surface was investigated by PEEM contrast images of PES lines. PES V $2p_{3/2}$, Al 2p, and Au $4f_{7/2}$ PEEM images from the same area as Fig. 4.6b are shown in Figs. 4.6c, 4.6d, 4.6e, respectively. Elemental contrast images were obtained by subtracting a "background" image (at approx. 3 - 5 eV lower binding energies) from the "peak" image (*i.e*., taken at the binding energy of the core level of interest) and then dividing by the background image, which thus takes local intensity variations of the background into account. The excitation energies (197 eV for Al 2p, 300 eV for Au $4f_{7/2}$, and 635 eV for
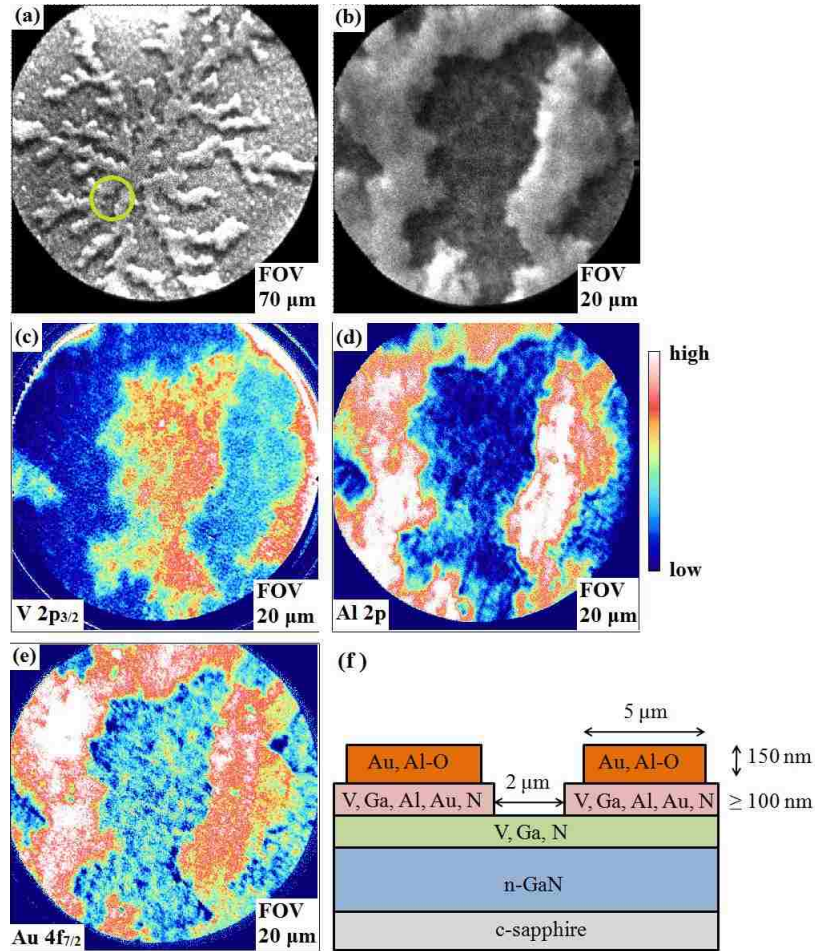
Fig. 4.6: PEEM images of the RTA-treated contact stack/GaN sample excited (a - b) by a Hg-lamp, and (c - e) by soft X-rays. The diameter of the field of view (FOV) is 70 μm in (a) and 20 μm in (b)–(e), and the circle in (a) indicates the location of images (b)-(e). PEEM images were obtained using V $2p_{3/2}$, Al 2p, and Au $4f_{7/2}$ photoemission lines for (c), (d), and (e), respectively. The scheme in (f) depicts a model that is consistent with the findings and gives typical dimensions (not to scale) for dendrites and cracks.

V $2p_{3/2}$) for each PEEM image were chosen such that the kinetic energies of the detected photoelectrons were similar (ranging from 120 to 220 eV), resulting in roughly the same 1/e attenuation length of the photoelectrons (6.4 ± 1.5 Å for Au $4f_{7/2}$ and 4.9 ± 0.9 Å for Al 2p and V $2p_{3/2}$ [57] for an estimated average void composition of V:Ga:Al:Au of 1 : 0.8 : 0.6 : 0.4) and thus in roughly comparable information depths. Furthermore, the

photon energies were selected in order to enhance the photoionization cross section [58] within these constraints.

The V $2p_{3/2}$ PEEM image in Fig. 4.6c shows that the surface of the voids is V-rich, while the surface of the dendrites is V-poor (or V-free). The Al $2p$ and Au $4f_{7/2}$ images (Fig. 4.6d and 4.6e, respectively) show that there is more Al and Au on the dendrite surfaces than on the surface of the voids. Thus, we find that the V distribution is also anti-correlated to the Al and Au distribution *on the surface* of the various regions. Thus, we find that the elemental and chemical distribution observed with WDS (*i.e.*, with a more bulk-sensitive probe) is completely corroborated by the surface-sensitive PEEM images. This suggests the absence of surface segregation effects and a certain degree of homogeneity within the dendrites and voids.

By combining our laterally-resolved AFM, WDS, and PEEM results with our previous and other unpublished laterally-integrating spectroscopic results (XPS, XES, and XAES [section 4.3.1]), we are able to propose a detailed picture of the contact formation on n-GaN, as shown in Fig. 4.6f. In establishing this picture, we started with interpreting the WDS images, assuming that "green" constitutes the lower limit for the presence of a particular element, and then refining the model by comparing with all other results. In the resulting model in Fig. 4.6f, elements in the various contact layers are thus listed in order of certainty. We find a three-layer structure of dendrites, voids, and cracks. The dendrites are composed of Au and Al-O, suggesting a significant interdiffusion of V and Al during the RTA treatment. The voids contain V, Ga, Al, and Au, and possibly also N. The cracks, as seen in AFM and WDS (we speculate that the cracks are not visible in the PEEM images due to the very grazing incidence illumination of 16°), extend through

42

the "void layer" and expose the underlying (V,Ga,N) layer on the n-GaN substrate. Based on our data, it is not possible to extract definite evidence that this layer completely covers the n-GaN substrate also underneath the "dendrite and void layers", but this structure appears feasible given the observed formation of VN and metallic Ga in the laterally integrating spectroscopies (section 4.3.1). Macroscopic contacts would now most likely form at the dendrite surface. The current would flow through the Au/Al-O layer and the "void layer", as well as the previously suggested (low-work function) VN in the (V,Ga,N) layer. The latter forms a direct (and possibly graded) contact to the n-GaN substrate, and is thus expected to play the primary role in establishing an Ohmic contact.

4.4 Summary

In conclusion, we have investigated the interface formation between V/Al/V/Au contacts and n-GaN. Our findings clearly show VN formation as a result of RTA treatment of V-based contacts on n-GaN. The presence of metallic Ga indicates that GaN serves as the nitrogen source for the observed VN formation. We have also studied the surface morphology as a result of the contact formation onto GaN using AFM, WDS, and PEEM. As a result of the RTA treatment, the surface is composed of dendrites which are composed of Au, Al, and V. We find that there is relatively more Au and Al in the dendrites as opposed to the voids, while V is more abundant in the voids. Through the use of PEEM, we find that the distribution of V is anti-correlated to that of Au and Al. These findings provide detailed insight into the contact formation of GaN-based devices and the improved performance of V-based contacts.

CHAPTER 5

CONTACT FORMATION ONTO n-AlN

5.1 Introduction

N-type $Al_xGa_{1-x}N$ alloys are of high interest due to their applications in optoelectronic

devices, such as light emitting diodes [2, 3], lasers [59], and photodiodes [60]. In such

devices, forming Ohmic contacts is of large importance. However, this is a significant

fundamental challenge for these materials. First, the electron affinity (χ) of GaN ($\chi = 3.3$

[61] or 4.1 [62]) and AlN ($\chi = 1.9$ [61] or less than zero [63]) are not conclusively known

(but most likely very different), and the band gaps (E_g) of GaN (3.34 eV) and AlN (6.02

eV) [64] are very different as well, and thus it is difficult to find *one* contact scheme

compatible for the entire $Al_xGa_{1-x}N$ ($0 \leq x \leq 1$) alloy system. For these highly ionic

semiconductors, the Fermi level of the metal does not appear to be pinned by

surface/interface states of the semiconductor. Consequently, to form Ohmic contacts to

AlN (and a variety of other semiconductors, such as n-ZnO or n-SrTiO3), one needs to

employ a metal with a very small work function [45], *e.g*., VN. Vanadium-based contacts

involving rapid thermal annealing (RTA) were first used on n-$Al_{0.3}Ga_{0.7}N$, [9] and it was

found that Ohmic contact formation occurred at less severe conditions (*i.e.*, lower

processing temperatures) and similar properties when compared to the traditional Ti-

based contacts used for n-$Al_xGa_{1-x}N$ [9, 10]. However, it was also found that, with

increasing Al content in the alloy, the RTA temperature had to be increased for optimal

specific contact resistivity [10]. Second, the employed contact schemes are very complex

and empirically derived. Consequently, a deeper understanding of the underlying

interface formation processes and insights into the character of interface species and

secondary phases is lacking. Such understanding, however, is needed to further optimize the interfaces and thus performance of associated devices. While the motivation of this study is an applied one, the main goal of this work is to gain a fundamental understanding of the chemical interface processes during high-temperature annealing of such complex semiconductor-metal interfaces.

For a deeper insight into the interface properties, we have employed a unique combination of spectroscopic and microscopic tools. In particular, we have used x-ray photoelectron spectroscopy (XPS) and x-ray emission spectroscopy (XES) to study the local chemical environment at the surface and near-surface bulk in an atom-specific fashion. These techniques have previously been used successfully to shed first light on the V-based contact formation on n-GaN (see Chapter 4). XES has also been widely used to investigate the electronic structure of GaN, AlN, and their alloys [55, 65, 66]. Here, XES was used to investigate the local atomic environment of nitrogen and vanadium of Au/V/Al/V/n-AlN structures before and after RTA treatment. Since XES is a photon-in-photon-out technique, it can probe the surface-near bulk and buried interfaces within the top tens to a few hundreds of nanometers. In addition, the surface composition before and after annealing was monitored by XPS. Furthermore, we have employed atomic force microscopy (AFM) in air to study the surface morphology before and after interface formation, and wavelength-dispersive x-ray spectroscopy (WDS) to investigate the lateral distribution (in the form of maps) of atomic species at the surface.

By combining the results from these complementary experimental approaches, we are able to depict a detailed model of the interface structure. As will be shown in Section

5.3.2, this structure is very complex and indeed requires the combination of such fundamental and sophisticated techniques to gain a comprehensive picture.

5.2 Experimental Details

Si-doped AlN samples were grown by molecular beam epitaxy onto c-plane sapphire. Subsequently, metal layers were deposited by electron beam evaporation. Additional details of sample growth and preparation have been published elsewhere [10]. The Au/V/Al/V contact scheme (where Au is the topmost layer) consisted of Au(100 nm)/V(20 nm)/Al(80 nm)/V(15 nm) (all thicknesses given are nominal values). Samples were cut into two parts, one of which was RTA-treated (1000 °C for 30 seconds in N_2). The samples were then packed and sealed under dry nitrogen without air exposure (to minimize any external surface contamination) and shipped from Boston University to UNLV. Samples were unloaded without air exposure in an N_2-purged glovebox prior to direct transfer into the ultra-high vacuum (UHV) chamber for XPS analysis. For the less surface-sensitive XES experiments, samples were briefly (< 10 minutes) exposed to air prior to transfer into the UHV chamber at the ALS. AFM experiments were conducted in air after completion of the XPS and XES experiments, and WDS was performed subsequently. Reference materials (VN powder, metal foils) were obtained from Alfa Aesar.

XES experiments were performed at Beamline 8.0.1 at the Advanced Light Source (ALS), Lawrence Berkeley National Laboratory, in our SALSA (Solid And Liquid Spectroscopic Analysis) endstation [37]. SALSA is equipped with a high-resolution, high-transmission variable line spacing soft x-ray spectrometer (further details

can be found elsewhere [38]). XPS experiments were performed at UNLV using a Mg K_α

radiation x-ray source and a SPECS PHOIBOS 150MCD electron analyzer. The energy

scale of the analyzer was calibrated using XPS and Auger lines of Au, Ag, and Cu [25].

AFM measurements were performed with a Park XE70 instrument in contact mode.

Elemental WDS and backscattered electron (BSE) mapping was performed at the UNLV

Electron Microanalysis and Imaging Laboratory with a JEOL JXA-8900 electron probe

microanalyzer. The Au M_α, V K_α, and Al K_α fluorescence lines were detected

simultaneously with three wavelength-dispersive spectrometers using lithium fluoride

(for Au M_α and V K_α) and thallium acid phthalate (TAP, for Al K_α) analyzing crystals, an

acceleration voltage of 20 kV at a beam current of 100 nA, and dwell time of 15

millisecond per pixel.

5.3 Results and Discussion

5.3.1 Spectroscopic Results

In Fig. 5.1, N K XES spectra of an untreated and an RTA-treated sample are shown,

along with n-AlN (epilayer) and VN (powder) reference spectra. The spectrum of the

untreated sample was multiplied by 8000 to account for the significant x-ray attenuation

in the metallic overlayers - the attenuation length (*i.e.*, the film thickness that attenuates

an x-ray beam to 1/e of its initial intensity) at 392 eV is 35 nm in Au, 323 nm in V, and

273 nm in Al [34]. This demonstrates the unique capability of XES to probe a buried

system, even through a metal layer stack of a nominal thickness of 215 nm. The intensity

of the N K XES spectrum after annealing is substantially increased due to morphological

changes described below.
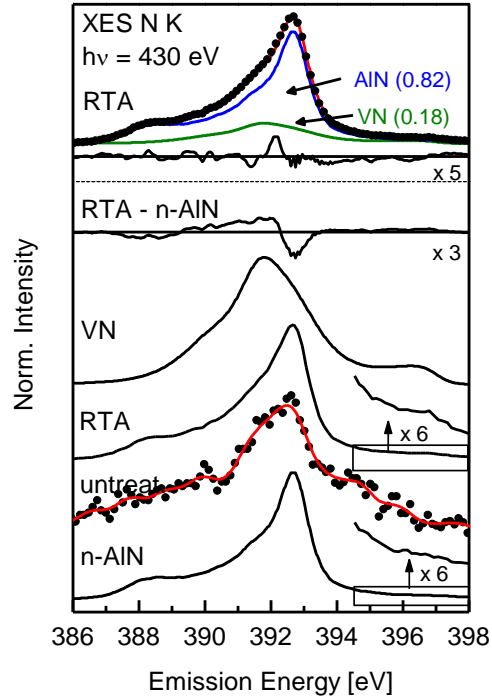
Fig. 5.1: N K XES spectra of the untreated (data points and Fourier-smoothed curve) and RTA-treated (data only) sample, together with n-AlN and VN reference spectra. Above the VN spectrum, the difference (magnified) between the RTA-treated and the n-AlN spectrum (normalized to area) is shown. For the n-AlN and the RTA spectrum, an enlarged (× 6) view of the uppermost valence band region is also shown. The top portion of the graph shows a fit (solid red line) of the RTA-treated sample data (dots) using a sum of the n-AlN (blue, 82% area fraction) and VN (green, 18% area fraction) spectra. The residual of the fit, magnified by a factor of 5, is also shown.

The energies of the main peak of the N K spectrum of both, the untreated and the RTA-treated sample, agree well with that of n-AlN. In fact, at first glance, the emission of the RTA-treated sample looks nearly identical to that of n-AlN, but closer inspection reveals a slight shoulder at ~391 eV, best seen in the difference spectrum (RTA − n-AlN, magnified by 3) shown above the VN reference spectrum. This feature coincides with the main peak seen in the VN spectrum. To quantify the contributions from AlN and VN to

the N XES spectrum, the spectrum of the RTA-treated sample is compared to a sum spectrum that was computed using the spectra of the n-AlN and VN references. This sum spectrum is also shown in Fig. 5.1 (top, red solid line), along with the measured data, the AlN and VN contributions, the residual (*i.e.*, the difference between the data and the fit), and the utilized weight factors (which were determined with a least-square fit routine to minimize the residual). The result shows that 81 ± 1 % of the peak area can be described with the n-AlN spectrum, and the rest ($19 \pm 1\%$) with the VN spectrum. Note that we do not attempt to interpret the lineshape of the (very weak) peak of the untreated sample, since it is most likely obscured by background effects that can be neglected for all other (significantly more intense) peaks.

An additional indicator for the presence of VN in the RTA-treated sample is the observation of a 'knee' at higher energies (~396-397 eV, see amplified region above the RTA spectrum). This feature is also present in VN, but not in AlN, as can be seen from the amplified region shown above the n-AlN spectrum in Fig. 5.1. The feature is ascribed to valence electrons at and near the Fermi energy and their relaxation into the N 1s core hole (note that VN is considered to exhibit metallic character [67-70]. Thus, we conclude that the nitrogen atoms probed in the RTA-treated sample are present as AlN and partially transformed to VN as a result of the RTA treatment.

V L_3 XES suggests the formation of VN in the RTA-treated sample as well. The V L_3 spectra of the samples are shown in Fig. 5.2, along with a V metal, (modified) VN, and a VO_2 reference spectrum. For the VN reference (referred to as "VN mod."), we modified the spectrum of the as-received VN powder (Alfa Aesar) to account for the observed surface oxidation by subtracting a suitably weighted V L_3 spectrum of a VO_2

reference. The presence of VO_2 oxidation would add artificial spectral weight to the valley in VN (at approximately 510 eV). The weight was chosen based on the integrated area ratio for the O K emission in the VO_2 and the oxidized VN spectra (not shown) to approximate a "pure" VN spectrum.

The untreated sample has a V L_3 emission energy and broad shape similar to that of vanadium metal (as expected). The spectrum has a very low signal-to-noise ratio, since the V emission stems from atoms below at least (nominally) 100 nm of Au (the 1/e attenuation length at 510 eV in Au is about 43 nm [34]. Upon RTA treatment, the
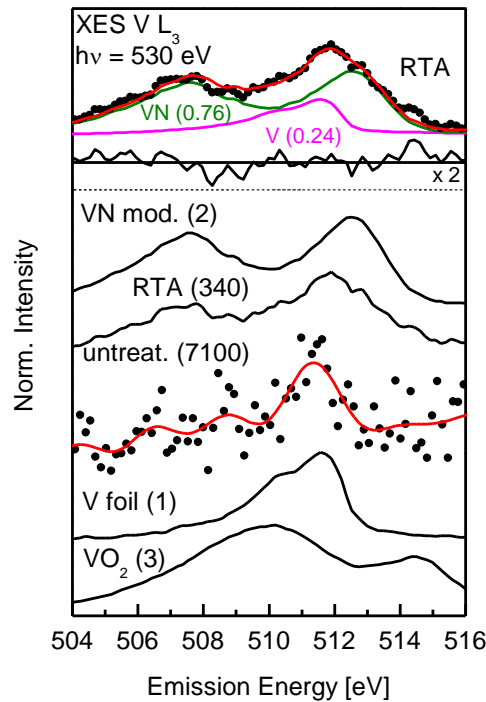
Fig. 5.2: V L_3 XES spectra of the untreated (data points and Fourier-smoothed curve) and RTA-treated (data only) sample, together with V metal, VN, and VO_2 reference spectra. The VN spectrum is designated as modified ("mod."), because a vanadium oxide contribution was removed (for details see text). The top portion of the graph shows a fit (solid red line) of the RTA-treated sample data (dots) using a sum of the V metal (magenta, 24% area fraction) and the modified VN (green, 76% area fraction) spectra. The residual of the fit is also shown, multiplied by 2.

spectrum undergoes pronounced changes, most notably a substantial increase in intensity and an additional emission feature at lower energies. To understand the origin of this feature, a sum spectrum was computed using the VN (mod.) and V metal reference spectra and suitable weight factors to describe the RTA data (shown in Fig. 5.2, top portion). The weight factors were again determined with a fit, and it was found that the RTA spectrum can be best described with 76 % (± 5 %) of the area from a VN (mod.) contribution, and 24 % (± 5 %) from V metal. Thus, most of the probed V atoms exist in a VN environment, while some remain unreacted in a V metal environment. Note that we do not find any direct indication of the presence of vanadium oxide, but small amounts might nevertheless be present (since there is some uncertainty in the "purity" of the VN mod. reference spectrum, as discussed above).

To summarize the XES results, we find the formation of VN as a result of the RTA treatment, and also detect the presence of metallic V and of AlN in the probed volume.

In order to complement these findings with very surface-sensitive information, the surface composition before and after RTA treatment was analyzed using XPS. Fig. 5.3 shows the corresponding XPS survey spectra. As expected, the untreated sample surface is dominated by Au lines (*i.e.*, from the topmost layer in the metal layer structure). Upon RTA treatment, the Au signals are significantly reduced, and previously buried elements (Al, V, and N) are now detected on the surface. This finding suggests significant interdiffusion processes and/or morphological changes as a result of the RTA-treatment, which will be further discussed in the following paragraphs. We also note that, despite the efforts to minimize surface contamination (as described in the experimental section),
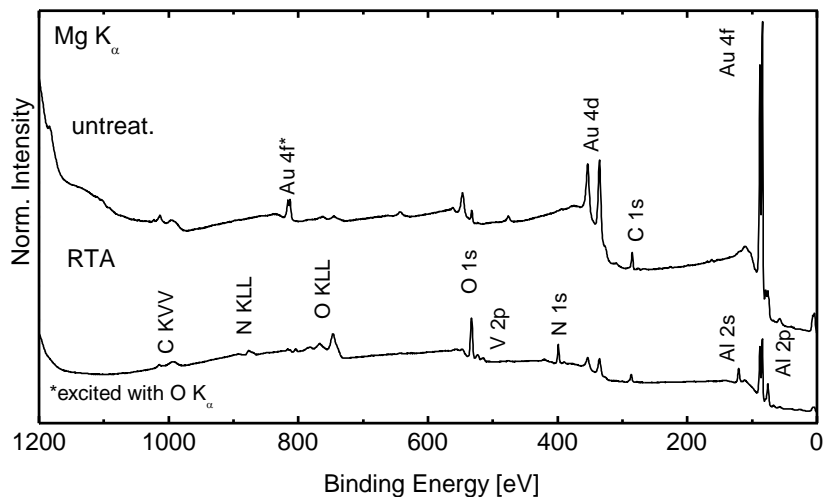
Fig. 5.3: XPS survey spectra of the untreated and RTA-treated sample, and (b) detail spectra of the Al 2p region of the RTA-treated sample and an oxidized Al metal foil.

both samples exhibit signals from C and O species on the surface. While the carbon signal is reduced after annealing, the oxygen signal is significantly enhanced, as evidenced by the increase of both the O 1s photoemission line as well as the O KLL Auger emission. Apparently, an oxide species has formed on the surface during the annealing step. In order to shed light on the chemical nature of the surface oxide, detail spectra were recorded for all metal lines observed in the survey spectra.

In Fig. 5.4, the Al 2p region is shown for the annealed sample and an oxidized Al metal foil reference (the Al foil was scratched in a N_2 filled glove box prior to transfer into UHV to also expose some metallic Al atoms at the surface). Note that the Al 2p feature was not detected in the untreated sample because of attenuation in the Au top layer.

Due to the Mg $K_{\alpha 3,4}$ excitation satellites of the (non-monochromatized) x-ray source, the as-measured spectrum of the annealed sample has satellite contributions from
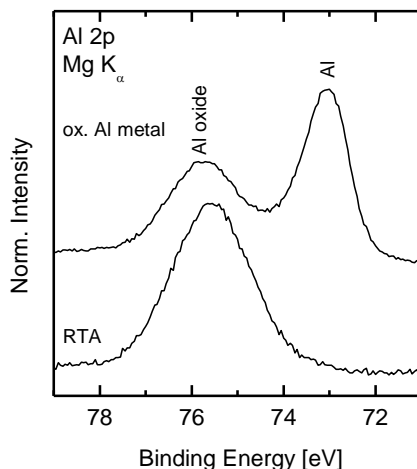
Fig. 5.4: XPS detail spectra of the Al 2p region of the RTA-treated sample and an oxidized Al metal foil.

the Au 4f lines in the Al 2p spectral window. To subtract these satellite lines, a sputter-cleaned Au reference foil was measured in the same energy window, and the spectrum was subtracted from the spectrum of the RTA-treated sample (after normalizing both spectra to the Au $4f_{7/2}$ main peak height). The result of this subtraction is shown in Fig. 5.4.

The oxidized Al metal reference foil has two components contributing to the Al 2p region - the feature at lower binding energies is due to metallic Al, while the one at higher binding energies is a native aluminum oxide, most likely Al_2O_3 (as it is thermodynamically most stable). The energetic positions of the two features are in agreement with the chemical shift reported between metallic Al and Al_2O_3 (+2.7 eV [30, 71, 72] or +2.8 eV [30]. Note that the spin-orbit splitting between the $2p_{1/2}$ and $2p_{3/2}$ lines (0.4 eV [73]) cannot be resolved in our measurements, since it is small compared to the

experimental linewidth (dominated by the width of the excitation source) and likely further obscured by the presence of Al in (slightly) differing oxidation states.

As is apparent from the excellent agreement between the binding energy of the Al 2p peak of the annealed sample and the aluminum oxide peak of the Al reference foil, we find that the Al atoms at the surface are not metallic, but exclusively in oxide form. This explains the significant increase in O 1s intensity; however, we note that, additionally, other oxides may exist. In particular, we cannot completely rule out the presence of some vanadium oxide – the peak position and lineshape analysis of the V 2p photoemission and V LMM Auger lines is inconclusive, most likely due to the presence of both a VN and a metallic V species (in addition to a potential vanadium oxide).

To summarize the XPS findings, we note a significant change in surface composition after annealing, corroborating the XES-derived interpretation of significant interdiffusion processes and/or morphological changes as a result of the RTA-treatment. We find a substantial reduction in the Au surface intensity, an increase of the V, Al, N, and O signals, and the clear presence of an aluminum oxide on the surface.

5.3.2 Laterally-resolved Results

To supplement the compositional and chemical information derived from the spectroscopic data, we have collected contact-mode AFM images (Figs. 5.5a and 5.5b), a BSE image (Fig. 5.5c), and WDS elemental maps of Al, Au, V (Figs. 5.5d-f) to derive the surface morphology and lateral elemental distribution. The AFM images of the untreated sample (Fig. 5.5a) exhibit a very flat surface (maximum elevation about 10 nm), covered with closely packed grains (with typical diameter of 100 nm), as expected for a thick metal overlayer and in agreement with the XPS information. In contrast, the surface of
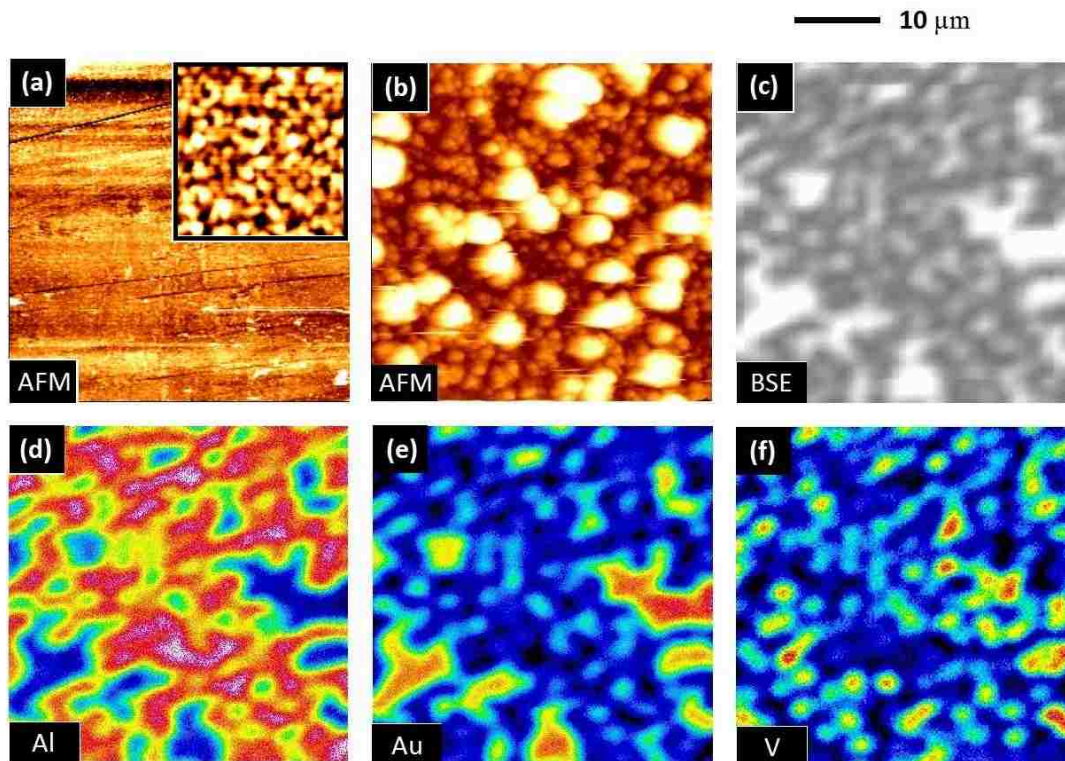
Fig. 5.5: 40 x 40 μm^2 images of the untreated sample, acquired by (a) AFM (contact mode in air; inset shows a 1 x 1 μm^2 image), images of the annealed sample acquired by (b) AFM, (c) using back-scattered electrons (BSE), and (d)-(f) WDS. Images (c) – (f) were collected from the same location on the sample, while (b) was taken at a different location. The maximal AFM z-scale (elevation) between the dark (low) and white (high) areas is about 10 nm for (a) and about 1.4 μm for (b). The WDS maps show the elemental distribution (fluorescence intensity) of (d) Al, (e) Au, and (f) V. The intensity scale follows the colors of the electromagnetic spectrum (black and blue: low; red and white: high).

the annealed sample in Fig. 5.5b is rough (maximum elevation about 1.4 μm), with an inhomogeneous lateral distribution of large clusters (approximately 7 μm in diameter) and small clusters (approximately 1-2 μm in diameter) in-between. In the vertical dimension, the large clusters are about 1.4 μm higher than the lowest (darkest) regions. For the small clusters, this height is about 270 nm from the lowest regions.

The BSE map in Fig. 5.5c shows a similar structure, albeit at a different location on the sample. At the "BSE location", the WDS maps show that the large clusters are mostly composed of Au (Fig. 5.5e), with some contribution of V (Fig. 5.5f; this is most easily seen for the three pronounced clusters in the bottom left corner or the three clusters at the bottom right edge of the maps). We note that the distribution of V is "spotty" – apparently, islands or subclusters containing V are formed. As is evident from the Al and Au maps (Fig. 5.5d and 5.5e), their distribution is anti-correlated – for example, the three clusters with high Au and (spotty) V intensity correspond to low intensities in the Al map. Note that the 1/e attenuation length of the Al K_α fluorescence used for this map is between 162 nm (in pure Au) and 480 nm (in pure V) [34]. Thus, this finding suggests the absence of Al in the large clusters, while it does not rule out the presence of Al atoms *underneath* the large clusters, *i.e.*, in the n-AlN substrate.

In combining the results from the various elemental, chemical, and topographic probes, we are now able to paint (propose) a comprehensive picture of the interface structure between the metal overlayers and the n-type AlN film after annealing. From the AFM images, we find that the contact layers transform from a nanocrystalline closed layer to a surface with two types of clusters ("large" and "small"). From the WDS elemental mapping, we find that the large clusters are mostly composed of Au with some inhomogeneous V enclosures or islands. From the XES analysis, we know that these V regions contain vanadium in both, a metallic and a VN-like environment. In contrast to the large clusters, the small clusters show a strong Al signal and minimal Au and V intensity. From the XPS analysis, we know that these Al atoms (at least those at the surface) are exclusively in an aluminum oxide environment. The (laterally integrated)

XPS intensity analysis shows that annealing leads to morphological changes that allow previously buried elements (N, Al, and V) to be detected at the surface, and, as mentioned, the AFM images and WDS maps can then be used to correlate this information with laterally-resolved insights, as described above.

The findings are summarized in the schematic structure shown in Fig. 5.6. During the annealing process, the atoms of the metallic top layers become very mobile and diffuse to form a very different surface morphology. Au and V atoms migrate to form large clusters (with the V being present in both metallic and VN form), while Al atoms migrate to form small clusters, presumably forming an aluminum oxide, and leading to an increased number of grain boundaries. The effective overall thickness of the "cover layer" is thus reduced, so that, *e.g.*, the AlN substrate becomes "visible" in XES. As mentioned, the XES analysis confirms the formation of VN as a result of the RTA treatment. For reasons discussed below, we speculate that the nitrogen source for this VN formation is likely the AlN layer, and that thus the VN is located at the interface between
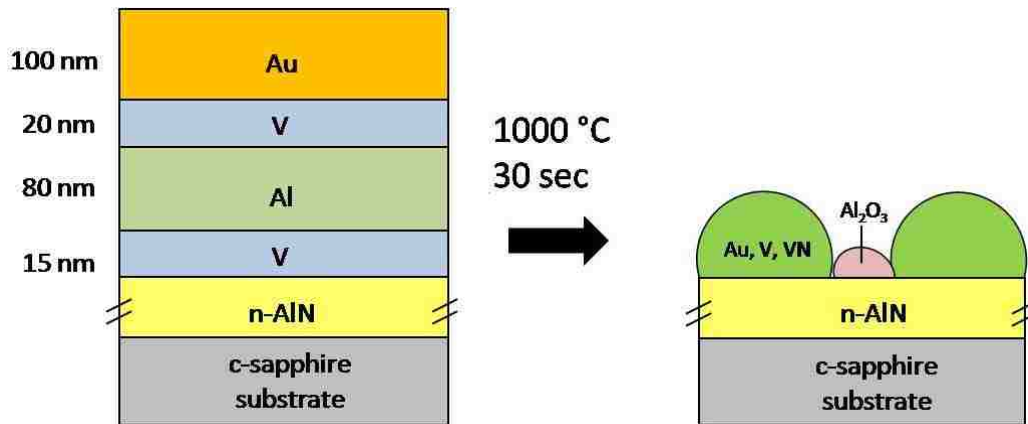
Fig. 5.6: Schematic of metal/n-AlN contact structure before and after rapid thermal annealing.

the large clusters and the AlN substrate. Also, note that the WDS maps show an inhomogeneous lateral V distribution within the large clusters (not shown in Fig. 5.6).

As mentioned, we propose that the nitrogen source for the VN formation is the AlN substrate (and not the ambient N_2 molecules during the RTA step). For n-GaN, we could previously show the presence of metallic Ga at the (Au, V, Al)/GaN interface, suggesting that the nitrogen source was indeed the GaN substrate (see Ch. 4). In the present case, a similar experimental argument cannot be applied, since the Al signal is vastly dominated by the Al atoms in the AlN substrate, and because Al is additionally present in the (initial) contact scheme. France *et al*. found that for optimal contact resistivity in the (Al,Ga)N alloy system, the required RTA processing temperature increases with increasing Al content – varying from 650°C (pure n-GaN) to 1000°C (pure n-AlN) and proposed that the formation of VN was directly involved with forming Ohmic contacts [10]. It was hypothesized that the RTA temperature was related to the bond strength (E_b) of Ga-N and Al-N [10]. Indeed, Talwar *et al*. report that $E_{b,AlN} > E_{b,GaN}$ [74]. If we assume that ambient N_2 molecules serve as the nitrogen source for VN formation, then the processing temperature should be independent of alloy composition since the V-N interaction is independent of the underlying substrate material (GaN or AlN). Furthermore, if the nitrogen originated from the ambient, then the fraction of VN detected in V $L_{2,3}$ XES should be constant when compared to the metallic V emission (for both GaN or AlN substrates since the contact schemes are identical). In contrast, we find (here and in Ch. 4) that the fraction of VN detected is not the same for the AlN and GaN systems. Since the optimal RTA processing temperature is reported to be dependent on the (Al,Ga)N composition, it is thus very unlikely that the ambient N_2 plays a significant

58

role as a nitrogen source. In contrast, this analysis suggests the n-(Al,Ga)N alloy as the nitrogen source for VN formation, as in the case of n-GaN.

These findings shed light on the fundamental interactions between metal contact layers and the n-(Al,Ga)N alloy system during annealing. The N K XES spectra of n-GaN show the nitrogen atoms in a dominant VN chemical environment, while for n-AlN, the N is dominant in an AlN environment with some VN contributions (note that the metal contact schemes in the two experiments were identical). For the n-GaN, the vanadium was mostly found in a metallic state, with some VN also being found (see Ch. 4), while in the case for n-AlN the converse is true. Furthermore, we find very different morphologies in the two cases – the n-GaN-based system forms a vein-like network after RTA treatment (see Ch. 4), while in the n-AlN case, we observe large and small clusters. This indicates that contact formation on the (Al,Ga)N alloy system occurs differently for varying Al content. A possible explanation could be based on thermodynamic stability. The standard heat of formation (ΔH_{298K}) for GaN, VN, and AlN is -109.7 kJ/mol, -217.3 kJ/mol, and -318.6 kJ/mol, respectively [56]. Since the heat of formation of VN is more negative than that of GaN, it is energetically more favorable to utilize a certain number of N atoms to form VN rather than GaN.

In contrast, the heat of formation of AlN is more negative than that of VN, and thus the formation of AlN is favored over that of VN in a situation where nitrogen is limited. Thus, these simple thermodynamic considerations can be one explanation for the dominant contribution of VN to the N K XES spectrum in the annealed n-GaN system. For the RTA-treated n-AlN system, the AlN contribution (from the substrate) dominates the nitrogen spectrum over VN, primarily due to the morphological changes discussed

above. Nevertheless, VN is formed in the annealing process of AlN as well, as can be seen in the V L_3 XES spectra, which show that VN is in fact the dominant V environment in the probed volume. In order to supply sufficient energy for this (nominally) endothermic process, thermal energy is required, and thus optimal (Ohmic) metal contacts on n-AlN presumably require higher RTA temperatures than in the n-GaN case in order to form a sufficient amount (*i.e.*, electronic pathway) of VN.

5.4 Summary

We have investigated the interaction between Au/V/Al/V metal contact layers and n-AlN upon annealing using a combination of spectroscopic and microscopy techniques (XES, XPS, WDS, BSE, and AFM). We have confirmed the previously speculated formation of VN as a result of the annealing step, and find significant morphological changes that lead to the formation of large and small clusters with significantly different elemental and chemical composition. Large clusters are composed of Au and an inhomogeneous distribution of V atoms in metallic and VN environments. Small clusters are composed of aluminum oxide. We have provided arguments that the nitrogen source for the VN formation is the AlN substrate and not the ambient nitrogen molecules during annealing. Finally, we have discussed the thermodynamical considerations governing the formation of GaN, VN, and AlN, and thus shed light on the metal contact interaction mechanism for the entire n-(Al,Ga)N alloy system.

CHAPTER 6

INTERFACE FORMATION AT Cu(In,Ga)Se$_2$ AND CdS

6.1 Introduction

Cu(In$_{1-x}$Ga$_x$)Se$_2$ (CIGSe)-based thin film solar cells have reached efficiencies of 20% at the laboratory scale [5] and 13.4 % for large area modules [75]. These high efficiencies are achieved with a CdS buffer layer between the window (n$^+$-ZnO/i-ZnO) and the chalcopyrite absorber, which is deposited in a chemical bath deposition (CBD) step. To achieve even higher efficiency, a better understanding of the junction formation between CdS and CIGSe absorber is needed. We have thus investigated the CdS/CIGSe interface as a function of CBD time (*i.e.*, CdS thickness) in order to investigate the growth start, to detect interfacial intermixing (as reported in [76], [77] and references therein), and to monitor the chemical structure of the interface using chemically and surface-sensitive techniques. X-ray emission spectroscopy (XES) and X-ray photoelectron spectroscopy (XPS) have previously been used to show S-Se intermixing at the CdS/CuInSe$_2$ heterojunction for less-efficient absorbers [76]. XPS and X-ray-excited Auger electron spectroscopy (XAES) were recently used to show that this S-Se intermixing can be controlled by the sulfur content in the absorber surface [77]. Here, we present our findings of a S-containing, non-CdS interlayer between the CdS buffer and the CIGSe absorber.

In addition to understanding the chemical structure at the interface, the electronic structure (*e.g.*, band alignment) is important for further optimization of the cells to understand the interplay of the different layers of the cell and their impact on the electronic structure and the final device performance. One of the most pertinent

parameters in heterojunction cells is the conduction band offset (CBO). The CBO is referenced to the absorber, where CBO > 0 indicates a "spike" in the conduction band and CBO < 0 indicates a "cliff" in the conduction band. Specifically, a "cliff" refers to the conduction band minimum (CBM) of the CdS layer that is lower than the CBM of CIGSe. There are few direct determinations of the CBO since it is difficult to investigate the unoccupied conduction band states. Often times, ultraviolet photoelectron spectroscopy (UPS) measurements are employed to derive the valence band offset (VBO) using the valence band maximum (VBM), and the CBO is calculated by assuming the surface band gap (E_g) is the same as the bulk E_g. Previously, Kronik and co-workers presented a flat alignment (-0.08 eV) for CBD CdS/Cu(In$_{0.91}$,Ga$_{0.09}$)Se$_2$ using surface photovoltage spectroscopy [13]. And more recently, Terada and co-workers suggested a flat conduction band alignment of CBD CdS/Cu$_{0.93}$(In$_{0.6}$,Ga$_{0.4}$)Se$_2$ using a rough approximation by only utilizing the VBM and CBM by UPS and IPES [78], respectively. Liu and Sites have simulated transport properties for CuInSe$_2$, where they report a maximum efficiency about 16 % for a CBO of -0.2 eV [79]. The value of the CBO is an important topic since it would affect the transport of photogenerated electrons from the absorber (*i.e.*, CIGSe) to the front contact. It is expected that a cliff in the conduction band would reduce the open-circuit voltage (V_{oc}) and increase recombination at the interface [80, 81]. Thus, there is a need to directly investigate the CBO of CBD-CdS and high-efficiency CIGSe absorbers.

6.2 Experimental Details

CIGSe absorbers were co-evaporated using the NREL three-stage process, followed by CBD-CdS deposition [5]. The CBD times were varied from 0 to 12.5 minutes. The best solar cell made from this absorber batch had an efficiency of 17.8%. Following the CBD step, the samples were briefly exposed to air and then sealed in an inert atmosphere (to minimize contamination from exposure to ambient air). Upon arrival at UNLV, they were loaded into the ultra-high vacuum (UHV) chamber, without air exposure, to be investigated by (surface-sensitive) XPS and XAES. For subsequent (bulk-sensitive) XES experiments at the ALS, samples were briefly exposed to ambient air prior to introduction into UHV.

The surfaces of the CdS/CIGSe samples were characterized by XPS and XAES at UNLV using a Mg K_α excitation source and a SPECS PHOIBOS 150MCD electron analyzer. The energy scale of the analyzer was calibrated according to Ref. 25. XES experiments were performed at Beamline 8.0.1 at the ALS, Lawrence Berkeley National Laboratory, using the soft X-ray fluorescence (SXF) endstation [36]. The S $L_{2,3}$ and Se $M_{2,3}$ spectra were excited non-resonantly with a photon energy of 200 eV, and the spectra were calibrated to the S $L_{2,3}$ emission spectrum of CdS in Ref. 82.

UPS experiments were performed with a He discharge lamp using the He I photon emission. For the inverse photoemission spectroscopy (IPES) experiments, a Geiger-Müller-like photon detector was utilized with a SrF_2 window and $Ar:I_2$ filling, and a low energy STAIB electron gun. Clean Au foil was measured by both UPS and IPES, and the Fermi edge was fitted. All energy scales of UPS and IPES spectra are referenced to the Fermi level (E_F). The VBM and CBM were determined by linear extrapolation of the

leading edges in UPS and IPES spectra, respectively. Mild Ar$^+$ ion treatment (kinetic energy 50 eV) cycles (of 15 min durations) were also utilized to prepare the surfaces.

6.3 Results and Discussion

6.3.1 Interface Formation: Chemical Structure

The evolution of the Se M$_{2,3}$ and S L$_{2,3}$ XES signal for the CdS/CIGSe series is shown in Fig. 6.1a (normalized to peak maximum). For the bare ("0 min") absorber sample (Fig. 6.1a, bottom), the observed emission is exclusively that of Se M$_{2,3}$, while for samples with CdS overlayer, the Se M$_{2,3}$ and S L$_{2,3}$ emission overlap. This is due to the fact that the Se 3p and 4s binding energies are similar to those of S 2p and 3s, respectively. The S L$_{2,3}$ emission is significantly stronger than the Se M$_{2,3}$ emission, as can be seen by the difference in magnification factor (shown in parentheses for each spectrum in Fig. 6.1). This significant intensity difference stems from the difference in fluorescence yield for the two involved transitions (S 3s $\rightarrow$ S 2p and Se 4s $\rightarrow$ Se 3p, respectively).

The Se M$_{2,3}$ emission from the bare absorber exhibits a distinct peak and a shoulder, separated by about 5.5 eV, which is in agreement with the Se 3p spin-orbit doublet separation of 5.8 eV [31]. After 0.5 min of CdS-CBD, the main peak has broadened and the Se M$_{2,3}$ doublet is less distinct, which is due to the contribution of S L$_{2,3}$ emission from the sulfur atoms deposited in the CBD process. As CBD time increases, the spectrum evolves: the main peak at ~146 eV becomes less broad and three new spectral features (at *ca*. 150.5, 151.6, and 155.7 eV) appear and become more pronounced. They are characteristic peaks for CdS [83-85], as can be easily seen when comparing with the CdS reference (Fig. 6.1a, top). The first two features are associated
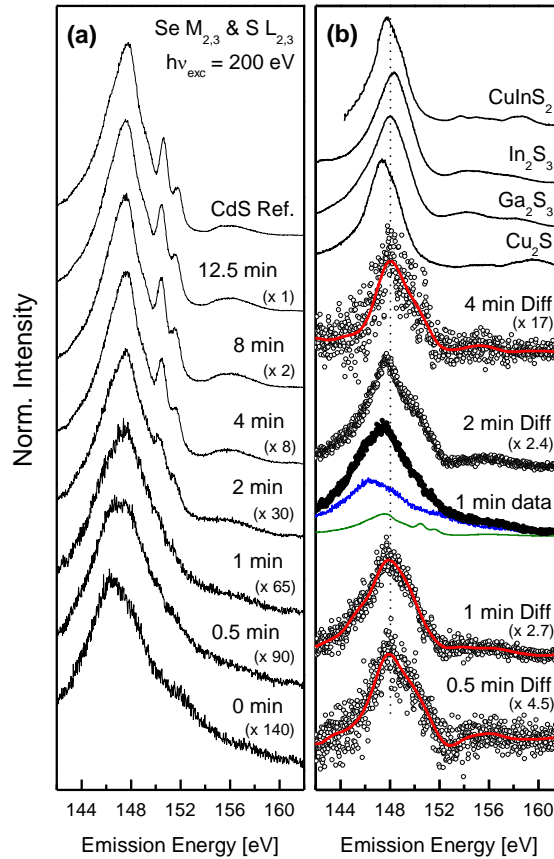
Fig. 6.1: Se $M_{2,3}$ and S $L_{2,3}$ XES spectra of (a) CBD-CdS/CIGSe sample series and a CdS reference, and (b) difference spectra (Diff) and additional sulfide references. For the Diff spectra, suitable fractions of the 12.5 min (representing S atoms in CdS) and 0 min (representing Se atoms in CIGSe) spectra were subtracted from the spectra given in the label, as shown exemplarily for the 1 min spectrum (0 min contribution in blue, 12.5 min contribution in green). A smoothed line (red) is shown for some spectra as a guide to the eye, and magnification factors are shown in parenthesis.

with a Cd 4d-derived band (hence indicating the presence of S-Cd bonds ["Cd 4d" $\rightarrow$ S $2p_{3/2}$, and "Cd 4d" $\rightarrow$ S $2p_{1/2}$ transitions]), and the third is due to electrons from the upper valence band decaying into S 2p core holes. With this assignment, we are able to monitor the spectral contributions of S $L_{2,3}$ and Se $M_{2,3}$ as a function of CBD time. For quantification, each spectrum was decomposed into a bare absorber contribution (*i.e.*, the

0 min Se $M_{2,3}$ emission spectrum of CIGSe) and a CdS contribution (*i.e,* the 12.5 min S $L_{2,3}$ emission spectrum of CBD-CdS). By subtracting a weighted fraction of each spectrum, while avoiding any negative intensity in the residual (and by varying the relative weights), it was found that the spectra of the intermediate CBD-time samples (0.5 min – 4 min) cannot be properly described with those two contributions alone. Instead, a third component in the Se $M_{2,3}$/S $L_{2,3}$ XES spectrum needs to be considered.

To shed light on this third component, we have determined the suitable weights for the 0 and 12.5 min spectra, as will be described below. The resulting residuals, representative of the third component, are shown in Fig. 6.1b for the 0.5 – 4 min CBD-CdS/CIGSe samples. To illustrate our analysis procedure, the residual ("Diff") obtained for the 1 min CBD-CdS spectrum (second from bottom) is shown below its original spectrum and the weighted CIGSe (Se $M_{2,3,}$ blue) and CdS (S $L_{2,3}$ for S in a CdS-environment, green) spectral contributions. The difference spectrum was determined by an iterative spectral subtraction of, first, the maximal possible CIGSe spectrum (while avoiding negative intensity in the residual). Then, the maximal possible amount of the 12.5 min CBD-CdS spectrum was subtracted. This approach was followed for the 0.5 and 1 min spectra, while the order of subtraction was reversed for the 2 and 4 min spectra to account for the respective predominant spectral character (Se $M_{2,3}$ of CIGSe for 0.5 and 1 min, S $L_{2,3}$ of CdS for 2 and 4 min). The resulting difference spectra (residua) do neither resemble the 12.5 min CBD-CdS spectrum nor the 0 min bare CIGSe absorber spectrum, but nevertheless exhibit a consistent and reasonable spectral shape. As found for the thinnest CdS overlayer in [76], the spectral shape of the main line is significantly more "triangular" than that of the CIGSe and CdS spectra (0 and 12.5 min, resp.), clearly

indicating the presence of a different species. Since the S 2p photoionization cross section is dominant at this excitation photon energy [58], we expect this additional species to be sulfur-related.

To shed further light on the nature of this species, the spectra of sulfur-containing candidate compounds (Cu_2S, Ga_2S_3, In_2S_3, and $CuInS_2$) are shown in Fig 6.1b. The Cu_2S and $CuInS_2$ spectra have significant (Cu 3d-derived) spectral features in the upper valence band region (~ 159 eV), which are noticeably absent from the difference spectra. Furthermore, the peak position of the main line is shifted towards lower emission energies for Cu_2S and $CuInS_2$, as compared to the difference spectra (indicated by the dotted line). In contrast, the peak position of the difference spectra is in good agreement with the Ga_2S_3 reference, and (slightly less so) the In_2S_3 reference. The difference spectra show some spectral weight at ~ 156 eV, at which Ga_2S_3, In_2S_3, and $CuInS_2$ show some valence band contributions as well (from Ga 4s- and In 5s-derived states, resp.). From this, we suggest the formation of S-In and/or S-Ga bonds during the initial stages of CdS-CBD on CIGSe (henceforth called "(In,Ga)S").

The spectral fractions (areas) of the CIGSe, CdS, and (In,Ga)S species, as determined from the analysis shown in Fig. 6.1b, are shown in Fig. 6.2 as a function of CdS-CBD time. The effective overlayer thickness of the (In,Ga)S/CdS layer (upper abscissa in Fig. 6.2) was computed using the average signal attenuation of the XPS lines of the CIGSe absorber elements (*i.e.*, Ga $2p_{3/2}$, Cu $2p_{3/2}$, In $3d_{5/2}$, and Se $3d_{5/2}$). As expected, with increasing deposition time, the CIGSe contribution (black circles) decreases, while that of CdS (red squares) increases. The (In,Ga)S contribution (blue

67
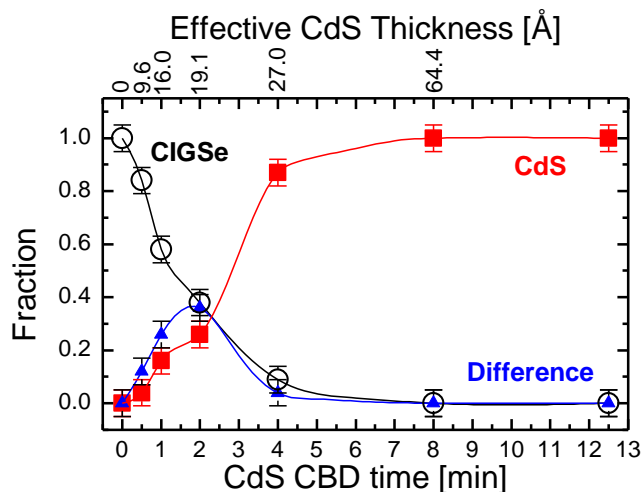
Fig. 6.2: Calculated area fraction of CIGSe (open circles), CdS (filled squares), and Diff (filled triangles) in the Se $M_{2,3}$/S $L_{2,3}$ XES spectra as a function of CdS CBD time. The effective overlayer thickness (top axis) was estimated by the photoemission attenuation of the absorber element signals. The error bar for the thickness is $\pm$ 7 Å.

triangles) first increases and then decreases with deposition time, which suggests that it is localized at the interface between CdS and CIGSe.

Now, we turn to surface-sensitive XPS and XAES to study the interface formation. Fig. 6.3 shows XPS survey spectra to elucidate the surface elemental composition of the bare CIGSe absorber and the two samples with varying CdS thickness. As expected, the intensity of photoemission lines associated with the absorber elements (*i.e.*, Cu, In, Ga, and Se) decrease with increasing CdS deposition time. Similarly, the signals, arising from Cd and S, increase with increasing CBD time. The Na 1s XPS peak (due to Na originating from the soda-lime glass substrate) is visible even after the 12.5 min CBD (Fig. 6.3c). The Na concentration is likely to decrease in the initial CBD-CdS process, but it is quite possible that some Na is localized at the interface [85]. Furthermore, Na is possibly redeposited on the surface of the sample during

immersion in the bath. All three samples exhibit C and O signals stemming from the growth process and/or contamination during sample transfer. Note that Cu, In, Ga, and Se signals are still visible at the surface of the 4 minute CBD sample, while they are absent for the 12.5 minute sample (*i.e.*, the standard buffer layer thickness of the NREL process). Apparently, the CdS layer, after 12 minutes of CBD, is a closed layer.

From the viewpoint of Cd atoms, we used XPS and XAES to analyze the interlayer formation between CdS and CIGSe. For that purpose, the modified Cd Auger parameter (α'), defined as the sum of the Cd $3d_{3/2}$ XPS binding energy and the Cd $M_4N_{4,5}N_{4,5}$ XAES kinetic energy, was derived. It is shown in Fig. 6.4, along with our and literature values [77, 86-89] for CdS (including CBD-CdS), CdSe (including CBD-CdSe), and CdO. The Cd $3d_{3/2}$ line was chosen (instead of the $3d_{5/2}$ line) to avoid the $3d_{3/2}$ satellites of Mg $K_{\alpha3,4}$ excitation, which overlap with the $3d_{5/2}$ peak. To show α', we have
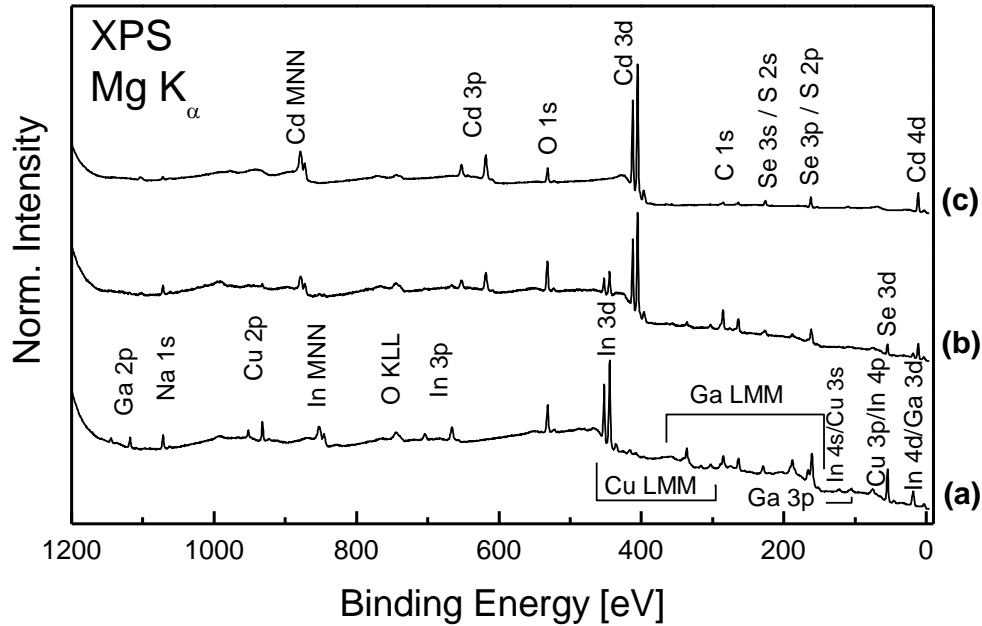
Fig. 6.3: XPS survey spectra of (a) the bare CIGSe, (b) a 4 minutes, and (c) a 12.5 minutes CBD-CdS layer on the CIGSe absorber.

first assumed that the Cd atoms exist in one single chemical environment (stars); α' first increases (up to 793.3 ± 0.1 eV at 1 min) and then decreases (from 2 to 4 min) to a constant value of 793.1 ± 0.1 eV (note that this decrease was also previously reported in Ref. 77). While all of the observed α' values lie within the reference values for CdS, this α' behavior clearly indicates the presence of a second Cd species. We thus reanalyzed the data assuming a second Cd-containing chemical species in the following way. A suitably weighted 12.5 min CdS-CBD spectral contribution (representative of CdS) was subtracted from the Cd $M_4N_{4,5}N_{4,5}$ feature of the 0.5, 1, and 2 min CdS-CBD samples, to produce a residual with the characteristic Cd $M_4N_{4,5}N_{4,5}$ Auger lineshape. In agreement with the concept of a second species, this residual Cd $M_4N_{4,5}N_{4,5}$ Auger emission was found at a different kinetic energy (note that the Cd $3d_{3/2}$ XPS line did not show a change in shape and thus was not deconvoluted into two separate Voigt profiles at different energies). α' was then re-computed for the two different species (triangles and circles) of the 0.5, 1, and 2 min CdS-CBD samples, as also shown in Fig. 6.4. The lower α' values are in good agreement with the CdS values found at longer deposition time, while the higher α' values are within the range of reported CdO values, and somewhat larger than those reported for CdSe [87, 89]. An unambiguous assignment based only on this analysis appears difficult. Nevertheless, the analysis strongly indicates the presence of two distinct Cd species in the initial growth stage, and we speculate that the second species (*i.e.*, beyond the expected CdS) presumably involves Se atoms that are liberated by the above-described (In,Ga)S formation. This finding is in agreement with our recent report of a Se diffusion into the CdS buffer that depends on the S concentration at the surface of $CuIn(S,Se)_2$ absorbers [77].
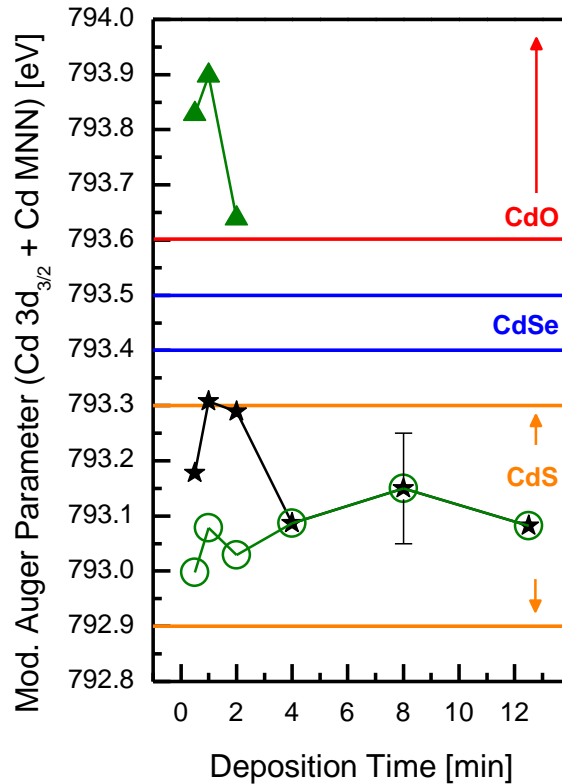
Fig. 6.4: Modified Cd Auger parameter α' using the Cd $3d_{3/2}$ and Cd $M_4N_{4,5}N_{4,5}$ lines of each sample. Stars represent α' values obtained by assuming only one Cd species in each sample. The open circles and triangles were determined by spectral subtraction, assuming two Cd species (the triangle-related species could only be discerned for 0.5, 1, and 2 min of CdS CBD). Error bars are ± 0.1 eV, as shown for the 8 min data.

6.3.2 Interface Formation: Electronic Structure

Even with a careful packing procedure and minimized air exposure, the bare CIGSe sample shows contaminations with carbon- and oxygen-containing species. On the surface of the CIGSe sample, there was considerably more oxygen (*i.e.*, O 1s) compared to that of the In 3d signal (see Fig. 6.5, bottom spectrum). Thus, to accelerate the cleaning process of the surface, the bare CIGSe sample were rinsed in aqueous ammonia (~ 1M) for 1 min at room temperature, followed by a rinse in deionized water for 0.5 min, and
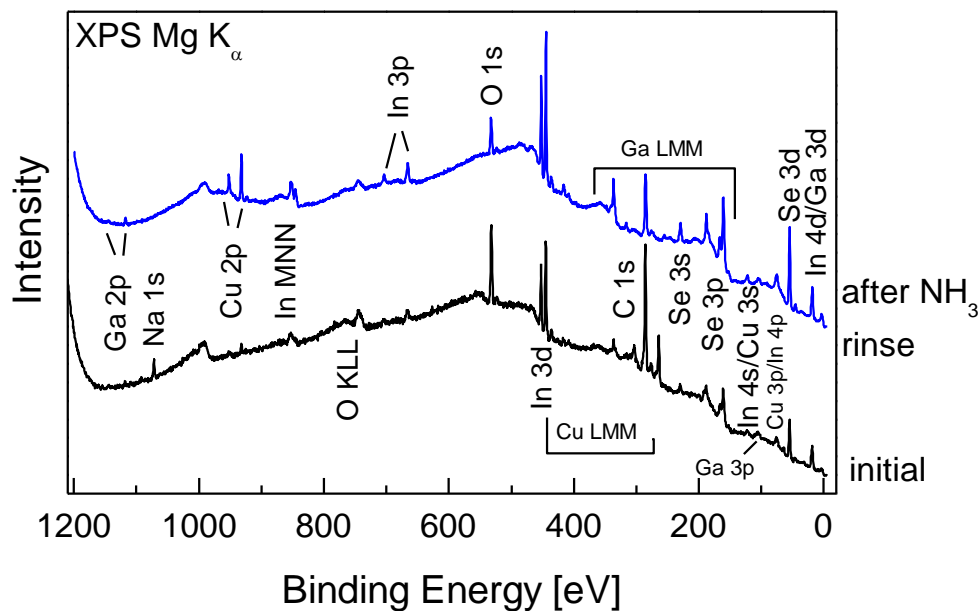
Fig. 6.5: XPS survey spectra of the bare CIGSe sample before (bottom, black) and after (top, blue) an aqueous ammonia rinse.

dried in N_2 environment that was directly connected to the UHV chamber (for IPES and UPS characterization). The ammonia rinse substantially reduced the amount of O content in the surface of the sample (Fig. 6.5, top spectrum). However, the rinse has also reduced the surface content of Na, which may also influence the surface electronic structure.

In Fig. 6.6a, the UPS and IPES spectra of the bare CIGSe sample are shown after the ammonia rinse and subsequent ion sputter steps. The ammonia-rinsed spectra (Fig. 6.6a, bottom) result in an artificially large E_g largely due to the still remaining surface contamination. As the ion treatments are performed, the VBM and CBM begin to move towards the E_F (and subsequently narrowing the E_g) as the sputtering steps have removed O- and C-containing contaminants on the surface. After the second 15 min Ar^+ ion treatment cycle (Fig. 6.6a, top), we find that the VBM and CBM are -0.72 ($\pm$ 0.1) eV and

0.96 ($\pm$0.1) eV, respectively. These results give a surface E_g of 1.68 $\pm$ 0.15 eV, which is in agreement with our previous measurements of CIGSe absorbers [90]. The E_F position indicates that the surface is p-type.

Similarly, for the thickest CdS layer (*i.e.,* 12.5 min CBD), the E_g is artificially wide due to surface contaminants (Fig. 6.6b, bottom). Note that the 12.5 min CBD CdS/CIGSe sample did not undergo an ammonia rinse as it displayed significantly less O- and C-containing contaminants. After the first 15 min ion treatment step (Fig. 6.6b, second from bottom), the valence band features of CdS are noticeable. After the third sputter cycle (Fig. 6.6b, top), we determine the VBM and CBM as -1.84 ($\pm$ 0.1) eV and
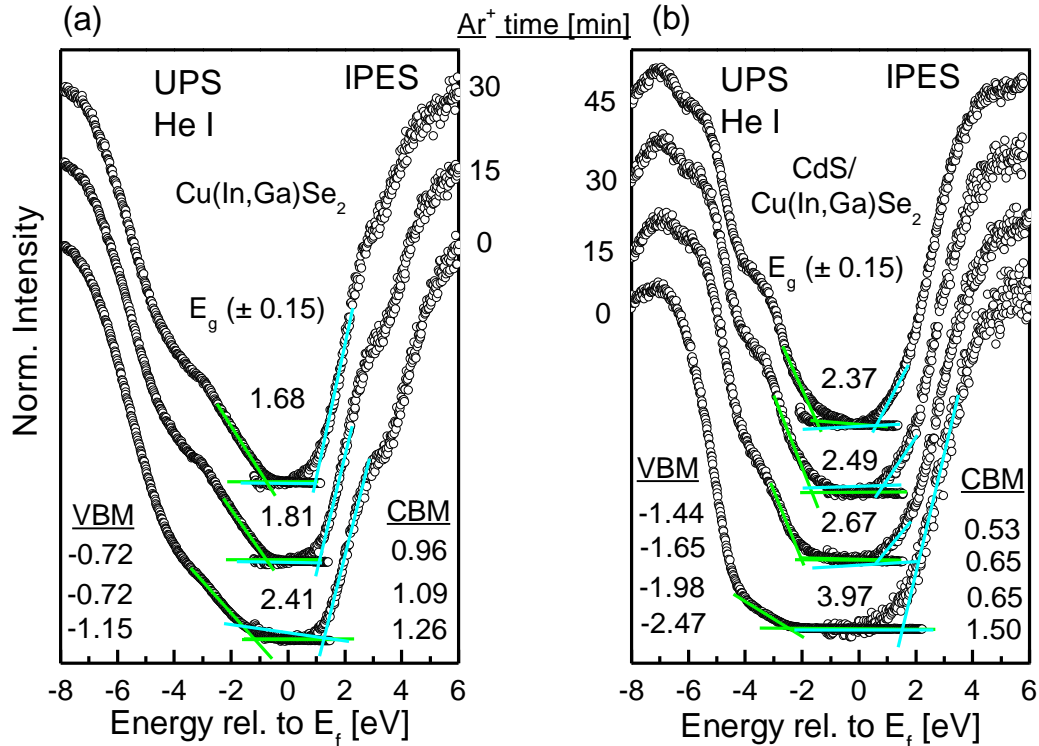
Fig. 6.6: He I UPS and IPES spectra of the (a) CIGSe, and (b) 12.5 min CBD CdS/CIGSe sample. The left and right side of each panel displays the UPS and IPES spectra, respectively. The resulting electronic surface band gap (E_g) derived from each pair of spectra is given.

0.53 ($\pm$0.1) eV, respectively, and a surface E_g of 2.37 $\pm$ 0.15 eV. Our E_g measurement of CBD-CdS is close to the reported bulk E_g [91].

As a rough approximation, the band alignment can be estimated with the VBM and CBM positions of the bare CIGSe and CdS/CIGSe. However, for a finer approximation of the band alignment, the effects of an interface-induced band bending (IIBB) from the perspective of the substrate (*i.e*., CIGSe) towards the CdS layer must be considered. For this, we have used the samples with intermediate CBD-CdS times 0.5, 1, 2, and 4 min where the core-level PES lines from the absorber are still "visible" by XPS. For the absorber, the Cu $2p_{3/2}$, In $3d_{3/2}$, Ga $2p_{3/2}$, and Se $3d_{5/2}$ lines were used and the peak center determined by a Voigt fit. For the CdS overlayer, the Cd $3d_{3/2}$ and S $2p_{3/2}$ lines were used and peak center determined by Voigt fit. The core-level shift of the absorber as a function of CBD time t relative to the bare absorber of the absorber is shown in Fig. 6.7. The core-level shifts of the Cu $2p_{3/2}$, In $3d_{3/2}$, and Se $3d_{5/2}$ behave similarly, while the shift of the Ga $2p_{3/2}$ is significantly smaller. Since the difference is positive, the core-levels of the absorber move downwards (to higher E_B) after the deposition of CdS. This result implies an interface-induced band bending is present between the CIGSe absorber and CdS buffer layer.

The IIBB was calculated as follows,

$$IIBB = -[(E^0_{CIGSe,i} - E^t_{CIGSe,i}) + (E^t_{CdS,j} - E^{12.5}_{CdS,j})]$$

where $E^0_{CIGSe,i}$ is the PES line of element i in the bare absorber, $E^t_{CIGSe,i}$ is a PES line of absorber element i after a CBD time of t, $E^t_{CdS,j}$ is a PES line of element j in CdS at t, and $E^{12.5}_{CdS,j}$ is a PES line of an element in CdS at 12.5 min CBD. In total, 32 values of IIBB were determined with different combinations of CIGSe lines and CdS lines, and these are
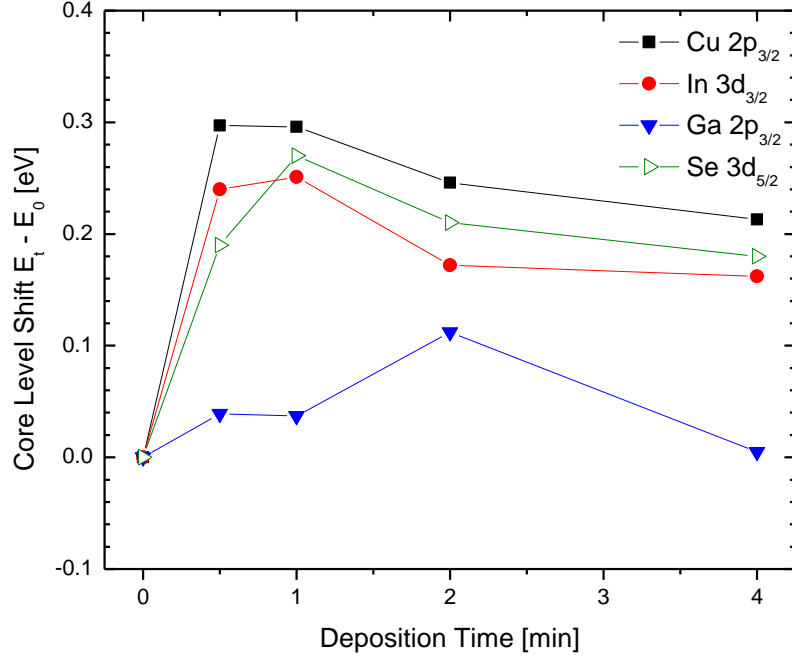
Fig. 6.7: Core level shifts, $E_t - E_0$, of the absorber lines Cu $2p_{3/2}$, In $3d_{3/2}$, Ga $2p_{3/2}$, and Se $3d_{5/2}$. E_t is the absorber line position after t CBD time, while E_0 is the core level energetic position of the bare absorber. The error bar is ± 0.07 eV.

summarized in Fig. 6.8. The average value for IIBB is 0.27 ± 0.15 eV (as indicated by the dashed line in Fig. 6.8). Finally, the VBO and CBO are determined as follows,

$$VBO = VBM_{CdS} - VBM_{CIGSe} + IIBB \text{ , and}$$

$$CBO = CBM_{CdS} - CBM_{CIGSe} + IIBB.$$

Thus, we find that the VBO and CBO are -0.85 ± 0.15 and -0.16 ± 0.15 eV, respectively.

We find that the conduction band alignment is "cliff-like" with a CBO of -0.16 eV. This results in a non-ideal band alignment at the CdS/CIGSe interface which would impede the charge carriers going across this interface. For CuInSe$_2$, it is predicted that a small cliff-like CBO will not drastically degrade transport properties of the CdS/CuInSe$_2$ junction [79]. Thus, in light of our findings of a cliff-like conduction band alignment, we
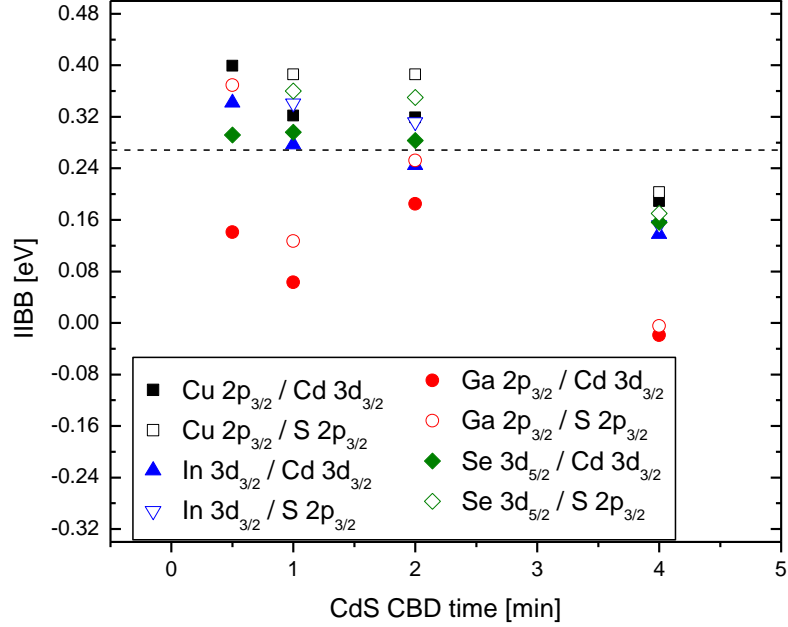
Fig. 6.8: Corrections for the interface-induced band bending as determined by combining core-level positions of the absorber (CIGSe), a thick CdS (12.5 min CBD), and four CdS/CIGSe of intermediate CdS thickness.

also propose that conduction band alignment, although not favorable, is not detrimental since the best device made from this absorber batch had an efficiency of 17.8%.

6.4 Summary

In summary, our findings give direct experimental evidence for the presence of a S-containing interlayer between CdS and the CIGSe absorber, most likely in the form of $(In_{1-x}Ga_x)_yS_z$. Furthermore, we find experimental evidence for an additional Cd-containing species and speculate that it could involve Se atoms liberated by the $(In_{1-x}Ga_x)_yS_z$–formation. These findings are in good agreement with our earlier, significantly more indirect, observation of a S-Se intermixing at the CdS/CIGSe interface [76, 77]. The

interface structure is highly complex, with large impact on the electronic properties of the buffer/absorber interface, and the fundamental concept of S/Se exchange appears to hold true even for the here-investigated high efficiency thin film solar cell systems. We have also directly investigated the electronic band alignment at the CdS/CIGSe interface, and find an unfavorable "cliff-like" band alignment. These results provide a comprehensive overview of the interface formation between CdS and CIGSe, and should provide insight for future optimization in the CIGSe system.

CHAPTER 7

SURFACES AND INTERFACES IN CdTe/CdS

7.1 Introduction

CdTe-based solar cells have reached efficiencies of up to 16.5% on the laboratory (small area) scale [6], and manufacturing costs of commercial CdTe modules are reported below $1/W_p$ [92]. For efficient CdTe cells, it is generally necessary to perform a $CdCl_2$ treatment ("activation") of the CdTe/CdS layer stack [17]. In addition, Cu-containing back contacts on CdTe are best formed after heat treatment in oxygen or air [19, 20, 21]. Numerous studies (*e.g.*, [20, 21, 22, 93, 94]) have reported diffusion processes at different interfaces in CdTe cells as a result of post-absorber deposition treatments. For Au/Cu back contacts, studies report Cu migration towards the front contact as a result of the oxygen (or air) annealing process [20, 93], and Cu affecting the electrical properties of a CdTe cell (*e.g.*, Ref. [95]).

Sputter depth-profile techniques have been used to investigate the effect of $CdCl_2$ and/or back contact (BC) treatments (*e.g.*, Ref. [21,96-98]), but these techniques are destructive and suffer from a variety of shortcomings, including preferential sputtering, sputter-induced mixing, and matrix effects. Based on an initial study of sulfur migration by X-ray emission (XES) and cross-sectional energy dispersive X-ray (EDX) spectroscopy [99], we have designed and produced a combinatorial sample set that allows us to separate the effects of each post-absorber deposition treatment and to study the sulfur migration and morphology of the back contact in detail. For this purpose, we have used XES, which is sensitive to the surface-to-near bulk, surface-sensitive X-ray photoelectron spectroscopy (XPS), and atomic force microscopy (AFM) to non-

destructively paint a complementary picture of the back contact morphology and chemical interface structure of CdTe-based solar cells as a function of post-absorber deposition treatment. We have used a suitable lift-off technique to probe initially buried interfaces with surface-sensitive X-ray photoelectron spectroscopy (XPS) to study the impact of the $CdCl_2$ and contact heat treatments on the chemical composition at the various surfaces and interfaces.

7.2 Experimental Details

CdTe (2 µm) and CdS (0.13 µm) thin films were deposited by R.F. magnetron sputtering at 45° onto a rotating SnO_2:F-coated glass substrate (Tec-15™ by Pilkington plc) held at 270°C. Four identical CdTe/CdS/SnO_2:F/glass samples were made, but after deposition of the CdTe layer, each sample underwent a different series of post-absorber deposition steps: (1) $CdCl_2$ activation, followed by Au/Cu deposition and BC treatment (henceforth labeled "both treatments"), (2) $CdCl_2$ activation, followed by Au/Cu deposition, but no BC treatment ("$CdCl_2$-treated"), (3) Au/Cu deposition without prior $CdCl_2$ activation, followed by BC treatment ("BC-treated"), (4) Au/Cu deposition without prior $CdCl_2$ activation and without subsequent BC treatment (*i.e.*, the control sample, "untreated"). The $CdCl_2$ activation was performed by evaporating a saturated $CdCl_2$ /methanol solution from the CdTe surface and annealing the samples at 390°C for 30 minutes in dry air, followed by a methanol rinse. The Au(10 nm)/Cu(4 nm) BC was thermally evaporated through a mask at room temperature, and the BC treatment was performed at 150°C in room air for 45 minutes. The Au/Cu/CdTe/CdS/SnO_2:F/glass samples were sealed in dry N_2 (at Toledo) and shipped to UNLV. The samples were then unpacked in an N_2-ambient

glovebox prior to transfer into ultra-high vacuum (UHV) for XPS characterization (*i.e.*, to avoid additional air exposure). After XPS analysis, the samples were packed in dry nitrogen again and shipped to the ALS for XES experiments in UHV after a brief (less than 5 minutes) air exposure. Finally, samples were again shipped to UNLV under dry nitrogen for AFM studies (in air). The average efficiency of the solar cells made from this batch was found to be 11.5%.

For the lift-off procedure, the sample was removed from UHV and the "back" surface was glued to a stainless steel plate (in air) using UHV-compatible conductive epoxy (EPO-TEK® H21-D). The glue was cured at 35-40°C for three hours, and then cured overnight at room temperature. The sample was re-introduced into the N_2-filled glovebox and cleaved. In addition, reference TeO_2 powder, a Te lump, CuTe powder, and a CdTe thin film (2 μm) were measured by XPS.

S $L_{2,3}$ XES measurements were performed at the SXF endstation of Beamline 8.0.1 [36] at the ALS, using an excitation photon energy of 200 eV. Energy scales were calibrated according to Ref. 83. For the XPS measurements, a Mg K_α excitation source and a Specs PHOIBOS 150MCD analyzer (calibrated according to Ref. 25) were used. Contact-mode AFM was performed with a Park XE-70 instrument.

7.3 Results and Discussion

7.3.1 Effect of Post-Absorber Treatments

AFM images (10×10 μm^2) of the four samples are shown in Fig. 7.1. The surface of the untreated sample (Fig. 7.1a) consists of uniformly small grains (d ≈ 0.5 μm). In contrast, the surface morphology of the CdCl$_2$-activated sample (Fig. 7.1b) exhibits larger grains
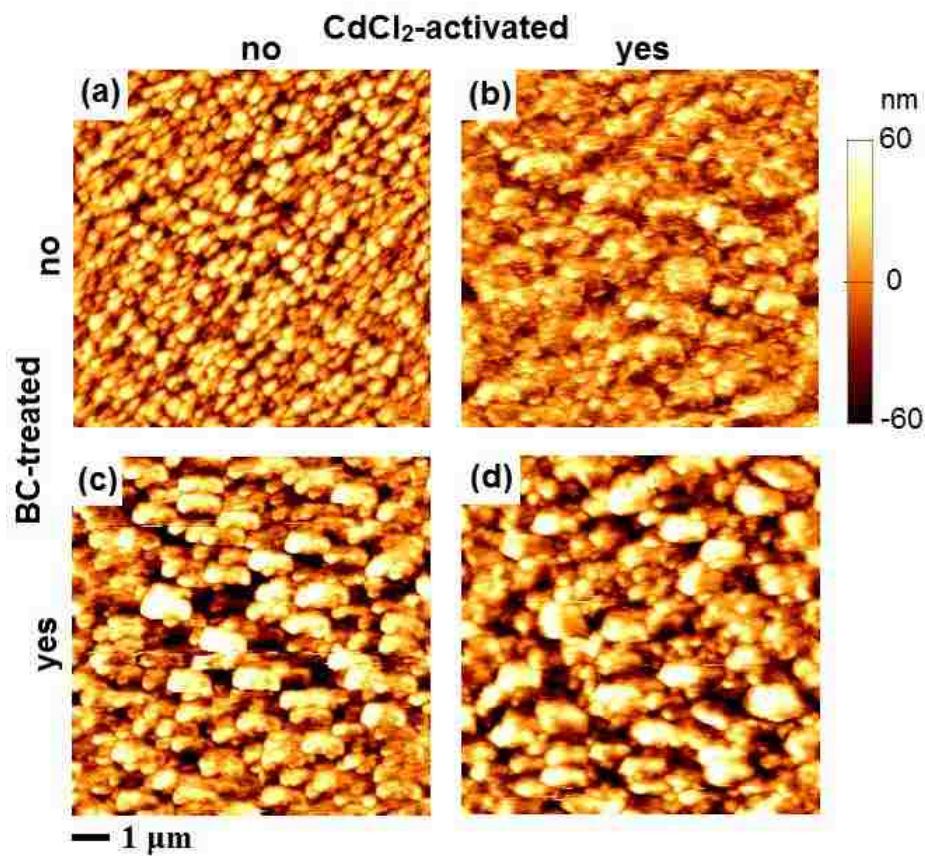
Fig. 7.1: $10 \times 10 \ \mu m^2$ AFM images of the (a) "untreated", (b) "CdCl$_2$-activated", (c) "BC-treated", and (d) "both treatments" samples.

as well, which indicates that the CdCl$_2$ activation affects the surface morphology of the CdTe absorber and the overlying BC layers. As visible in Fig. 7.1c, the surface of the BC-treated sample also shows larger grains than the untreated sample. For the "both treatments" sample (Fig. 7.1d; as for a typical CdTe solar cell), the surface morphology is most similar to that of the CdCl$_2$-activated sample, again with larger grains and some finer features.

In Fig. 7.2, the XES S L$_{2,3}$ emission of the four samples are shown, together with spectra of CdS and CdSO$_4$ references (spectra were normalized to the peak height of the

largest peak; the magnification factors are shown next to each spectrum). All samples exhibit a distinct sulfur emission, which suggests significant sulfur diffusion (as reported earlier [99-101]) – a 2 μm thick CdTe film would attenuate the S signal of a buried CdS layer by approx. 10^6 (based on attenuation lengths given in [34]). Also, an inhomogeneous surface coverage cannot be entirely ruled out. The S $L_{2,3}$ signal is strongest (and similar) for the two samples which underwent $CdCl_2$ activation (as indicated by the smaller magnification values). In contrast, the S $L_{2,3}$ emission from the sample that only underwent the BC treatment is most attenuated. CdS (thin film; bottom spectrum) and $CdSO_4$ (powder, Alfa Aesar; top spectrum) references were also measured and shown in Fig. 7.2. In all samples, the presence of S-Cd bonds is clearly present (as indicated by the pronounced Cd 4d-derived band at 150.5 and 152 eV, marked with dotted vertical lines) [76]. We note that this presence of S-Cd bonds appears more pronounced after the $CdCl_2$ activation, suggesting that this treatment plays an important role in S migration and the formation of S-Cd bonds. In addition, the presence of an oxidized sulfur species is also observed in all four samples (as indicated by the S 3s- and 3d-derived states, most easily seen for the $CdSO_4$ reference spectrum and marked with dashed vertical lines in Fig. 7.2) [102]. Sulfur oxide formation is most pronounced for the $CdCl_2$-activated and "both treatments" samples, and likely caused by the $CdCl_2$ activation performed in methanol and/or air. As a first summary, we thus find that sulfur atoms migrate towards the BC as a result of the $CdCl_2$ treatment. While most of the S atoms are found to be in S-Cd bonds [*e.g.*, in a CdS or Cd(S,Te) environment], some are present in an oxidized form.
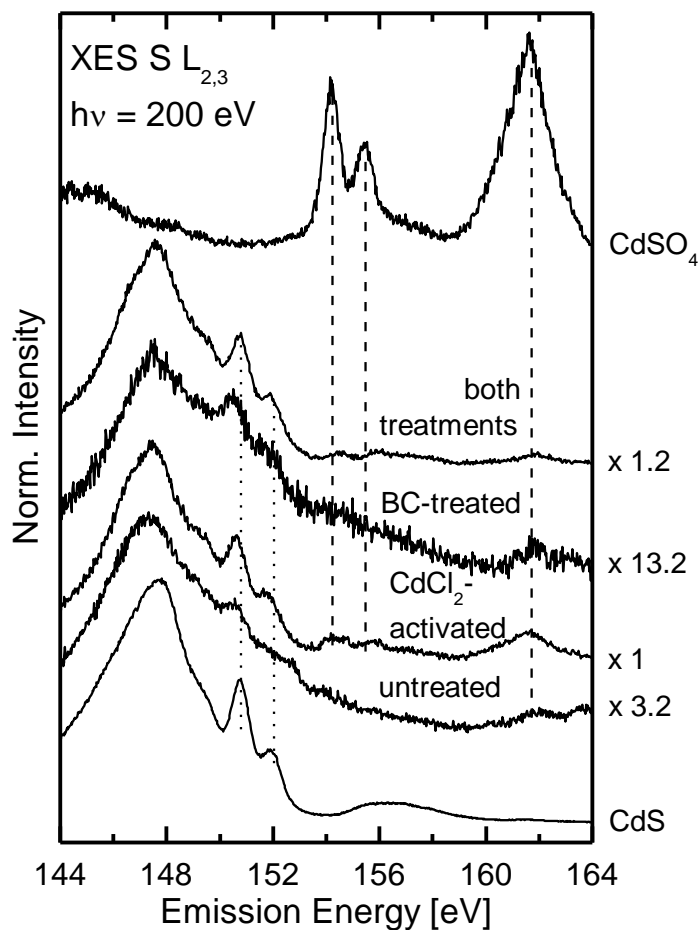
Fig. 7.2: S $L_{2,3}$ XES spectra of the various CdTe/CdS samples, together with reference $CdSO_4$ and CdS spectra.

To investigate the possible presence of sulfur directly at the back surface, we have employed surface-sensitive XPS (the attenuation length of the analyzed photoelectrons is approx. 5-10 Å). Survey spectra of the four samples are shown in Fig. 7.3. The XPS signals arising from the untreated sample (Fig. 7.3, bottom) are (as expected) dominated by Au and Cu signals, with some contribution from C and O. Similarly, the surface of the $CdCl_2$-activated sample is composed of Au, significantly reduced concentrations of Cu,

C, and O, and additionally Cd, Cl, and Te. The surface composition of the BC-treated sample is similar to that of the untreated sample, where the observed signals are due to Au and Cu (and some C and O). Also, the BCs of the untreated and BC-treated samples appear to be fully closed, since no Cd and Te signals are detected by XPS. This
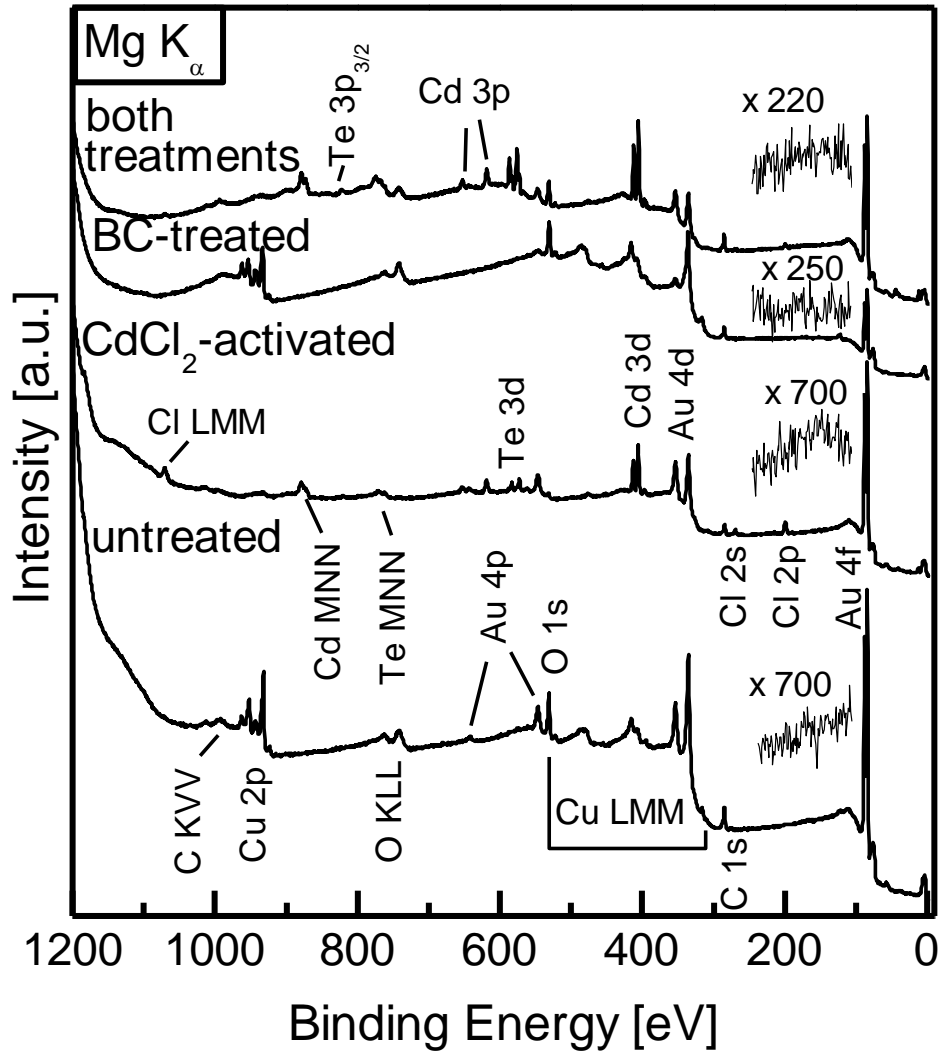
Fig. 7.3: XPS survey spectra of the four samples. The magnified detailed spectra (160 – 165.5 eV) of the (absent) S 2p line are also shown above each survey spectrum.

corroborates the XES results that the S signal is most attenuated for the BC-treated sample.

Upon closer inspection, the Cu/Au signal ratio of the BC-treated sample is larger than that of the untreated sample. This suggests a diffusion of Cu (towards the back surface) and/or Au (towards the CdTe absorber) caused by the BC treatment. For the "both treatments" sample, the spectrum resembles that of the CdCl$_2$-activated one, for which Au, Cd, Cl, and Te signals are detected at the surface. Surprisingly, no Cu signal is observed, similar to the very weak Cu signal of the CdCl$_2$-activated sample; this will be discussed in conjunction with Fig. 7.4 below.

Detailed XPS measurements in the S 2p region were performed, but no S 2p signal was detected from any of the four samples (the detail spectra are shown above each survey spectrum in Fig. 7.3, and their intensity magnification factors are given), indicating that (at most) only a negligible amount of sulfur atoms is present at the surface. Detailed XPS spectra of the Cu $2p_{1/2}$ region (instead of the $2p_{3/2}$ to avoid the $2p_{1/2}$ satellites of Mg K$_{\alpha 3,4}$ excitation) are shown in Fig. 7.4 for all samples, with a bar indicating the spread of literature values for metallic Cu, Cu$_x$S, and Cu$_x$O [31]. The Cu atoms at the surface of the untreated sample are in at least two different chemical environments, as indicated by the main peak at 951.8 eV ("metallic"), a pronounced shoulder at *ca.* 954.1 eV, and a double-peak structure at 961-964 eV. The latter two features are indicative of copper in a higher oxidation state – Cu(II) (*i.e.*, CuS and/or CuO) contributes to both, the shoulder and the double-peak structure, while Cu(I) (*i.e.*, Cu$_2$S and/or Cu$_2$O) contributes only to the shoulder [103 and references therein]. Similarly, the BC-treated sample also exhibits Cu(II) and, most likely, Cu(I) species. The
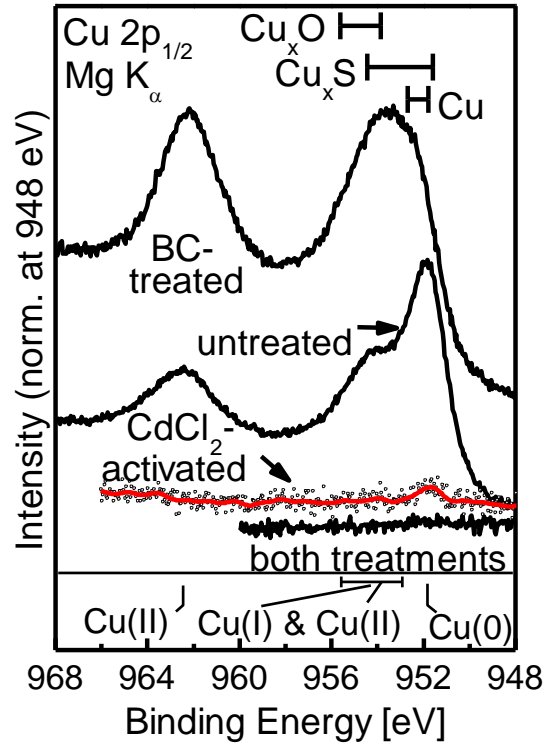
Fig. 7.4: XPS Cu $2p_{1/2}$ spectra of the four samples. The horizontal bars above the spectra indicate the literature spread of values for Cu, Cu_xO, and Cu_xS [31]. The bottom portion denotes our assignment of the Cu oxidation state in our spectra.

presence of oxidized copper at the surface is not surprising since the BC treatment is performed in air.

In contrast, the Cu $2p_{1/2}$ signal from the $CdCl_2$-activated sample is significantly decreased in intensity and "metallic", and it is completely absent for the "both treatments" sample. As learned from the AFM images, the morphology of the Au/Cu BC is strongly affected by the $CdCl_2$ activation. Thus, two explanations appear feasible: either the modified morphology allows an enhanced diffusion of Cu into the CdTe film, and/or the Au layer covers the Cu layer more efficiently (completely), thus attenuating its

XPS signal. The fact that a Te signal is observed for both samples that underwent CdCl$_2$ activation, XPS studies after sample cleavage (see section 7.3.2), and Cu XES spectra (not shown) suggest that the Cu atoms indeed diffuse into the CdTe [or Cd(S,Te)] layer and neither are entirely removed during the treatment steps nor localized at only the back surface.

7.3.2 Lift-off investigation of a CdTe/CdS solar cell

As a result of the cleaving process, two new surfaces are exposed: one on the back contact side, *i.e.*, on the side of the stainless steel carrier plate ("LO-SS" for "lift-off stainless steel"), and one on the front contact side, *i.e.*, on the side of the glass superstrate ("LO-g"). A schematic which displays the surfaces that were analyzed is shown in Fig. 7.5. The XPS survey spectra of the "back", LO-SS, and LO-g surfaces are shown in Fig. 7.6. The spectrum of the "back" surface (Fig. 7.6, top) shows Au, Cd, Te, and Cl signals. Signals stemming from the Cu 2p lines (expected at binding energies of 933 and 952 eV
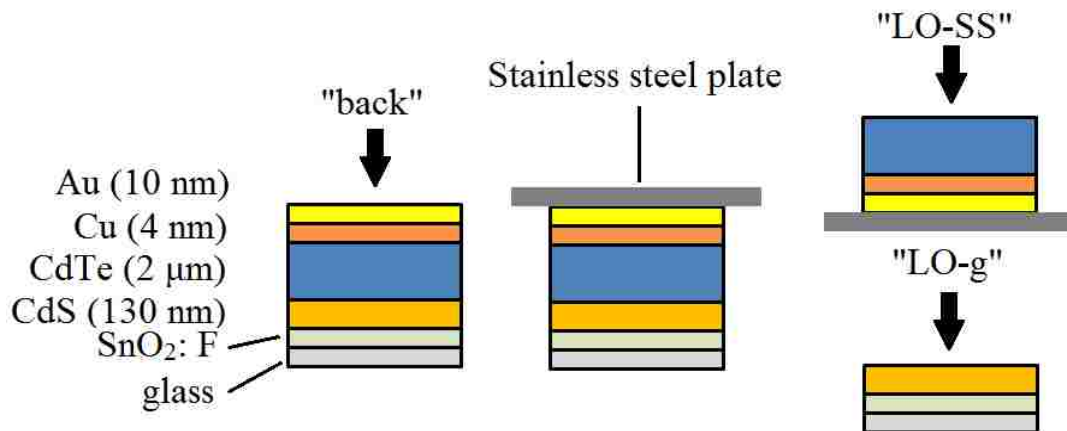
Fig. 7.5: Schematic of the CdTe solar cell measured before and after lift-off. The arrows indicate the surfaces that were analyzed.

87

[73], resp., and indicated in Fig. 7.6) are absent [the broad feature at 940 eV is due to a Cd Auger line, which is corroborated by the survey spectra taken with Al K_α excitation (not shown)]. However, detailed spectra of the Cu 2p region using Al K_α excitation show a very weak signal. Also note that XPS signals ascribed to Te (and Cd) can be observed on the "back" surface, which indicates that the initial top Au/Cu layer is not closed (possibly due to insufficient cover layer thickness and/or morphological changes during the contact heat treatment). Back in Fig. 7.1, the AFM images (10 x 10 μm^2) of the "back" contact surfaces of the sample (a) without any treatments, and (d) with both the CdCl$_2$ and contact heat treatments, are shown. The "back" of the fully treated sample (Fig. 7.1d) displays voids, which supports our XPS observation of an inhomogeneous contact layer.
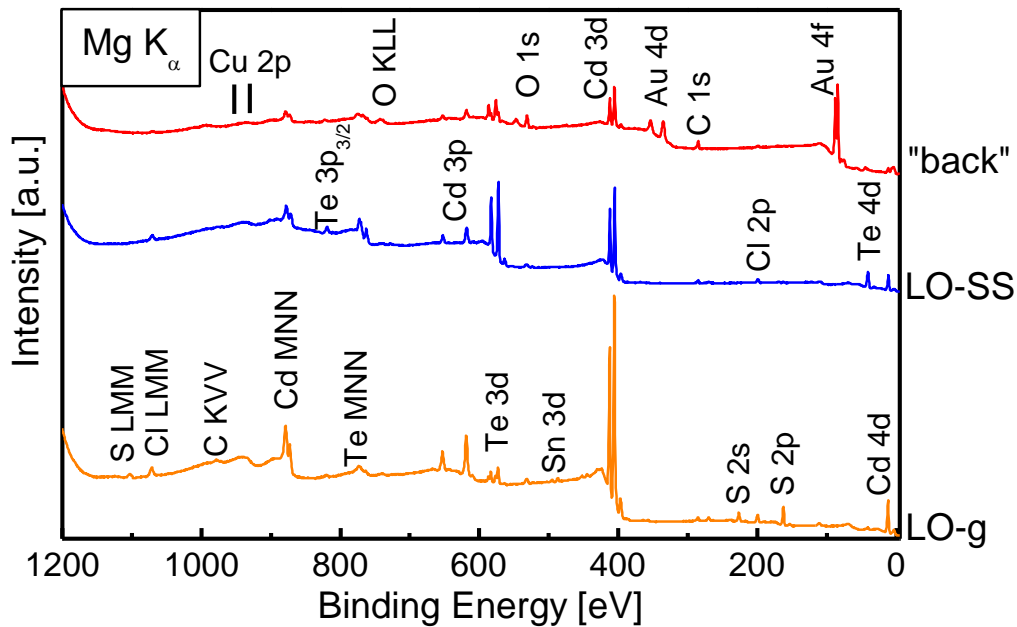
Fig. 7.6: XPS survey spectra of the "back" (top), LO-SS (center), and LO-g (bottom) surfaces of the sample, with all observed elements labeled. The Cu 2p binding energy positions are also indicated (with vertical lines).

While for the "back" sample, we find some contamination with carbon and oxygen (probably due to the $CdCl_2$ activation and/or back contact formation process), both cleaved surfaces show considerably less contribution from C and O. The LO-SS surface is dominated by signals from Te and Cd, while the LO-g surface shows only a weak Te signal. This suggests that the cleavage takes place close to the CdTe/CdS interface, with some CdTe remaining on the LO-g surface (either as individual grains or clusters). Alternatively, Te could have diffused (in)to the CdS layer. On the LO-SS surface, we find a very weak signal contribution from S (corroborating the interpretation of the cleavage location) and a significant Cl signal. It appears that (some of) the Cl atoms from the $CdCl_2$ activation have diffused through the CdTe layer, as has been reported before [104]. The LO-g surface is primarily dominated by Cd and S lines (where the Cd:S ratio is in close agreement to stoichiometric CdS), with Te, Cl, and Sn signals present as well.

The Te 3d core level spectra of the different surfaces are shown in Fig. 7.7 (along with other Te-containing references). Te is present at all three sample surfaces, and its signal is strongest for the LO-SS surface. The Te atoms on both the "back" and LO-g surfaces are in (at least) two different chemical environments, as seen by the presence of two peaks for each, the Te $3d_{3/2}$ and Te $3d_{5/2}$ core level contributions. The low-binding energy component (for either the $3d_{3/2}$ or $3d_{5/2}$) is common on all three surfaces and in energetic agreement with CdTe, CuTe, and/or elemental Te. Due to the very weak Cu signal, we believe that the contribution from Te atoms in a CuTe environment to the low-binding energy spectral feature is very small (if any). Furthermore, the modified Auger parameter was determined (using the position of the Te $3d_{3/2}$ and Te MNN), and the

89
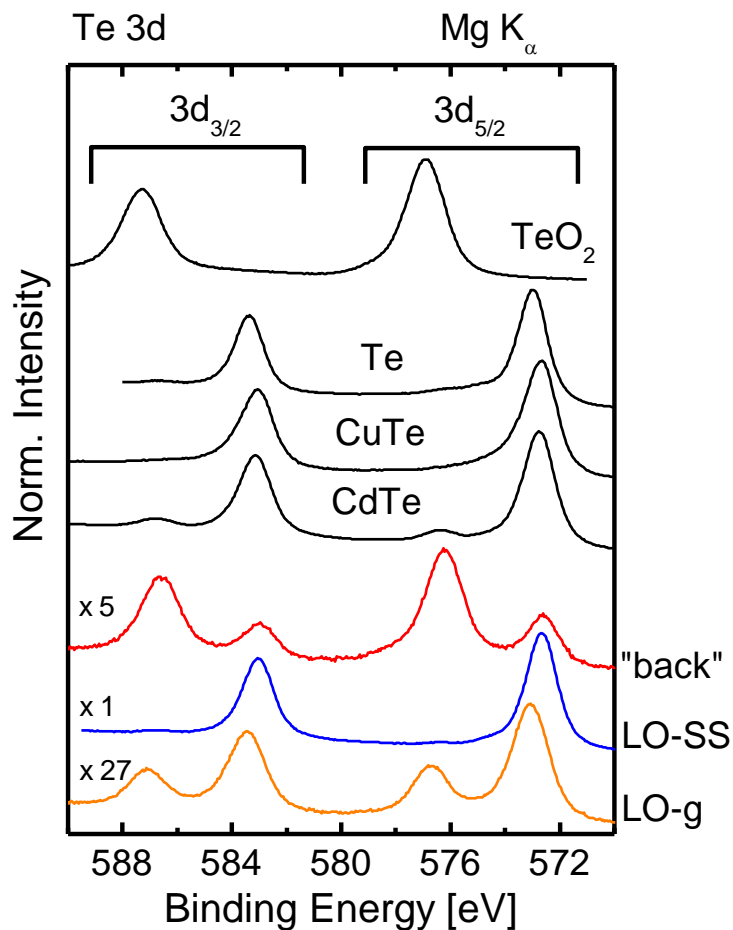
Fig. 7.7: Te 3d XPS detail spectra of the "back", LO-SS, and LO-g sample. The magnification factor of the spectrum of sample is also shown. Reference spectra of a CdTe thin film, a CuTe powder, an elemental Te lump, and TeO_2 powder are shown for comparison.

lower binding energy feature for the Te 3d is in good agreement with literature values for CdTe, but not for elemental Te [30]. The higher binding energy feature present on the "back" and LO-g surfaces is in agreement with the TeO_2 reference (and respective oxide literature values [30]).

Further analysis in the form of spectral fits, only using the CdTe and TeO_2 reference spectra, was then performed on the Te $3d_{3/2}$ region, as shown in Fig. 7.8. The
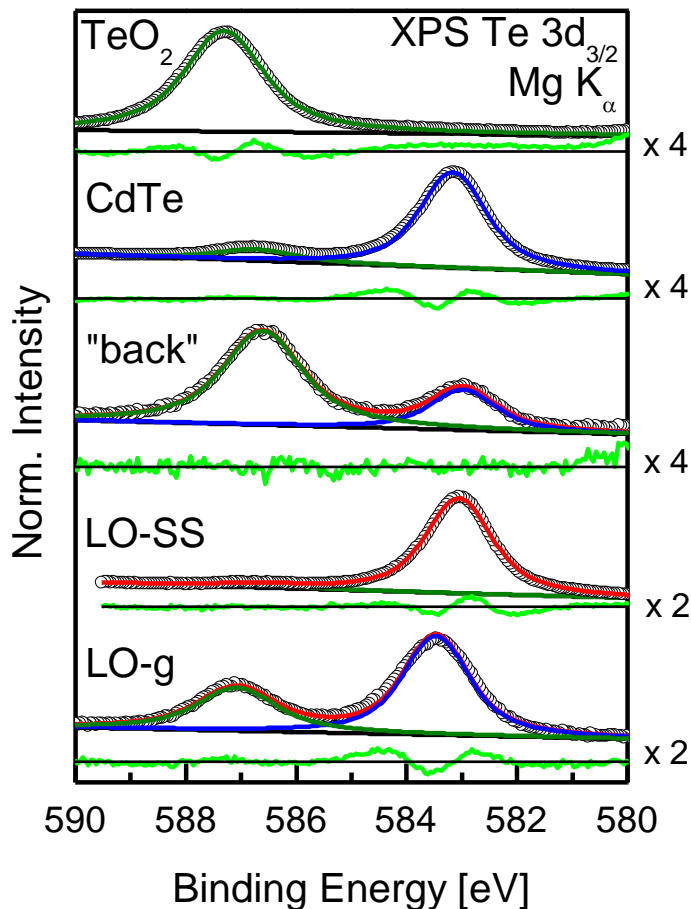
Fig. 7.8: Spectral fits of the Te $3d_{3/2}$ region of the "back", LO-SS, and LO-g samples together with those of CdTe and TeO_2 references. Data are shown as points, and fits are shown as solid lines (blue: CdTe, green: TeO_2, red: sum spectra).

$3d_{3/2}$ lines were chosen (instead of the stronger $3d_{5/2}$ lines) to avoid spectral distortion by the $K_{\alpha3,4}$ satellites of the non-monochromatized Mg $K_{\alpha3,4}$ x-ray excitation. The Te $3d_{3/2}$ region of the "back", LO-SS, and LO-g samples were fitted simultaneously, using the fitted peak parameters of CdTe and TeO_2 reference spectra (shown in Fig. 7.7). In all fits the Gaussian width for all peaks and Lorentzian widths for all components were coupled. From the fit results, the fraction of Te atoms in a CdTe- and a TeO_2-like chemical

environment can be determined, as shown in Fig. 7.9. We find that the oxide contribution is largest for the "back" side of the sample, which may arise from the contact formation step and/or the $CdCl_2$ treatment. This is in agreement with the survey spectrum of the "back" surface, which shows the strongest O signal. Also, the formation of $CdTeO_3$ appears possible, as reported by McCandless and co-workers [105]. Furthermore, we find that the Te atoms on the LO-SS surface are predominantly in a CdTe environment, and that a large fraction of the Te atoms on the LO-g surface is in an oxide environment. We speculate that this tellurium oxide is either formed from oxygen atoms of the SnO_2 front contact or due to the "back" oxidation of tellurium on grains that remained after the cleavage step.
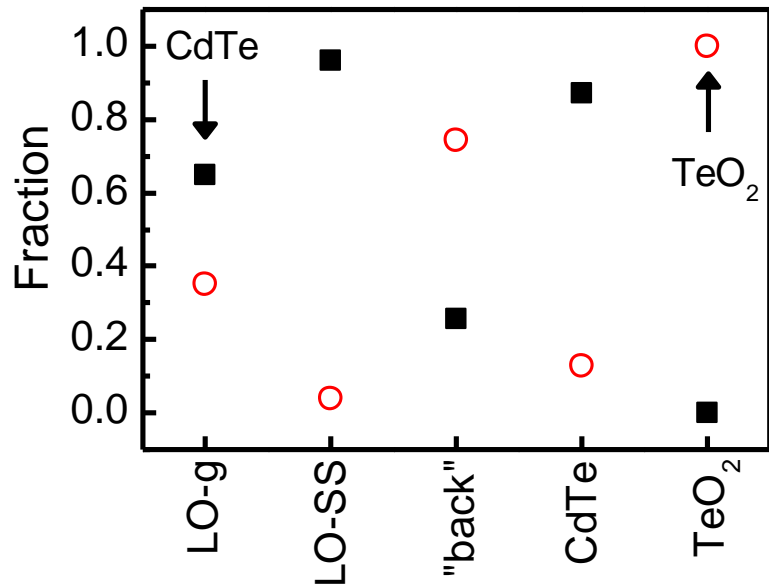
Fig. 7.9: Fraction of CdTe (solid black squares) and TeO_2 (open red circles) fit components, derived from the fits shown in Fig. 7.8.

7.4 Summary

Thus, in combining soft x-ray spectroscopies (XPS and XES) with different information depths, we find significant impacts of the various treatments on the chemical structure of CdTe-based thin film samples. The $CdCl_2$ treatment induces sulfur atoms to migrate from the CdS layer towards the BC, but no sulfur atoms reach the back surface. Most likely, a Cd(S,Te) layer is formed, as previously reported in Ref. 100. Furthermore, the $CdCl_2$ treatment affects the morphology (as seen in AFM) and chemical structure of the subsequently deposited Au/Cu layer. Most notably, it appears to suppress the Cu concentration at the back surface. We find that the BC treatment alone leaves the back surface dominated by Au and Cu, with Cu being driven towards the back surface and/or Au towards the CdTe absorber. Finally, we observe that the $CdCl_2$ treatment is "dominant" over the BC treatment. That is, both the morphology and chemical structure results of the "both-treatments" sample (*i.e.*, the one most relevant for a real device) were similar to that of the (only) $CdCl_2$-activated sample. The findings thus shed light on the chemical and morphological impact of post-deposition steps on CdTe/CdS-based thin film solar cells. Future work will focus on optimizing the associated process parameters, as well as on painting the associated electronic structure picture.

We have investigated an initially buried interface of a CdTe-based solar cell using a suitable lift-off technique and surface-sensitive X-ray photoelectron spectroscopy. We find that the region of cleavage is at or near the CdTe-CdS interface. The surfaces exposed on either side of the cleavage interface exhibit substantially less oxygen than the "back" surface. We also find that the Te atoms that remain on the cleavage-exposed surface on the back contact side are in a predominantly (95%) CdTe-like chemical

environment, while the Te atoms on the cleavage-exposed surface on the front contact side are present as CdTe (65%) and TeO_2 (35%).

CHAPTER 8

SUMMARY

In this dissertation, the investigation of surfaces and interfaces in relevant optoelectronic devices such as LEDs and solar cells was presented. Many complementary analytical techniques, both spectroscopic and microscopic, have demonstrated as being effective and insightful tools for device optimizations. The motivation behind this work was to investigate the chemical and electronic structure of materials which have important applications in energy-related devices. Experiments and samples were carefully designed so that a methodical approach to could elucidate the potential reasoning for empirically-derived optimized electrical properties of the. The goal of this dissertation is to provide new insight and physical explanations for these properties which will aid in future optimization.

In Chapters 4 and 5, the contact formation of V-based contacts onto n-type GaN and AlN were presented. There is a clear indication for the formation of VN at the contact-nitride interface that is a result of the RTA treatment required for electrical Ohmic properties. In the case for n-GaN, metallic Ga was present on the surface which indicated the chemical pathway of contact formation. This indicated that the V-Ga exchange occurred at the V/GaN interface, and the nitrogen source for VN formation was from the n-GaN substrate. In addition, the morphology of the contact transformed to consist of dendritic features (mostly composed of Au and Al) as a result of the contact formation. The elemental distribution of V and Au are found to be anti-correlated.

In contrast to the n-GaN system, the surface morphology of the n-AlN system after contact formation consisted of large and small clusters. The large clusters are composed of Au and V atoms (presumably in metallic and VN environments), while the

95

small clusters are composed of aluminum oxide. Together with n-GaN and n-AlN results, the nitrogen source for VN formation is proposed to be the GaN or AlN substrate, and not the ambient nitrogen molecules during annealing. Finally, we have discussed the thermodynamical considerations governing the formation of GaN, VN, and AlN, and thus shed light on the metal contact interaction mechanism for the entire n-(Al,Ga)N alloy. These findings provide detailed insight into the contact formation of AlGaN-based devices and the improved performance of V-based contacts, and can aid in the future design of contact materials to novel semiconductors in the future.

The interface formation between thin film CIGSe absorbers and CdS for solar cells was presented in Chapter 6. The findings provided evidence for the presence of a S-containing interlayer between CdS and the CIGSe absorber, and an additional Cd-containing species and speculate that it could involve Se atoms liberated as a result of the formation of the S-containing interlayer. These results provide additional details to the interface formation between CdS and other Cu-chalcopyrite absorbers. The electronic energy alignment at the CdS/CIGSe interface was also presented, and it displayed an unfavorable "cliff-like" band alignment. The interface structure is highly complex, with large impact on the electronic properties of the buffer/absorber interface. A comprehensive overview of the interface formation between CdS and CIGSe was shown, and this will provide insight for future optimization in the CIGSe system such as extension of the In-termination in the growth process.

The impacts of individual post-absorber deposition treatments for thin film CdTe/CdS solar cells were presented in Chapter 7. The $CdCl_2$ treatment drives the sulfur atoms to the CdTe layer (but not to the back surface), and most likely forms Cd(S,Te).

Furthermore, the CdCl$_2$ treatment affects the CdTe grains which in turn, affects the morphology and chemical environment of the subsequently deposited Au/Cu back contacts and suppresses the Cu concentration at the back surface. We find that the back contact treatment alone leaves the back surface dominated by Au and Cu, with Cu being driven towards the back surface and/or Au towards the CdTe absorber. Also, the CdCl$_2$ treatment is observed to be "dominant" over the back contact treatment, where both the morphology and chemical structure results of the sample undergone both treatments (*i.e.*, the one most relevant for a real device) were similar to that of the (only) CdCl$_2$-activated sample. A CdTe solar cell, that had undergone the post-absorber treatments, was cleaved at the CdTe/CdS interface. The Te atoms existed on both newly exposed surfaces, but the cleavage-exposed surface on the back contact side are in a predominantly CdTe-like chemical environment, while the Te atoms on the cleavage-exposed surface on the front contact side are present as CdTe and TeO$_2$. The findings thus shed light on the chemical and morphological impact of post-deposition steps on CdTe/CdS-based thin film solar cells, and the chemical structure at the once-buried CdTe/CdS interface. Future work will focus on optimizing the associated process parameters in light of their chemical and structural influences. Future efforts should also include investigating the *real* (i.e., after post-deposition treatments) electronic structure at the CdTe/CdS as it was previously inaccessible before lift-off.

APPENDIX

LIST OF SYMBOLS AND ABBREVIATIONS

AFM	Atomic force microscopy
BC	Back contact
CBD	Chemical bath deposition
CBM	Conduction band minimum
CBO	Conduction band offset
CdS	Cadmium sulfide
CdTe	Cadmium telluride
CIGSe	Copper indium gallium diselenide, $Cu(In,Ga)Se_2$
DOS	Density of states
DS	Doniach-Šunjić
E_B	Binding energy
E_F	Fermi energy or level
E_g	Energy gap for semiconductors and insulators, band gap
E_{kin}	Kinetic energy
E_{vac}	Vacuum level
FWHM	Full-width at half maximum
$h\nu$	Photon energy
IIBB	Interface Induced Band Bending
IPES	Inverse photoelectron spectroscopy
LED	Light emitting diode
LO-g	Lift-off glass substrate side
LO-SS	Lift-off stainless steel substrate side

n-AlN	negatively doped AlN
n-GaN	negatively doped GaN
Φ	Work function
PEEM	Photoemission electron microscopy
PES	Photoemission spectroscopy
PV	Photovoltaic
RTA	Rapid thermal annealing
SEM	Scanning electron microscopy
UHV	Ultra-high vacuum
UPS	Ultraviolet photoelectron spectroscopy
VBM	Valence band maximum
VBO	Valence band offset
WDS	Wavelength dispersive spectroscopy
χ	Electron affinity
XAES	X-ray Excited Auger electron spectroscopy
XES	X-ray emission spectroscopy
XPS	X-ray Photoelectron spectroscopy

BIBLIOGRAPHY

[1] J. E. Lilienfeld, U. S. Patent No.1,745,175 (8 October 1926).

[2] S. Nakamura, T. Mukai, and M. Senoh, *Appl. Phys. Lett.* **64**, 1687 (1994).

[3] F. A. Ponce and D. P. Bour, *Nature* **386**, 351 (1997).

[4] L. T. Sharp, A. Stockman, W. Jagla, and H. Jägle, *J. of Vision* **5**, 948 (2005).

[5] I. Repins, M. A. Contreras, B. Egaas, C. DeHart, J. Scharf, C. L. Perkins, B. To, and R. Noufi, *Prog. Photovolt: Res. Appl.* **16**, 235 (2008).

[6] X. Wu, J. C. Keane, R. G. Dhere, C. DeHart, D. S. Albin, A. Duda, T. A. Gessert, S. Asher, D. H. Levi, and P. Sheldon, *17th EPVSC* (Munich), 995 (2001).

[7] W. Shockley and H. J. Queisser, *J. Appl. Phys.* **32**, 510 (1961).

[8] S. M. Sze, Semiconductor Devices: Physics and Technology, 2nd ed. (John Wiley and Sons, New York, 2002).

[9] K. O. Schweitz, P. K. Wang, S. E. Mohney, and D. Gotthold, *Appl. Phys. Lett*. **80**, 1954 (2002).

[10] R. France, T. Xu, P. Chen, R. Chandrasekaran, and T. D. Moustakas, *Appl. Phys. Lett.* **90**, 062115 (2007).

[11] I. Galesic and B. O. Kolbesen, *Thin Solid Films* **349**, 14 (1999).

[12] R. Noufi, 4th IEEE WCPEC (Hawaii), oral presentation.

[13] L. Kronik, L. Burstein, M. Leibovitch, Y. Shapira, D. Gal, E. Moons, J. Beier, G. Hodes, D. Cahen, D. Hariskos, R. Klenk, and H.-W. Schock, *Appl. Phys. Lett.* **67**, 1405 (1995).

[14] M. Morkel, L. Weinhardt, B. Lohmüller, C. Heske, E. Umbach, W. Riedl, S. Zweigart, and F. Karg, *Appl. Phys. Lett.* **79**, 4482 (2001).

[15] L. Weinhardt, M. Morkel, Th. Gleim, S. Zweigart, T. P. Niesen, F. Karg, C. Heske, and E. Umbach, *17th EPVSC* (Munich), 1261 (2001).

[16] L. Weinhardt, O. Fuchs, D. Groβ, G. Storch, E. Umbach, N. G. Dhere, A. A. Kadam, S. S. Kulkarni, and C. Heske, *Appl. Phys. Lett*. **86**, 062109 (2005).

[17] P. V. Meyers, C.-H. Liu, and T. J. Frey, U. S. Patent No. 4,873,198 (10 October 1989).

[18] S. A. Ringel, A. W. Smith, M. H. MacDougal, and A. Rohatgi, *J. Appl. Phys.* **70**, 881 (1991).

[19] K. Kuribayashi, H. Matsumoto, H. Uda, Y. Komatsu, A. Nakano, and S. Ikegami, *Jpn. J. Appl. Phys.* **22**, 1828 (1983).

[20] H. C. Chou, A. Rohatgi, N. M. Jokerst, E. W. Thomas, and S. Kamra, *J. Electronic Materials* **25**, 1093 (1996).

[21] H. Uda, S. Ikegami, and H. Sonomura, *Sol. Energy Mater. Sol. Cells* **50**, 141 (1998).

[22] D. Grecu and A. D. Compaan, *Appl. Phys. Lett.* **75**, 361 (1999).

[23] A. Zangwill, Physics at Surfaces, 1st ed. (New York, Cambridge University Press, 1988).

[24] M. P. Seah and W. A. Dench, *Surf. Interface Anal.* **1**, 2 (1979).

[25] M. T. Anthony and M. P. Seah, *Surf. Interface Anal.* **6**, 107 (1984).

[26] F. Schedin, G. Thornton, and R. I. G. Uhrberg, *Rev. Sci. Instrum.* **68**, 41 (1997).

[27] V. Dibeler, J. A. Walker, K. E. McCulloh, and H. Rosenstock, *Int. J. Mass Spectrom. Ion Phys.* **7**, 209 (1971).

[28] N. V. Smith and D. P. Woodruff, *Prog. Surf. Sci.* **21**, 295 (1986).

[29] T. Gleim, C. Heske, E. Umbach, C. Schumacher, S. Gundel, W. Faschinger, A. Fleszar, C. Ammon, M. Probst, and H. –P. Steinrueck, *Surf. Sci.* **531**, 77 (2003).

[30] D. Briggs and M. P. Seah, Practical Surface Analysis: Auger and Photoelectron Spectroscopy, 2nd ed. (John Wiley and Sons, Chichester, 1990).

[31] C. A. Wagner, A. V. Naumkin, A. Kraut-Vass, J. W. Allison, C. J. Powell, and J. R. Rumble, Jr., NIST X-ray Photoelectron Spectroscopy Database. http://srdata.nist.gov/xps.

[32] S. Doniach and M. Šunjić, *J. Phys. C: Solid State Phys.* **3**, 285 (1970).

[33] David Attwood, Soft X-Rays and Extreme Ultraviolet Radiation: Principles and Applications, 1st ed. (Berkeley, Cambridge University Press, 2007).

[34] B. L. Henke, E. M. Gullikson, and J. C. Davis, *Atomic Data Tables* **54**, 181 (1993).

[35] Beamline 8.0.1 Technical Specifications, http://www.als.lbl.gov/als/techspecs/bl8.0.1.html

[36] J. J. Jia, T. A. Callcott, J. Yurkas, A. W. Ellis, F. J. Himpsel, M. G. Samant, J. Stöhr, D. L. Ederer, J. A. Carlisle, E. A. Hudson, L. J. Terminello, D. K. Shuh, and R. C. C. Perera, *Rev. Sci. Instrum.* **66**, 1394 (1995).

[37] M. Blum, L. Weinhardt, O. Fuchs, M. Bär, Y. Zhang, M. Weigand, S. Krause, S. Pookpanratana, T. Hofmann, W. Yang, J. D. Denlinger, E. Umbach, and C. Heske, *Rev. Sci. Instrum.* **80**, 123102 (2009).

[38] O. Fuchs, L. Weinhardt, M. Blum, M. Weigand, E. Umbach, M. Bär, C. Heske, J. Denlinger, Y.-D. Chuang, W. McKinney, Z. Hussain, E. Gullikson, M. Jones, P. Batson, B. Nelles, and R. Follath, *Rev. Sci. Instrum.* **80**, 063103 (2009).

[39] Park Systems Corp., About Park Systems Atomic Force Microscope, http://www.parkafm.com.

[40] K. Prabhakaran, T. G. Andersson, and K. Nozawa, *Appl. Phys. Lett.* **69**, 3212 (1996).

[41] R. Ortega-Borges and D. Lincot, *J. Electrochem. Soc.* **140**, 3464 (1993).

[42] M.E. Lin, Z. Ma, F.Y. Huang, Z.F. Fan, L.H. Allen, and H. Morkoc, *Appl. Phys. Lett.* **64**, 1003 (1994).

[43] K.O. Schweitz and S.E. Mohney, *J. Electron. Mater.* **30**, 175 (2001).

[44] V.S. Fomenko, Handbook of Thermionic Properties: Electronic Work Functions and Richardson Constants of Elements and Compounds, (Plenum, New York, 1966), p. 103.

[45] J. S. Foresi and T. D. Moustakas, *Appl. Phys. Lett.* **62**, 2859 (1993).

[46] D. R. Lide, CRC Handbook of Chemistry and Physics, 88th ed. (Boca Raton, CRC Press/Taylor and Francis, 2008), 12-79.

[47] M.W. Fay, G. Moldovan, P.D.Brown, I. Harrison, J.C. Birbeck, B.T. Hughes, M.J. Uren, and T. Martin, *J. Appl. Phys.* **92**, 94 (2002).

[48] J.O. Song, S.-H. Kim, J.S. Kwak, and T.-Y. Seong, *Appl. Phys. Lett*. **83**, 1154 (2003).

[49] D. Selvanathan, F.M. Mohammed, A. Tesfayesus, and I. Adesida, *J. Vac. Sci. Technol. B* **22**, 2409 (2004).

[50] C.I. Wu and A. Kahn, *J. Vac. Sci. Technol. B* **16**, 2218 (1998).

[51] G. Schön, *J. Electron. Spectrosc. Rel. Phenom*. **2**, 75 (1973)

[52] S. Evans, *Surf. Interface Anal.* **7**, 299 (1985);

[53] R. Carin, J.P. Deville, and J. Werckmann, *Surf. Interface Anal.* **16**, 65 (1990);

[54] S.D. Wolter, B.P. Luther, D.L. Waltemyer, C. Önneby, S.E. Mohney, and R.J. Molnar, *Appl. Phys. Lett.* **70**, 2156 (1997).

[55] C.B. Stagarescu, L.-C. Duda, K.E. Smith, J.H. Guo, J. Nordgren, R. Singh, and T.D. Moustakas, *Phys. Rev. B* **54**, 335 (1996).

[56] E. A. Brandes, <u>Smithells Metals Reference Book</u>, 6th ed., (London, Butterworths, 1985) 10-1.

[57] S. Tougaard, Quases Inelastic Mean Free Path calculation software, <u>http://www.quases.com/</u>

[58] J. J. Yeh and I. Lindau, *Atomic Data and Nuclear Data Tables* **32**, 1-155 (1985).

[59] S. Nakamura, M. Senoh, S. Nagahama, N. Iwasa, T. Yamada, T. Matsushita, H. Kiyoku, Y. Sugimoto, T. Kozaki, H. Umemoto, M. Sano, and K. Chocho, *Appl. Phys. Lett.* **72**, 2014 (1998).

[60] E. Monroy, M. Hamilton, D. Walker, P. Kung, F. J. Sanchez, and M. Razeghi, *Appl. Phys. Lett*. **74**, 1171 (1999).

[61] C. I. Wu and A. Kahn, *Appl. Surf. Sci.* **162-163**, 250 (2000).

[62] J. I. Pankove and H. Schade, *Appl. Phys. Lett*. **25**, 53 (1974).

[63] M. C. Benjamin, C. Wang, R. F. Davis, and R. J. Nemanich, *Appl. Phys. Lett.* **64**, 3288 (1994).

[64] D. R. Lide, "Properties of Semiconductors", in <u>CRC Handbook of Chemistry and Physics</u>, 90th ed. (Boca Raton, CRC Press/Taylor and Francis, 2010).

[65] L. C. Duda, C. B. Stagarescu, J. Downes, K. E. Smith, D. Korakakis, T. D. Moustakas, J. Guo, and J. Nordgren, *Phys. Rev. B* **58**, 1928 (1998).

[66] M. Magnuson, M. Mattesini, C. Höglund, J. Birch, and L. Hultman, *Phys. Rev. B* **80**, 155105 (2009).

[67] D. W. Fischer, *J. Appl. Phys*. **40**, 4151 (1969).

[68] A. Callenås, L. I. Johansson, A. N. Christensen, K. Schwarz, and P. Blaha, *Phys. Rev. B* **32**, 575 (1985).
[69] R. Fix, R. G. Gordon, and D. M. Hoffman*, Chem. Mater.* **5**, 614 (1993).

[70] R. Sanjinés, P. Hones, and F. Lévy, *Thin Solid Films* **332**, 225 (1998).

[71] A. Barrie, *Chem. Phys. Lett*. **19**, 109 (1973)

[72] R. Z. Bachrach, S. A. Flodström, R. S. Bauer, S. B. M. Haström, and D. J. Chadi, *J. Vac, Sci. Technol.* **15**, 488 (1978).

[73] A. Thompson, D. Vaughan, D. Attwood, E. Gullikson, M. Howells, K.-J. Kim, J. Kirz, J. Kortright, I. Lindau, Y. Liu, P. Pianetta, A. Robinson, J. Scofield, J. Underwood, G. Williams, and H. Winick, X-ray Data Booklet, (Lawrence Berkeley National Lab, Berkeley, 2009) p. 1-2. http://xdb.lbl.gov/

[74] D. N. Talwar, D. Sofranko, C. Mooney, and S. Tallo, *Materials Science and Engineering* **B90**, 269 (2002).

[75] M.A. Green, K. Emery, Y. Hishikawa, W. Warta, *Prog. Photovolt: Res. Appl.* **16**, 61 (2008).

[76] C. Heske, D. Eich, R. Fink, E. Umbach, T. Van Buuren, C. Bostedt, L. J. Terminello, S. Kakar, M. M. Grush, T. A. Callcott, F. J. Himpsel, D. L. Ederer, R. C. C. Perera, W. Riedl, and F. Karg, *Appl. Phys. Lett*. **74**, 1451 (1999).

[77] L. Weinhardt, M. Bär, S. Pookpanratana, M. Morkel, T. P. Niesen, F. Karg, K. Ramanathan, M. A. Contreras, R. Noufi, E. Umbach, and C. Heske, *Appl. Phys. Lett*. **96**, 182102 (2010).

[78] N. Terada, R. T. Widodo, K. Itoh, S. H. Kong, H. Kashiwabara, T. Okuda, K. Obara, S. Niki, K. Sakurai, A. Yamada, and S. Ishizuka, *Thin Solid Films* **480-481**, 183 (2005).

[79] X. Liu and J. R. Sites, AIP Conference Proceedings (Anaheim), 444 (1996).

[80] I. Hengel, A. Neisser, R. Klenkm and M. Ch. Lux-Steiner, *Thin Solid Films* **361-362**, 458 (2000).

[81] R. Klenk, *Thin Solid Films* **387**, 135 (2001).

[82] L. Weinhardt, O. Fuchs, E. Umbach, C. Heske, A. Fleszar, W. Hanke, and J. D. Denlinger, *Phys. Rev. B* **75**, 165207 (2007).

[83] L. Zhou, T. A. Callcott, J. J. Jia, D. L. Ederer, and R. Perera, *Phys. Rev. B* **55**, 5051 (1997).

[84] L. Weinhardt, O. Fuchs, A. Fleszar, M. Bär, M. Blum, M. Weigand, J. D. Denlinger, W. Yang, W. Hanke, E. Umbach, and C. Heske, *Phys. Rev. B* **79**, 165305 (2009).

[85] C. Heske, D. Eich, R. Fink, E. Umbach, S. Kakar, T. Van Buuren, C. Bostedt, L. J. Terminello, M. M. Grush, T. A. Callcott, F. J. Himpsel, D. L. Ederer, R. C. C. Perera, W. Riedl, and F. Karg, *Appl. Phys. Lett.* **75**, 2082 (1999).

[86] M. Polak, *J. Electron Spectrosc. Rel.Phenom.* **28**, 171 (1982).

[87] S. W. Garrenstroom and N. Winograd, *J. Chem. Phys.* **67**, 3500 (1977).

[88] A. Roche, H. Montes, J. Brissot, M. Romand, P. Josseaux, and A. K. De Mesmaeker, *Appl. Surf. Sci.* **21**, 12 (1985).

[89] H. Seyama and M. Soma, *J. Chem. Soc. Faraday Trans. I* **80**, 237 (1984).

[90] M. Bär, I. Repins, M. A. Contreras, L. Weinhardt, R. Noufi, and C. Heske, *Appl. Phys. Lett.* **95**, 052106 (2009).

[91] O. de Melo, L. Hernandez, O. Zelaya-Angel, R. Lozada-Morales, M. Becerril, and E. Vasco, *Appl. Phys. Lett.* **65**, 1278 (1994).

[92] First Solar Quarterly Reports, http://investor.firstsolar.com/

[93] N. Nakayama, H. Matsumoto, A. Nakano, S. Ikegami, H. Uda, and T. Yamashita, *Jpn. J. Appl. Phys.* **19**, 703 (1980).

[94] W. K. Metzger, D. Albin, M. J. Romero, P. Dippo, and M. Young, *J. Appl. Phys.* **99**, 103703 (2006).

[95] J. Zhou, X. Wu, Y. Yan, S. Asher, J. Da Silva, S. Wei, L. Weinhardt, M. Bär, and C. Heske, *Mater. Rec. Soc. Symp. Proc.* **1012**, 1012-Y13-03 (2007).

[96] R. Dhere, D. Rose, D. Albin, S. Asher, M. Al-Jassim, H. Cheong, A. Swartzlander, H. Moutinho, T. Coutts, and P. Sheldon, *Proc. 26th IEEE PVSC*, 435 (1997).

[97] I. Visoly-Fisher, K. D. Dobson, J. Nair, E. Bezalel, G. Hodes, and D. Cahen, *Adv. Func. Mater.* **13**, 289 (2003).

[98] J. Fritsche, A. Klein, and W. Jaegermann, *Adv. Eng. Mater.* **7**, 914 (2005).

[99] X. Liu, N. R. Paudel, A. D. Compaan, K. Sun, L. Weinhardt, M. Bär, S. Pookpanratana, C. Heske, O. Fuchs, W. Yang, and J. D. Denlinger, *Proc. 34th IEEE PVSC*, 2107 (2009).

[100] I. Clemminck, M. Burgelman, M. Casteleyn, J. De Poorter, and A. Vervaet, *Proc. 22nd IEEE PVSC*, 1114 (1991).

[101] M. Emziane, K. Durose, N. Romeo, A. Bosio, and D. P. Halliday, *Thin Solid Films* **480-481**, 377 (2005).

[102] C. Heske, U. Groh, O. Fuchs, E. Umbach, N. Franco, C. Bostedt, L. J. Terminello, R. C. C. Perera, K. H. Hallemeier, A. Preobrajenski, R. Szargan, S. Zweigart, W. Riedl, and F. Karg, *Phys. Stat. Sol. (a)* **187**, 13 (2001).

[103] L. Weinhardt, O. Fuchs, D. Groβ, E. Umbach, C. Heske, N. G. Dhere, A. A. Kadam, and S. S. Kulkarni, *J. Appl. Phys.* **100**, 024907 (2006)

[104] K. D. Dobson, I. Visoly-Fisher, G. Hodes, and D. Cahen, *Sol. Energy Mater. Sol. Cells* **62**, 295 (2000).

[105] B. E. McCandless, S. S. Hegedus, R. W. Birkmire, and D. Cunningham, *Thin Solid Films* **431-432**, 249 (2003).

VITA

Graduate College
University of Nevada, Las Vegas

Sujitra Pookpanratana

Degree:
Bachelor of Science, Chemical Engineering, 2006
University of California, San Diego

Special Honors and Awards:
1. Nowak-Notre Dame Graduate Student Award from UNLV Chemistry Dept., 2008-2009
2. Graduate Student Travel Award from Materials Research Society (MRS), Compound Semiconductors for Energy Applications and Environmental Sustainability Symposium, Spring 2009
3. University of California, San Diego (UCSD) Provost's Honors in Fall 2003, Winter & Spring 2004, Winter, Spring, & Fall 2005
4. UCSD Science and Engineering scholarship, 2004-2005

Publications:
1. **S. Pookpanratana**, F. Khan, Y. Zhang, C. Heske, L. Weinhardt, M. Bär, X. Liu, N. Paudel, and A. Compaan, "Chemical structure of buried interfaces in CdTe thin film solar cells," *35th Institute of Electrical and Electronics Engineers (IEEE) Photovoltaic Specialists Conference Proceeding*, in print.
2. **S. Pookpanratana**, I. Repins, M. Bär, L. Weinhardt, Y. Zhang, R. Félix, M. Blum, W. Yang, and C. Heske, "CdS/Cu(In,Ga)Se$_2$ interface formation in high-efficiency thin film solar cells," *Appl. Phys. Lett*. **97**, 074101 (2010).
3. M. Bär, M. Wimmer, R. G. Wilks, M. Roczen, D. Gerlach, F. Ruske, K. Lips, B. Rech, L. Weinhardt, M. Blum, **S. Pookpanratana**, S. Krause, Y. Zhang, C. Heske, W. Yang, and J. D. Denlinger, "Impact of solid-phase crystallization of amorphous silicon on the chemical structure of the buried Si/ZnO thin film solar cell interface," *Appl. Phys. Lett.* **97**, 072105 (2010).
4. **S. Pookpanratana**, R. France, M. Blum, A. Bell, M. Bär, L. Weinhardt, Y. Zhang, T. Hofmann, O. Fuchs, W. Yang, J.D. Denlinger, S. Mulcahy, T.D. Moustakas, and C. Heske, "Chemical structure of vanadium-based contact formation on n-AlN," *J. Appl. Phys.* **108**, 024906 (2010).
5. L. Weinhardt, M. Bär, **S. Pookpanratana**, M. Morkel, T. P. Niesen, F. Karg, K. Ramanathan, M. A. Contreras, R. Noufi, E. Umbach, and C. Heske, "Sulfur gradient-driven Se diffusion at the CdS/CuIn(S,Se)$_2$ solar cell interface," *Appl. Phys. Lett.* **96**, 182102 (2010).
6. M. Bär, N. Barreau, F. Couzinié-Devy, **S. Pookpanratana**, J. Klaer, M. Blum, Y. Zhang, W. Yang, J. D. Denlinger, H. –W. Schock, L. Weinhardt, J. Kessler, and C. Heske, "Chemical structure of the heavily intermixed In$_2$S$_3$/Cu(In,Ga)Se$_2$ interface," *Appl. Phys. Lett.* **96**, 184101 (2010).

7. **S. Pookpanratana**, I. Repins, M. Bär, R. Felix, M. Blum, L. Weinhardt, W. Yang, J. D. Denlinger, M. A. Contreras, and C. Heske, "Spectroscopic Analysis of the Chemical Structure at the CdS/Cu(In,Ga)Se$_2$ Interface in High-Efficiency Solar Cell Devices," *34th IEEE Photovoltaic Specialists Conference Proceeding*, 1060 (2009).

8. X. Liu, N. R. Paudel, A. D. Compaan, K. Sun, L. Weinhardt, M. Bär, **S. Pookpanratana**, C. Heske, W. Yang, and J. D. Denlinger, "Migration and Oxidation of Sulfur at the Back Contact in CdTe Cells," *34th IEEE Photovoltaic Specialists Conference Proceeding*, 2107 (2009).

9. M. Blum, L. Weinhardt, O. Fuchs, M. Bär, Y. Zhang, M. Weigand, S. Krause, **S. Pookpanratana**, T. Hofmann, W. Yang, J. D. Denlinger, E. Umbach, and C. Heske, "Solid and liquid spectroscopic analysis – a soft x-ray spectroscopy endstation with a novel flow-through liquid cell," *Rev. Sci. Instrum.* **80**, 123102 (2009).

10. M. Bär**,** K.-S. Ahn, S. Shet, Y. Yan, L. Weinhardt, O. Fuchs, M. Blum, **S. Pookpanratana**, K. George, W. Yang, J. D. Denlinger, M. Al-Jassim, and C. Heske, "Impact of air exposure on the chemical and electronic structure of ZnO: Zn$_3$N$_2$ thin films," *Appl. Phys. Lett.*, **94**, 012110 (2009).

11. M. Bär, L. Weinhardt, **S. Pookpanratana**, C. Heske, S. Nishiwaki, W. N. Shafarman, O. Fuchs, M. Blum, W. Yang, and J. D. Denlinger, "Band Gap Energy of Chalcopyrite Thin Film Solar Cell Absorbers Determined by Soft X-ray Emission and Absorption Spectroscopy," *33rd IEEE Photovoltaic Specialists Conference Proceeding,* DOI: 10.1109/PVSC.2008.4922728 (2008).

12. M. Bär**,** S. Nishiwaki, L. Weinhardt, **S. Pookpanratana**, O. Fuchs, M. Blum, W. Yang, J.D. Denlinger, W. N. Shafarman, and C. Heske, "Depth-resolved band gap in Cu(In,Ga)(S,Se)$_2$ thin films," *Appl. Phys. Lett.*, **93**, 244103 (2008).

13. **S. Pookpanratana**, R. France, M. Bär, L. Weinhardt, O. Fuchs, M. Blum, W. Yang, J.D. Denlinger, T.D. Moustakas, and C. Heske, "Intermixing and chemical structure at the interface between n-GaN and V-based contacts," *Appl. Phys. Lett.*, **93**, 172106 (2008).

14. M. Bär, S. Nishiwaki, L. Weinhardt, **S. Pookpanratana**, W. N. Shafarman, and C. Heske, "Electronic level alignment at the deeply buried absorber/Mo interface in chalcopyrite-based thin film solar cells," *Appl. Phys. Lett.*, **93**, 042110 (2008).

Dissertation Title: Chemical and Electronic Structure of Surfaces and Interfaces in Compound Semiconductors

Dissertation Examination Committee:
      Chairperson, Clemens Heske, Dr. rer. nat.
      Committee Member, Paul Forster, Ph. D.
      Committee Member, Dennis Lindle, Ph. D.
      Graduate Faculty Representative, Rama Venkat, Ph. D.